Spin Transport in Lateral Spin Valves

Joseph Thomas Batley

University of Leeds

School of Physics and Astronomy

Submitted in accordance with the
requirements for the degree of

Doctor of Philosophy

August 2015

Intellectual Property Statement

The candidate confirms that the work submitted is his/her own, except where work which has formed part of jointly authored publications has been included. The contribution of the candidate and the other authors to this work has been explicitly indicated below. The candidate confirms that appropriate credit has been given within the thesis where reference has been made to the work of others.

This copy has been supplied on the understanding that it is copyright material and that no quotation from the thesis may be published without proper acknowledgement.

The right of Joseph Thomas Batley to be identified as Author of this work has been asserted by him in accordance with the Copyright, Designs and Patents Act 1988.

Work from the following jointly authored papers is in this thesis:

M. C. Rosamond, **J. T. Batley**, G. Burnell, B. J. Hickey, and E. H. Linfield, ‘High contrast 3D proximity correction for electron-beam lithography: An enabling technique for the fabrication of suspended masks for complete device fabrication within an UHV environment’, Microelectron. Eng., 143, 5 (2015).

Paper details some of the methods used during device fabrication. This is included in the experimental methods chapter 3.

- **Work attributed to the candidate**: Sample prep, development and deposition. Discussion of fabrication process.
- **Work attributed to others**: M. C. Rosamond: Sample prep and development. Data analysis and simulations. Patterning of samples. Discussion of fabrication process. E. H. Linfield: Support and management for M. C. Rosamond. G. Burnell: Support and management for J. T. Batley, Discussion of fabrication process. B. J. Hickey: Support and management for J. T. Batley

J. T. Batley, M. C. Rosamond, M. Ali, E. H. Linfield, G. Burnell, B. J. Hickey,‘Spin relaxation through Kondo scattering in Cu/Py lateral spin valves’, Phys. Rev. B 92, 220420(R) (2015).

This work forms the majority of chapter 4.

- **Work attributed to the candidate**: Design and management of the project, fabrication of devices, measurements, construction of deposition system, interpretation and analysis, and writing of the manuscript.
- **Work attributed to others**: M. C. Rosamond: fabrication of devices. M. Ali: construction of deposition system. E. H. Linfield: provided support and management for M. C. Rosamond. G. Burnell: design and management of the project, measurements, construction of deposition system, interpretation and analysis, and reviewed and edited manuscript. B. J. Hickey: design and management of the project, construction of deposition system, interpretation and analysis, and reviewed and edited manuscript.

Acknowledgements

Firstly, I would like to thank both my supervisors, Prof. Bryan Hickey and Dr. Gavin Burnell, for all the support and motivation they have given during this work. Their enthusiasm can be contagious and has often provided a much needed boost in the turmoil that is a PhD. I am especially thankful for Gavin's willingness to debug software and penchant for practical jokes, along with Bryan's good humour and ability to put up with me.

I am extremely grateful of all the help and support from Dr. Mannan Ali. His training in all things vacuum related and considerable input into the design and construction of the angled deposition system were key factors in enabling me to grow any samples at all. I would also like to thank Dr. James Witt, whose fellow love of coffee provided a catalyst for useful discussion and who also helped in continually fixing the deposition system. Dr. Mark Rosamond performed the electron beam lithography for all of the samples in this work, he was a great help in all the clean room processing. His ability to drag a silver lining out of almost all lithographic failures is impressive and greatly appreciated.

A lot of this work involved the building of new equipment and without the expertise and skill of the technical staff in the physics department this project would have gone a very different route. John Turton's ability to fix almost anything has been a huge help during my PhD. Brian Gibbs, Leigh Harris, Trevor Haynes, Richard Oliver and Andrew Price have all provided assistance with the construction of equipment. I would also like to thank Phil Cale and Luke Bone for their ability to keep up with my tireless helium consumption.

I am especially grateful to all members of the Condensed Matter Group, past and present, who have helped and trained me during my PhD, especially Dr. Mark Elkin, Dr. Christopher Allen and Dr. Nicholas Porter. I would also like to thank both Philippa Shepley and Sophie Morley for sharing in the madness, listening to my rants, and providing new ideas for my procrastination.

To my parents I am eternally thankful for their love and encouragement in all I attempt, as their support seems to know no bounds.

Finally, my wife Carley. Her support and patience has made this possible and I cannot thank her enough.

Abstract

This thesis outlines the construction of an ultra-high-vacuum angle-deposition system, developed specifically for the fabrication of lateral spin valves (LSVs). The thesis then proceeds to answer two important questions: what causes the loss of spin accumulation at low temperatures seen in LSVs? and how do spin currents interact in multi-terminal circuits?

Through a double-dose electron beam lithography and angle-deposition technique, Cu/Py LSVs are fabricated and shown to have transparent contacts. By means of a DC injection method, the nonlocal voltage is measured as a function of injection current, magnetic field and temperature, enabling contributions from heat and spin currents to be isolated.

The spin diffusion length is obtained from LSVs fabricated with Cu containing magnetic impurities <1 ppm and ~4 ppm. Temperature dependent charge and spin transport measurements provide evidence linking the presence of the Kondo effect in Cu to the suppression of the spin diffusion length below 30 K. The spin-flip probability for magnetic impurities is found to be 34%, orders of magnitude larger than other scattering mechanisms. This is extended to explain similar observations in the spin accumulation. These measurements establish the dominant role of Kondo scattering in spin-relaxation, even in low concentrations of order 1 ppm.

Finally, a new multi-terminal LSV (MTLSV) is fabricated and the interaction between two spin currents is investigated. Fan-out and fan-in measurements are performed, demonstrating that spin currents separate and combine at junctions in a circuit with magnitudes dictated by the spin resistance of the conduction channels. It is also shown that two spin currents of opposite polarity will cancel out. Whether Kirchhoff's law holds for spin currents is discussed and this chapter helps lay the ground work for spin current based circuits and computation.

Abbreviations

LSV	Lateral Spin Valve
MTLSV	Multi-Terminal Lateral Spin Valve
FM	Ferromagnetic
NM	Nonmagnetic
P	Parallel
AP	Antiparallel
KR	Kelvin Resistor
NLIV	Nonlocal Current-Voltage curve
3DNLIV	3-Dimensional Nonlocal Current-Voltage curve
ECP	Electrochemical Potential
DOS	Density of States
SOC	Spin Orbit Coupling
VBS	Virtual Bound State
AMR	Anisotropic Magnetoresistance
MI	Magnetic Impurity
PDE	Partial Differential Equations
UHV	Ultra High Vacuum
VTI	Variable Temperature Insert
MOKE	Magneto Optical Kerr Effect
EBL	Electron Beam Lithography
OL	Optical Lithography
DUV	Deep Ultra Violet
SEM	Scanning Electron Microscope
LOR	Lift Off Resist
DI H_2O	De-Ionised Water
PMMA	Polymethyl methacrylate
MMA	Methyl methacrylate
IPA	Isopropyl alcohol
PCB	Printed Circuit Board
RF	Radio Frequency
FEM	Finite Element Method

CONTENTS

CHAPTER 1

Introduction

When Lord Kelvin made his discovery of magnetoresistance[1], it established a field that would develop theoretically and experimentally across 150 years into what is known today as spintronics. This emerging field, devoted to the exploitation of the spin degree of freedom within electron transport, saw the discovery in 1988 of giant magnetoresistance (GMR)[2, 3], nucleating an explosion in research and technological advances. The continued progress in spintronics pushes the boundaries of solid state physics through the applications of pure spin currents, a flow of spin angular momentum in the absence of a net flow of charge, presenting opportunities for information transport with reduced dissipation from Joule heating. This thesis is aimed at improving our understanding of pure spin transport in metallic heterostructures, to facilitate the development of new low power consumption and non-volatile technologies[4–6].

The magnetic spin valve is the prototypical spintronics device and its use has been forefront in the investigation in to spin transport and the development of the underlying theory[7]. However, seminal experiments prior to this by Johnson and Silsbee[8] demonstrated the strength of lateral geometries, where spin diffusion can be measured over much longer distances (~1 μm). Following this, advances in lithography saw the development of nonlocal spin injection and lateral spin valves by Jedema *et al.*[9, 10] at much smaller length scales. The reduced dimensions of these devices allow them to be considered as 1D spin conduction channels, minimising the complexity of the problem. The spatial separation of spin and charge currents in a nonlocal experiment means these nanoscale lateral spin valves (LSVs) are an ideal geometry for the study of spin transport. This has been shown in many cases with the successful measurements of spin injection and transport in various metallic[9, 11–13], semiconductors[14, 15] and superconducting[16, 17] materials. Along with this, the generation of a pure spin current in a LSVs can be achieved through charge spin injection[11, 12, 18–20], thermal current spin injection[21–23] and even spin pumping[24], proving to be useful tools for investigating efficient spin injection of many forms.

The advances in lithographic procedures have lead to the development of a versatile fabrication methods, known as shadow deposition. Through the application of bilayer resist recipes and deposition at various angles relative to the substrate, multi-material lateral device can be fabricated in one vacuum cycle. This has immediate benefits over conventional two or three step lithography as it produces high quality interfaces, since there is no exposure to atmosphere or resist between depositions. This technique is widely used for the fabrication of LSVs with both transparent interfaces[11, 13, 25] and those containing tunnel barriers[26, 27]. Knowledge of the type of interface present in a spin injection experiment is critical to the interpretation of the results, as the transparency of an interface alters the interaction of the contact with the spin current and hence the equations requited to describe the transport[28]. By developing a robust technique for shadow fabrication the quality of the interfaces is ensured removing ambiguity from the analysis.

For the past 15 years LSVs have been a dominant tool in the study of pure spin transport, and yet several key and fundamental questions have yet to be answered. It is the aim of this thesis to address two import questions: what causes the loss of spin accumulation at low temperatures? and how do pure spin currents interact?

In Chapter 5 the different mechanisms that cause spin-relaxation are discussed. Within non-magnetic metals it is reasonable to expect the Elliot-Yafet[29, 30] mechanism to play a role and thus the spin diffusion length might be inversely proportional to resistivity. However, in lateral spin valves, measurements have found that at low temperatures the spin diffusion length unexpectedly decreases[19, 25, 31, 32]. This loss of spin accumulation has become a long-standing issue, where, until now, no coherent model describing this interesting behaviour has been obtained. Having fabricated lateral spin valves from Cu with magnetic impurities <1 ppm and 4 ppm, evidence is presented that directly links the reduced spin accumulation at low temperatures to the presence of Kondo scattering[33]. The results presented in this chapter establishes the dominant role of Kondo scattering in spin-relaxation, even in low concentrations of order 1 ppm, and hence demonstrates its importance in solving this critical problem.

Although spin coherence is vital for the realisation of computation via spin currents, an equally crucial aspect is a detailed understanding of how spin currents interact in multi-terminal circuits. A fundamental theory of electronics is Kirchhoff's first law, and it is important to ask whether this can be applied in spin current circuits. Chapter 6 introduces a new multi-terminal LSV. These new devices are used to investigate the interaction between two separately generated pure spin currents, along with how a single spin current divides among branches in a circuit in order to investigate whether pure spin currents obey Kirchhoff's first law.

Before presenting these key experimental chapters, we begin, in Chapter 2 with the introduction of the necessary theory required in order to interpret the results presented later in the thesis. The Valet-Fert theory[7] is applied to the geometry of a LSV to obtain the characteristic equations for spin injection and diffusion in a metallic conductor. This chapter will also discuss the different mechanisms that contribute to spin relaxation in metals. Following this, Chapter 3 outlines the methods for device fabrication and characterisation. The techniques of shadow lithography and angled deposition used during in this work were developed specifically for the fabrication of LSVs. This chapter includes details of the custom designed ultra-high-vacuum deposition chamber that was built in house, along with the double-dose lithography recipe developed in collaboration with the engineering faculty. These allowed the first fabrication of LSVs with these techniques at the University of Leeds, and in the UK. Finally, Chapter 4 provides an overview of the devices, the design considerations and different contributions to the nonlocal measurements.

CHAPTER 2

Background Theory

2.1 Introduction

The physics of electrons in solids is complex and varied, both in the observed phenomena and the theory used to describe them. The different formalisms all contain caveats regarding their applicability, ranging from computational limits on the rigorous ab initio approaches, to the simplicity of the free electron model obscuring the finer details. When the interactions that give rise to magnetic effects are considered, things can become “enormously complicated"[34] and as such, approximations based on the dominant processes and significant length scales are required.

The main focus of this work is on spin transport in non-ferromagnetic materials, specifically paramagnetic Cu. Since Cu is a monovalent noble metal, it is well described through a free-electron dispersion relation that is generally assumed throughout this thesis. Within any physical problem the length scales involved dictate the relevant mechanisms to be considered. In this work the measured devices have dimensions, in general, much larger than the mean free path (λ_e) of the charge carriers. This allows the description of the charge flow through a Boltzmann transport equation where the approximation of a relaxation time for each scattering mechanism is used. For spin transport the critical length scale is the spin diffusion length (λ_s), which is predominately much larger than λ_e. Here it is assumed the two spin types act as parallel conduction channels as in the two channel model originally proposed by Mott[35].

This chapter presents a small overview of these basic concepts required in understanding and interpreting the results presented later in the thesis. For a more detailed discussion the reader is directed to references [36, 37].

2.2 Stoner Ferromagnetism

Ferromagnetic materials play an important role in the field of spintronics as a source of spin polarised carriers. However, the origin of their spontaneous magnetisation is in fact not a direct consequence of the spin magnetic moment of the electron but instead a combination of their charge and the Pauli principle. Within a solid material the orbital wave functions of the electrons can overlap and for fermions the total wave function must be antisymmetric. This allows two combinations of the individual wave functions, a symmetric spacial function with a singlet spin-state, or an antisymmetric spatial function and a triplet spin-state.

For simplicity, consider only two electrons with spacial coordinates $\mathbf{x}_1$ and $\mathbf{x}_2$. The joint wave function is either a symmetric or antisymmetric spatial combination of the product of individual electron states $\psi_{\mathrm{p}}(\mathbf{x}_1)$ and $\psi_{\mathrm{q}}(\mathbf{x}_2)$. Then, the total wave function for the singlet Ψ_{S} and triplet Ψ_{T} can be written as:

$$\Psi_{\mathrm{S}} = \frac{1}{\sqrt{2}}[\psi_{\mathrm{p}}(\mathbf{x}_1)\psi_{\mathrm{q}}(\mathbf{x}_2) + \psi_{\mathrm{p}}(\mathbf{x}_2)\psi_{\mathrm{q}}(\mathbf{x}_1)]\chi_{\mathrm{S}}\ (s=0) \tag{2.1a}$$

$$\Psi_{\mathrm{T}} = \frac{1}{\sqrt{2}}[\psi_{\mathrm{p}}(\mathbf{x}_1)\psi_{\mathrm{q}}(\mathbf{x}_2) - \psi_{\mathrm{p}}(\mathbf{x}_2)\psi_{\mathrm{q}}(\mathbf{x}_1)]\chi_{\mathrm{T}}\ (s=1) \tag{2.1b}$$

Assuming that both the spin parts are normalised the difference in the electrostatic energies of the two states is:

$$E_{\mathrm{S}} - E_{\mathrm{T}} = 2\int \psi^*_{\mathrm{p}}(\mathbf{x}_1)\psi^*_{\mathrm{q}}(\mathbf{x}_2)V\psi_{\mathrm{p}}(\mathbf{x}_2)\psi_{\mathrm{q}}(\mathbf{x}_1)d\mathbf{x}_1 d\mathbf{x}_2, \tag{2.2}$$

where V denotes the potential due to the Coulomb interaction. This difference in energy is an electrostatic term due to the exchange of two identical particles and is used to define the exchange constant:

$$J = \frac{E_{\mathrm{S}} - E_{\mathrm{T}}}{2} \tag{2.3}$$

Stoner showed that if the gain from this exchange energy is greater than the increase in kinetic energy from altering the band structure, a spontaneous magnetisation would occur[38]. This becomes stable when the product of the exchange constant and the density of states at the fermi surface $N(\epsilon_F)$ are greater than one and is known as the Stoner criterion:

$$JN(\epsilon_{\mathrm{F}}) > 1 \tag{2.4}$$

Within the transition metals the 3d electrons form a narrow band with a large density of states. The complex structure within this 3d band means that only the three elements Fe, Co and Ni have peaks in $N(\epsilon)$, at or sufficiently near, ϵ_{F}, which fulfils the Stoner criterion at room temperature, as shown in Fig. 2.1 (a).

2.2.1 Spin Polarisation

One of the most important consequences of the spin-split density of states for spintronics is the resulting polarisation of the charge carriers. Materials with large spin polarisation can enhance observed effects due to spin transport[40] and so is a vital parameter for applications. As shown in Fig. 2.1 (b) the exchange interaction causes an energy shift in $N(\epsilon)$ between up- and down-spin electrons. In the case of Ni, it can be seen that ϵ_{F} sits within the d-band for spin-down but above it for spin-up, resulting a different $N(\epsilon_{\mathrm{F}})$ for each spin

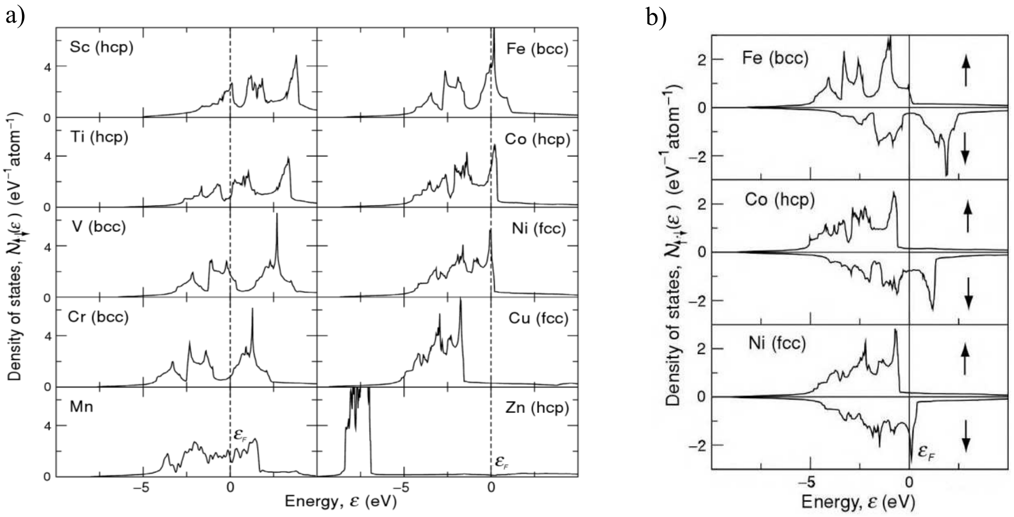

Figure 2.1: a) Calculations of the density of states per atom for the 3d transition metals. In general the 3d sub-bands exhibit a complex structure. This leads to only Fe, Co, and Ni having a value of $N(\epsilon_F)$ large enough to fulfil the Stoner criterion. b) Calculation of the spin split density of states for the 3d ferromagnetic metals. Demonstrates the effect of the exchange interaction, where one of the spin band moves higher in energy with respect to the other. Images from [39]

type. It can also be seen that the polarisation of the whole electron population is not the same as at the Fermi surface, as ϵ_F for the majority ($\uparrow$) electrons sits above the d-band it results in in a smaller $N(\epsilon_F)$ compared to the minority ($\downarrow$) electrons. Since through Fermi's golden rule scattering probabilities, which dictate the conductivity, are proportional to the available states in which to scatter, the two spin species have different conductivities. The two current model, described by Mott[41], where each spin type is viewed as a parallel conduction channel, has had huge success in describing the properties of FM materials[42] and heterostructures through the Valet-Fert model[7]. Thus, a charge current driven through a FM will carry with it a net spin polarisation due to the spin-split $N(\epsilon_F)$. Using the formalism that the spin-up electrons ($\uparrow$) are the majority spins while the spin-down ($\downarrow$) the minority, the polarisation can be defined as:

$$\alpha_F = \frac{\sigma_\uparrow - \sigma_\downarrow}{\sigma_\uparrow + \sigma_\downarrow} \tag{2.5}$$

For most conventional ferromagnetic materials this lies somewhere in the range of 0.1 - 0.7 and is an important tool used in spintronics to create spin asymmetry in other materials. It is worth noting here that the definition of the measured α_F is strongly dependent on the experimental setup[43]. However, the subtleties are more relevant in tunnelling experiments and beyond the scope of this work, where pure spin transport within a nonmagnetic material is the focus.

2.2.2 Anisotropic Magnetoresistance

Ferromagnetic materials are known to exhibit a change in the electrical conductivity depending on the relative orientation of the materials magnetisation **M** and the direction of current flow. The change in resistance is usually of the order of a few percent and was first discovered by Lord Kelvin[1] and has since been named anisotropic magnetoresistance (AMR).

The origin of the effect has undergone much theoretical study based on arguments relating to the ferromagnetic band structure and spin-orbit coupling (SOC). Smit[44] showed that the s-d scattering, a result of the Fermi energy lying within the d-band in the transition metals, is dependent on ϕ—the angle between the electrons momentum **k** and **M**. In general this manifests itself as a reduction of the resistance when the current density **j** and **M** are perpendicular and can be expressed phenomenologically as:

$$\rho_{\parallel} = \rho_{\perp} + \Delta\rho \ \cos^2\phi \tag{2.6}$$

For most ferromagnetic materials $\Delta\rho$ is of the order of a few percent. Measuring the AMR of a ferromagnetic electrode is then a convenient method of determining how the magnetisation behaves in an applied field.

2.3 Spin Injection and Accumulation

As discussed, the spin-split $N(\epsilon)$ within a ferromagnetic material causes different conductivities for spin-up and spin-down electrons, within the limits of the two current model i.e. the spin mixing is sufficiently weak. This has interesting consequences when a charge current is driven across a ferromagnetic/nonmagnetic (FM/NM) interface. Since there is no intrinsic splitting of the spin states in the NM, there must be a redistribution of the charge current across the two spin bands at the interface. Due to the spin-polarised current in the FM, it carries with it an imbalance of spin types and will inject one preferentially into the NM. Therefore, an initial increase in the number of injected spin-ups in the NM must be counteracted by a decrease in spin-downs by an equal amount, in order to maintain charge neutrality. This produces an induced spin splitting in the NM and an accumulation of spins at the interface.

The initial description of this was given by van Son *et al.*[45] through the two current model, which was later formalised through the Boltzmann equation and applied to full heterostructures by Valet and Fert[7]. This interfacial spin accumulation is an important building block within spintronic devices, providing a source of spins within an NM and used to study spin transport. As such, the theoretical framework is accepted and what follows is an overview following the work in reference [36].

The electrical current density **j** of a conductor can be expressed by summing the contributions from electrical field **E** driven and diffusive motion due to gradients in the carrier number density n. With the two current model each spin channel $\sigma =\uparrow,\downarrow$ is considered separately as:

$$\mathbf{j}_\uparrow = \sigma_\uparrow \mathbf{E} - eD_\uparrow \nabla n_\uparrow, \tag{2.7a}$$

$$\mathbf{j}_\downarrow = \sigma_\downarrow \mathbf{E} - eD_\downarrow \nabla n_\downarrow, \tag{2.7b}$$

where e is the magnitude of an electron's charge and $\sigma_{\uparrow(\downarrow)}$ and $D_{\uparrow(\downarrow)}$ are the conductivity and diffusion constant for each spin band. Defining the electrochemical potential (ECP) as $\mu_\sigma = \epsilon_\mathrm{F}^\sigma + e\phi$ where ϕ is the electric potential and $\epsilon_\mathrm{F}^\sigma$ is the Fermi energy, and since $\nabla n_\sigma = N_\sigma(\epsilon_\mathrm{F})\nabla\epsilon_\mathrm{F}^\sigma$, with the Einstein relation $\sigma_\sigma = e^2 N_\sigma(\epsilon_\mathrm{F})D_\sigma$, the current density for each channel can be expressed as:

$$\mathbf{j}_\uparrow = -\frac{\sigma_\uparrow}{e}\nabla\mu_\uparrow, \tag{2.8a}$$

$$\mathbf{j}_\downarrow = -\frac{\sigma_\downarrow}{e}\nabla\mu_\downarrow \tag{2.8b}$$

Hence, the driving force for the spins arises from a gradient in the ECP. The total charge and spin currents are then defined as $\mathbf{j}_\mathrm{c} = \mathbf{j}_\uparrow + \mathbf{j}_\downarrow$ and $\mathbf{j}_\mathrm{s} = \mathbf{j}_\uparrow - \mathbf{j}_\downarrow$ respectively. Through conservation laws the continuity equations of charge and spin in the steady state are obtained as[28]:

$$\nabla\cdot\left(\mathbf{j}_\uparrow + \mathbf{j}_\downarrow\right) = 0, \tag{2.9a}$$

$$\nabla\cdot\left(\mathbf{j}_\uparrow - \mathbf{j}_\downarrow\right) = -e\frac{\delta n_\uparrow}{\tau_{\uparrow\downarrow}} + e\frac{\delta n_\downarrow}{\tau_{\downarrow\uparrow}}, \tag{2.9b}$$

where $\delta n_\sigma = n_\sigma - \bar{n}_\sigma$ is the deviation from the equilibrium carrier density $\bar{n}_\sigma$ for each spin band and $\tau_{\uparrow\downarrow}$ is the characteristic scattering time for spin flip events. Imposing that there should be no net spin scattering in equilibrium (i.e. $N_\uparrow/\tau_{\uparrow\downarrow} = N_\downarrow/\tau_{\uparrow\downarrow}$ where N_σ is the spin-dependent density of states at Fermi energy), then the basic diffusion equations that describe the charge and spin transport are[28, 45]:

$$\nabla^2\left(\sigma_\uparrow\mu_\uparrow+\sigma_\downarrow\mu_\downarrow\right)=0, \tag{2.10a}$$

$$\nabla^2\left(\mu_\uparrow-\mu_\downarrow\right)=\frac{1}{\lambda_s^2}\left(\mu_\uparrow-\mu_\downarrow\right), \tag{2.10b}$$

where $\lambda_\mathrm{s}=\sqrt{D\tau_\mathrm{sf}}$ is the spin diffusion length. D is the spin-averaged diffusion coefficients defined as $D=D_\uparrow D_\downarrow(N_\uparrow+N_\downarrow)/(N_\uparrow D_\uparrow-N_\downarrow D_\downarrow)$ and τ_sf is the spin relaxation time. These equations describe the diffusion of the pure spin current as one moves from the FM/NM interface and can be solved for a given device geometry. The general solution for the electrochemical potential of each spin type is of the form:

$$\mu_\uparrow=a+bx+\frac{c}{\sigma_\uparrow}e^{\frac{-x}{\lambda}}+\frac{d}{\sigma_\uparrow}e^{\frac{x}{\lambda}}, \tag{2.11a}$$

$$\mu_\downarrow=a+bx-\frac{c}{\sigma_\downarrow}e^{\frac{-x}{\lambda}}-\frac{d}{\sigma_\downarrow}e^{\frac{x}{\lambda}} \tag{2.11b}$$

In general the values for μ_σ, σ_σ and λ will differ between the FM and NM regions. Considering a 1D channel that is FM for $x<0$ and NM for $x>0$, as shown in Fig. 2.2 (a), the coefficients can then be determined through the boundary conditions where the materials meet. In a simple model, where it is assumed that the interfaces are transparent and do not cause spin flip scattering, the boundary conditions are:

- the electrochemical potentials for each spin band are continuous at the interface
- the spin currents $\mathbf{j}_\uparrow$ and $\mathbf{j}_\downarrow$ are conserved at the interface
- the charge current density $\mathbf{j}_\mathrm{c}=\mathbf{j}_\uparrow^\mathrm{FM}+\mathbf{j}_\downarrow^\mathrm{FM}=\mathbf{j}_\uparrow^\mathrm{NM}+\mathbf{j}_\downarrow^\mathrm{NM}$ is constant everywhere
- far from the interface ($x=\pm\infty$) there is no spin accumulation ($\mu_\uparrow=\mu_\downarrow$)

Van Son *et al.* applied this to a transparent FM/NM interface in the presence of a charge current across the boundary[45]. The consequence of this was two fold. Firstly an interfacial spin resistance R_I was found:

$$R_\mathrm{I}=\frac{\Delta\mu}{eI}=\frac{\alpha_\mathrm{F}^2(\sigma_\mathrm{N}^{-1}\lambda_\mathrm{N})(\sigma_\mathrm{F}^{-1}\lambda_\mathrm{F})}{(\sigma_\mathrm{F}^{-1}\lambda_\mathrm{F})+(1-\alpha^2)(\sigma_\mathrm{N}^{-1}\lambda_\mathrm{N})} \tag{2.12}$$

where α_F is the FM spin polarisation and σ_i and λ_i are the conductivities and spin diffusion length in the N = NM and F = FM. This can be seen in Fig. 2.2 (b) where the differences in the spin averaged chemical potential is visible at the interface and can be measured as a potential difference between the two materials $\Delta\mu/e$. The second is that the ECPs of the each spin band split, indicating a spin accumulation at the interface due to injection of a spin-polarised current. Within the FM there is a suppression of the spin polarised current within a length scale of $\approx \lambda_F$ due to a back flow of spins caused by the accumulation at the interface. However, in the NM the splitting of the ECP and resulting gradient $\nabla(\mu^N_\uparrow - \mu^N_\downarrow)$ drives a pure spin current into the bulk of the NM as shown in Fig. 2.2 (c). It is this generation and transportation of the pure spin current in the NM that is the focus of this work.

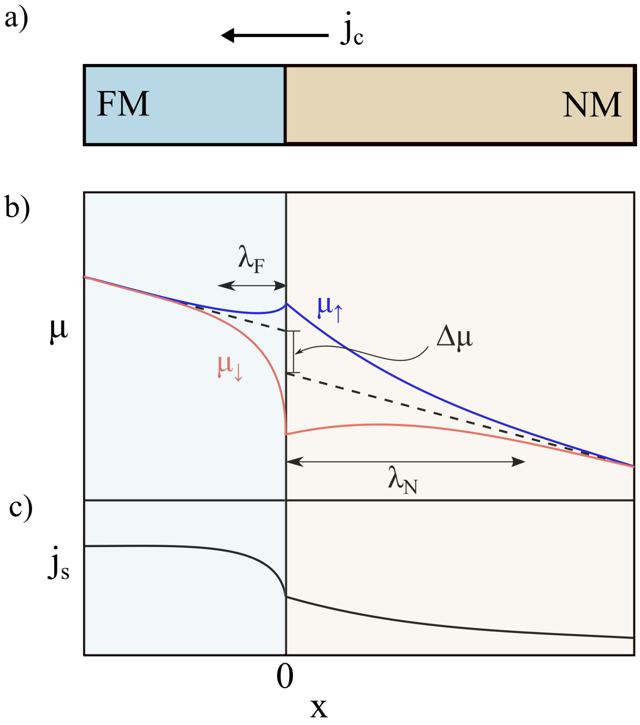

Figure 2.2: a) Schematic of a FM/NM interface with a charge current $\mathbf{j}_c$ flowing from the NM to the FM. The drives electrons fro the FM into the NM. b) Schematic showing the ECP for spin-up ($\mu_\uparrow$) and spin-down ($\mu_\downarrow$) in both the FM and NM. At the interface, due to the difference in conductivities of the the spin species the ECPs split forming an accumulation of up-spins. c) Show the change in spin current across the interface where $\mathbf{j}_s = \mathbf{j}_\uparrow - \mathbf{j}_\downarrow = \frac{-1}{e}\left(\sigma_\uparrow \nabla\mu_\uparrow - \sigma_\downarrow \nabla\mu_\downarrow\right)$. The spin accumulation causes a small back flow into the FM reducing $\mathbf{j}_s$ near the interface. The spin current also diffuses into the NM and decays over the spin diffusion length λ_N

2.3.1 Lateral Spin Valves

The spin accumulation at an FM/NM interface can be measured through the fabrication of a lateral spin valve (LSV) as shown in Fig. 2.3 (a). A charge current is injected through FM1 and drained out the device to the left hand side of the NM causing spin accumulation in the NM. One can see from the solutions to equation 2.10 that the spin accumulation will exponentially decay along the length of the NM due to spin-flip scattering. Figure 2.3 (b) is a schematic representation of the ECP for both spin types in a LSV and shows this decay. If a second FM contact is placed a distance L along the NM wire then the spin splitting can be detected. At the detection interface the condition that the ECPs for each spin band remain constant further induces spin splitting of the ECPs in FM2. Due to the spin asymmetry already present in the FM, the neutrality point far from the interface will be shifted compared to the NM by the amount $\Delta\mu$. This potential difference can be detected through an open circuit voltage measurement, as shown in Fig. 2.3 (a). Upon applying a magnetic field in order to switch the magnetisation of FM2, the spin asymmetry is reversed and a change in the measured potential is detected. This change in potential with magnetic field is an indication of the magnitude of the spin accumulation and diffusive pure spin current in the NM.

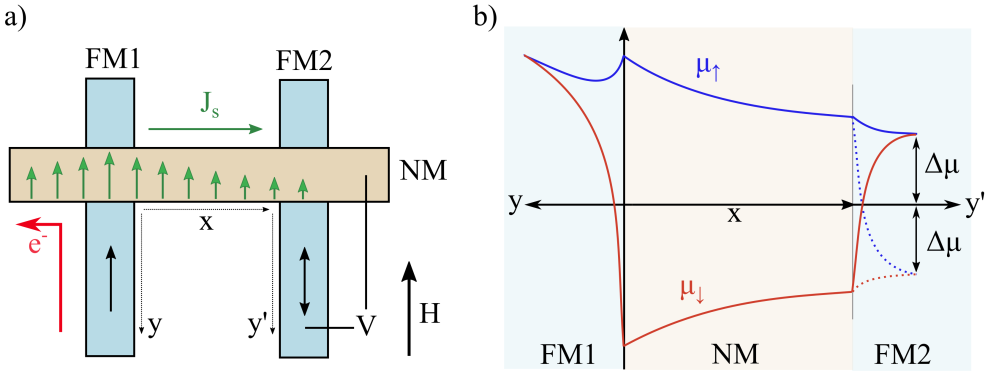

Figure 2.3: a) Schematic diagram of a LSV. FM1 is the injector electrode where a charge current drives electrons into the NM, causing spin accumulation. The spins diffuse through the NM and are detected at FM2. b) Schematic of the ECP for spin-up (blue) and spin-down (red). The spin dependent voltage $\Delta V = \Delta\mu/e$ is measure between FM2 and NM. The dotted lines indicate case for AP alignment of FM1 and FM2.

Through a similar approach to the simple FM/NM interface, by applying the correct boundary conditions to the generalised solution 2.11 an expression for the nonlocal voltage measured at the detector normalised to the injection current is obtained as:

$$\Delta R_{\mathrm{s}} = \frac{2\Delta V}{eI_{\mathrm{c}}} = \frac{4\alpha_{\mathrm{F}}^2 R_{\mathrm{F}}^2}{(1-\alpha_{\mathrm{F}}^2)^2 R_{\mathrm{N}}} \frac{e^{-L/\lambda_{\mathrm{N}}}}{(1+\frac{2R_{\mathrm{F}}}{(1-\alpha^2)R_{\mathrm{N}}})^2 - e^{-2L/\lambda_{\mathrm{N}}}}, \tag{2.13}$$

where the spin resistances are defined as $R_{\mathrm{F}} = \rho_{\mathrm{F}}\lambda_{\mathrm{F}}/A_{\mathrm{F}}$ and $R_{\mathrm{N}} = \rho_{\mathrm{N}}\lambda_{\mathrm{N}}/A_{\mathrm{N}}$ and are a measure of how well each material will act as a spin sink[46]. The areas A are those perpendicular to the flow of the spin current i.e. $A_{\mathrm{F}} = w_{\mathrm{F}} w_{\mathrm{N}}$ and $A_{\mathrm{N}} = w_{\mathrm{N}} t_{\mathrm{N}}$.

In defining the boundary conditions for the calculation of Eq. 2.13, once again the assumption of transparent contacts was made. The relaxation of the continuity of the ECP at the interface can lead to very different dependence of ΔR_{s} on L[28]. This is most prominent in LSVs that include tunnel barriers at the injector/detector interface, which limits the interaction between the FM detector and the spin accumulation in the NM. However, as is demonstrated in Chapter 4, the devices fabricated within this study are all in the transparent contact regime, and as such is the only case considered here.

2.3.2 Hanle Spin Precession

When a perpendicular magnetic field $B_{\perp}$ is applied to a LSV a torque is exerted on the spin angular momentum of the electrons carrying the spin current. This results in Larmor precession with a frequency:

$$\omega_{\mathrm{L}} = \frac{g\mu_{\mathrm{B}} B_{\perp}}{\hbar}, \tag{2.14}$$

where g, μ_{B} and $\hbar$ are the g-factor, Bohr magneton and reduced Plank's constant respectively. As shown in Fig. 2.4 (a) this causes the spins to rotate as they diffuse along the NM track. Once at the detector, the injected spins will have rotated through an angle $\phi = \omega_{\mathrm{L}} t$ where t is the time of flight for the electrons to travel from FM1 to FM2. The detection of the spin current by FM2 is sensitive only to the projected component of the spin density in the NM onto its own magnetisation direction (fixed along the y-axis due to shape anisotropy). This causes the resulting spin accumulation at the detector to vary as $\cos\phi$ and is called Hanle spin precession. For the simple case of a single transit-time the precession angle depends only on the applied field. Figure 2.4 (b) shows the normalised nonlocal signal due to Hanle precession as a function of ϕ. The two curves show the expected behaviour for a LSV

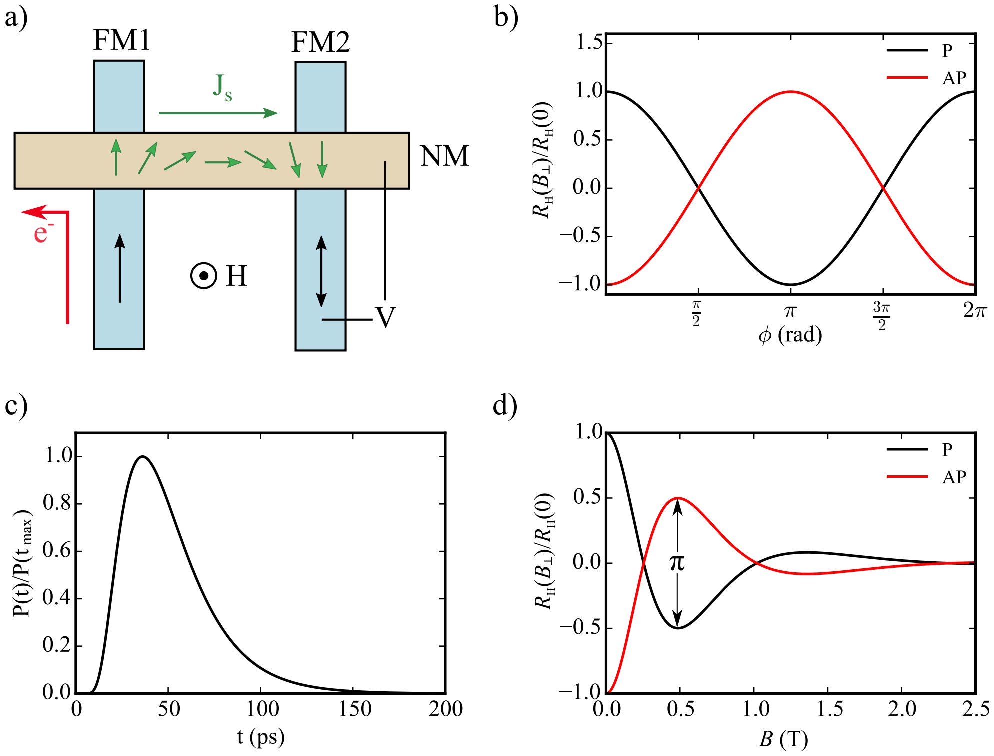

Figure 2.4: a) Schematic of a LSV in the Hanle spin precession geometry. The out of plane field applied a torque to the spin current causing the diffusing spins to precess. b) Normalised nonlocal Hanle signal as a function of precession angle ($\phi = \omega_L t$) of arriving spins at FM2 for a single transit time t. c) Probability distribution function (Eq. 2.15) for a LSV with $L = 2$ µm and $\tau_{sf} = 20$ ps. d) Simulated Hanle curve for P and AP initial configurations. The two curves reverse sign completely when the majority of spins arrive with a precession angle of π.

initialised in the P and AP configurations before applying a perpendicular field and the two states maintain a π phase shift with respect to each other.

Since the conduction within structures in this work is diffusive, there is not one single transit-time t but a distribution of times, and as such precession angles. The probability distribution function for the time of flight between the injector and detector in a 1D conductor can be expressed as:

$$P(t) = \sqrt{1/4\pi Dt}\, e^{-L^2/4Dt} e^{-t/\tau_s} \tag{2.15}$$

The second exponential term here accounts for the probability of a spin flip during diffusion time t. This distribution is shown in Fig. 2.4 (c) and exhibits a peak with an exponential decay reducing the chance of long transit times. The total signal at the detector is thus proportional to a summation over all possible transit times, as each electron arrives having undergone rotation through an angle $\phi = \omega_L t$. This is expressed as:

$$R_H(B_\perp) \propto \int_0^\infty P(t) \cos\phi \, dt \tag{2.16}$$

where $R_H = V_H/I$ is the nonlocal voltage from Hanle spin precession normalised to the injection current. This distribution of transit times causes a dephasing of the spin density at FM2 and results in a damping of the measured signal. This is shown in the simulation of a Hanle signal measured from a LSV in Fig. 2.4 (d). The oscillatory signal is still present but the diffusive nature of the spin transport means the total signal quickly decays.

Crucially, this approach does not account for the type of FM/NM interface and anisotropic absorption of spins[47, 48]. Idzuchi *et al.* demonstrated that when ohmic contacts are used the increased spin absorption at the interface alters the distribution of transit times, resulting in a faster diffusion of spins. They then formulate a new model including considerations of ohmic contacts and the different absorption and relaxation mechanisms for transverse and longitudinal spin currents. This is found through solving the diffusion-modified Bloch-Torrey equation[49–51] with a complex representation of a spin current $I_s = I_s^y + iI_s^x$. The details are beyond the scope of this thesis and the reader is directed to references [47, 51] for details of the derivation. Finally, it is worth noting that in the limit of high resistance interfaces (i.e. tunnel junctions) then the above reduces to give the same form as Eq. 2.16.

2.4 Spin Relaxation

The spin accumulation at an FM/NM interface causes the diffusion of a pure spin current throughout the NM. The magnitude of this spin current will decay over a characteristic length scale λ_s which is governed by the spin relaxation mechanisms in the material. For an ensemble of spins in an applied field the dephasing/relaxation can be described through the Bloch-Torrey[52, 53] phenomenological equations, with two relaxation times T_1 and T_2. The spin relaxation time T_1 (also called the longitudinal or spin-lattice time) is the characteristic time for the spins, collinear to the applied field, to equilibrate, generally through phonon interactions. The dephasing time T_2 (transverse or decoherence time) is the time for an ensemble of spins, transverse to an applied field, precessing in phase around the field direction to lose their coherence through fluctuations in the precession frequencies. In isotropic and cubic solids, in zero or small applied fields, these two relaxation times are equivalent.

Essentially, if the random phase fluctuations gained by the electron in time τ_c provides an uncertainty in the energy greater than the Zeeman splitting between the two spin orientations, then the dephasing field acts equally on transverse and longitudinal spins and $T_1 = T_2$. The conditions that $\omega_L\tau_c \ll 1$ (i.e. small magnetic field) where τ_c is a correlation time, defined as $1/\tau_c$ being the rate of change of the effective dephasing magnetic field, is well observed for the field values within this work, $\ll 1$ T. Since Cu is the material of concern for spin transport throughout this thesis, it is assumed that there is only one spin relaxation time $T_1 = T_2 = \tau_{sf}$. Although a single relaxation time for the spin ensemble will be assumed, there can be many different scattering mechanisms.

2.4.1 Elliot-Yafetet

In clean nonmagnetic materials the dominant process for spin relaxation is provided through spin-orbit coupling (SOC) as described by Elliot and Yafet[29, 30]. The introduction of the SOC interaction in the Hamiltonian takes the form

$$V_{SOC} = \frac{\hbar}{4m^2c^2}\nabla V_{sc} \times \hat{\mathbf{p}} \cdot \hat{\sigma}, \tag{2.17}$$

where V_{sc} is the scalar (spin-independent) periodic lattice potential, $\hat{\mathbf{p}} = -i\hbar\nabla$ is the momentum operator and $\hat{\sigma}$ are the Pauli spin matrices. As a consequence of this interaction the single-electron Bloch wave functions are no longer eigenstates of the $\hat{\sigma}_z$ but instead become superpositions of the spin-up $|\uparrow\rangle$ and spin-down $|\downarrow\rangle$ states. For the case of metals with inversion symmetry Elliot wrote these new states, for electrons of momentum $\mathbf{k}$ and band index n, as:

$$\Psi_{\mathbf{k}n\uparrow}(\mathbf{r}) = [a_{\mathbf{k}n}(\mathbf{r})|\uparrow\rangle + b_{\mathbf{k}n}(\mathbf{r})|\downarrow\rangle]e^{i\mathbf{k}\cdot\mathbf{r}} \tag{2.18a}$$

$$\Psi_{\mathbf{k}n\downarrow}(\mathbf{r}) = [a^*_{-\mathbf{k}n}(\mathbf{r})|\downarrow\rangle - b^*_{-\mathbf{k}n}(\mathbf{r})|\uparrow\rangle]e^{i\mathbf{k}\cdot\mathbf{r}} \tag{2.18b}$$

Since SOC is, in general, much smaller than the kinetic and potential energy terms within the Hamiltonian, it can be considered as a perturbation. Thus, the values of $|a|$ can be close to unity, while $|b| \ll 1$, and it becomes convenient to call $\Psi_{\mathbf{k}n\uparrow}(\mathbf{r})$ and $\Psi_{\mathbf{k}n\downarrow}(\mathbf{r})$ “spin-up" and“spin-down" respectively. However, this mixing of the spin states does not in itself lead to spin relaxation, but requires the presence of momentum relaxation where each scattering event can couple $\Psi_{\mathbf{k}n\uparrow}(\mathbf{r})$ and $\Psi_{\mathbf{k}n\downarrow}(\mathbf{r})$ allowing transitions between the two. As such, the spin relaxation events will follow the same temperature dependence as the electronic momentum scattering rate $1/\tau_{\mathrm{e}}$, dominated by phonons at high temperatures and nonmagnetic impurities and grain boundaries at low temperature.

Further to this Yafet[30] discussed another spin relaxation method where a periodic lattice-ion induced spin-orbit interaction is modified by phonons and can directly couple Pauli up- and down-spin states. Yafet showed that this spin relaxation was closely related to the electrical resistivity. In general the combined Elliot-Yafet mechanism of spin relaxation can be summed up through the expression:

$$\frac{1}{\tau_{\mathrm{sf}}} = \frac{\varepsilon}{\tau_{\mathrm{e}}}, \tag{2.19}$$

where ε is a temperature independent constant that links the momentum and spin-relaxation rates through SOC.

2.4.2 The Kondo effect

Impurities in nonmagnetic materials mainly provide a temperature independent contribution to the momentum and hence spin relaxation. However, certain impurity/host combinations allow the formation of a local moment on the impurity and this extra degree of freedom causes temperature dependent scattering through the Kondo effect[33]. The formation of the local moment can be described though a virtual bound state (VBS) or Anderson model[54]. For a 3d impurity ion in a free-electron like metal host there are four important terms in the Hamiltonian:

$$\mathscr{H} = KE_{\mathrm{s}} + KE_{\mathrm{d}} + V_{\mathrm{sd}} + U_{\mathrm{dd}} \tag{2.20}$$

The first two terms are the individual kinetic energies for the s and d electrons respectively. The third represents the hybridisation interaction between the s and d electrons, while the final is the intra-atomic Coulomb repulsion of the lowest d orbital of opposite spin. Figure 2.5 (a) shows a schematic of the density of states $N(\epsilon)$ for up- and down-spins in the host materials s-band along with a localised d-impurity level, below the fermi energy and in the absence of hybridisation. When s-d mixing and the intra-atomic Coulomb interactions are switched on the effects are three fold. The first consequence of the hybridisation is to shift the energy of the impurity state down with respect to the Fermi energy ϵ_{F} to:

$$\epsilon_{\mathrm{d}} \approx \frac{2N(\epsilon_{\mathrm{F}})|V_{\mathrm{sd}}|^2}{D}, \tag{2.21}$$

where D is the s-bandwidth. Secondly the mixing induced a broadening to the impurity state to a width:

$$2\Gamma \approx 2\pi N(\epsilon_F)|V_{sd}|^2 \tag{2.22}$$

The final result is an energy shift U between the spin-up and spin-down levels caused by the Coulomb repulsion. Figure 2.5 (b) is a schematic demonstrating the above for the case of a strongly magnetic impurity, where the spin-down VBS is shifted above ϵ_F and is unoccupied. Thus, depending on the exact properties of the DOS of the host and impurity, both ϵ_d and U can vary altering the magnetic behaviour of the impurity. For example, if it occurs that both spin-up and spin-down VBS exist either completely below or above ϵ_F, then there will be no moment on the impurity. Alternatively one or both VBS can intersect ϵ_F and form an impurity with a non-half-integer spin moment. A typical example of this are dilute alloys of Ni or Fe in Cu where only Fe impurities have a moment[55].

Systems where dilute magnetic impurities are dissolved in a nonmagnetic host result in a resistance minimum at low temperatures, as shown in Fig. 2.6 (a). At low temperatures phonon scattering is reduced and the interaction between the conduction electrons and

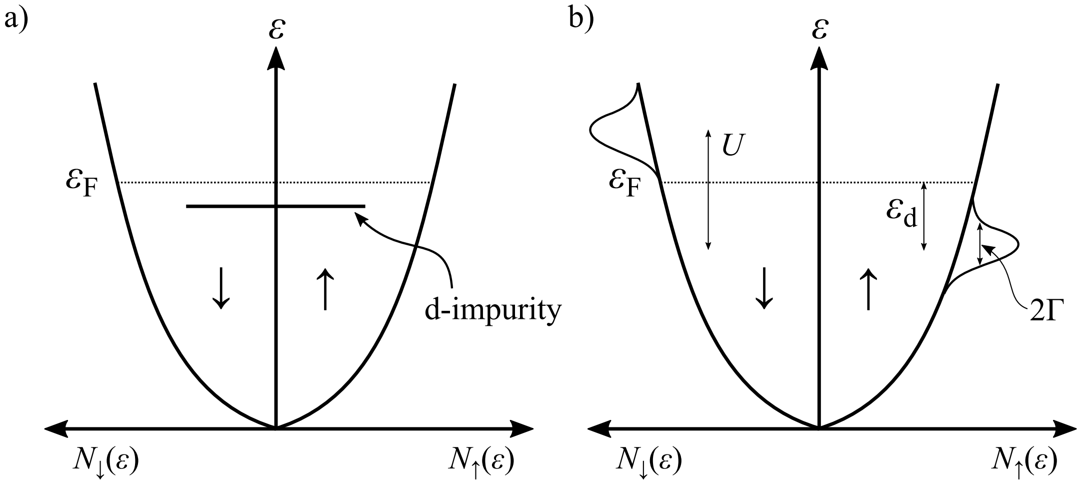

Figure 2.5: a) Schematic of the spin-dependent DOS for a free-electron like metal. The host's s-band is shown with an isolated impurity level below ϵ_F. b) After turning on the s-d hybridisation and coulomb interaction the d-impurity state broadens and moves in energy to ϵ_d. The Coulomb interaction U causes a shift in energy for the impurity band for the two spin states. Here the case for a strong ferromagnetic impurity state is shown, where U causes the down-spin state to sit above the Fermi energy while the up-spin state is entirely below the Fermi surface.

the magnetic impurities dominates causing an increase in the resistivity that can eventually plateau as the magnetic impurities become screened[56]. It was Kondo that developed the first theory to describe the negative temperature coefficient at low temperatures through a 2$^{\text{nd}}$ order perturbation method[33]. The result of the second Born approximation gives a scattering probability of the form

$$P_{\mathbf{k}\to\mathbf{k}'} \propto \frac{2\pi}{\hbar}\left(V_{\mathbf{k}\mathbf{k}'}V_{\mathbf{k}'\mathbf{k}} + \sum_{\mathbf{q}\neq\mathbf{k}} \frac{V_{\mathbf{k}\mathbf{k}'}V_{\mathbf{k}'\mathbf{q}}V_{\mathbf{q}\mathbf{k}}}{E_{\mathbf{k}} - E_{\mathbf{q}}} + cc\right) \tag{2.23}$$

where $V_{\mathbf{k}\mathbf{k}'} = \langle\phi_{\mathbf{k}}|\, V\, |\phi_{\mathbf{k}'}\rangle$. This can be interpreted as the total scattering probability of going directly from the initial **k** to final $\mathbf{k}'$ state, together with the probability of scattering via an intermediate state **q**. It is the scattering via this intermediate state that is important for the Kondo effect, as it involves consideration of the internal degree of freedom of the impurities moment. Figures 2.6 (b)-(e) shows the four possible scattering processes which conserves the initial and final spin state of the electron. Figure 2.6 (b) shows the straight forward 'direct' process, where $|\mathbf{k}\uparrow\rangle$ initially scatters into the intermediate state $|\mathbf{q}\uparrow\rangle$, conserving the spin. This then scatters into the final state $|\mathbf{k}'\uparrow\rangle$ further maintain the same spin. In (d) the reverse order of this is shown, where $|\mathbf{q}\uparrow\rangle$ scatters into the final state $|\mathbf{k}'\uparrow\rangle$ followed by $|\mathbf{k}\uparrow\rangle$ scattering into $|\mathbf{q}\uparrow\rangle$, with both events conserving the electrons spin. This process is called the 'exchange' of the first due to the swapping of the scattering order. The mechanisms (c) and (e) then show the direct and exchange scattering where the intermediate state is now spin-down and hence involves a spin flip. Figures 2.6 (f)–(i) show similar events but where the final state has the opposite spin. Crucially, the scattering amplitude for direct and exchange processes where at least one transition involves a spin-flip are different. When these individual amplitudes are summed they provide a contribution to the resistivity ~ lnT. Kondo's result for the resistivity due to a concentration of magnetic impurities c with a spin moment S is:

$$\rho_{\mathrm{m}} = \rho_{\mathrm{K}}\ln\mathrm{T}, \tag{2.24}$$

where z is the number of conduction electrons per atom and:

$$\rho_{\mathrm{K}} = c\left[1 + \frac{3zJ}{\epsilon_{\mathrm{F}}}\right]\frac{3\pi m J^2 S(S+1)(V/N)}{2e^2\hbar\epsilon_{\mathrm{F}}} \tag{2.25}$$

Here m is the free electron mass, V the total volume of the crystal and N total number of atoms. J represents the magnitude of the direct exchange interaction between the localised

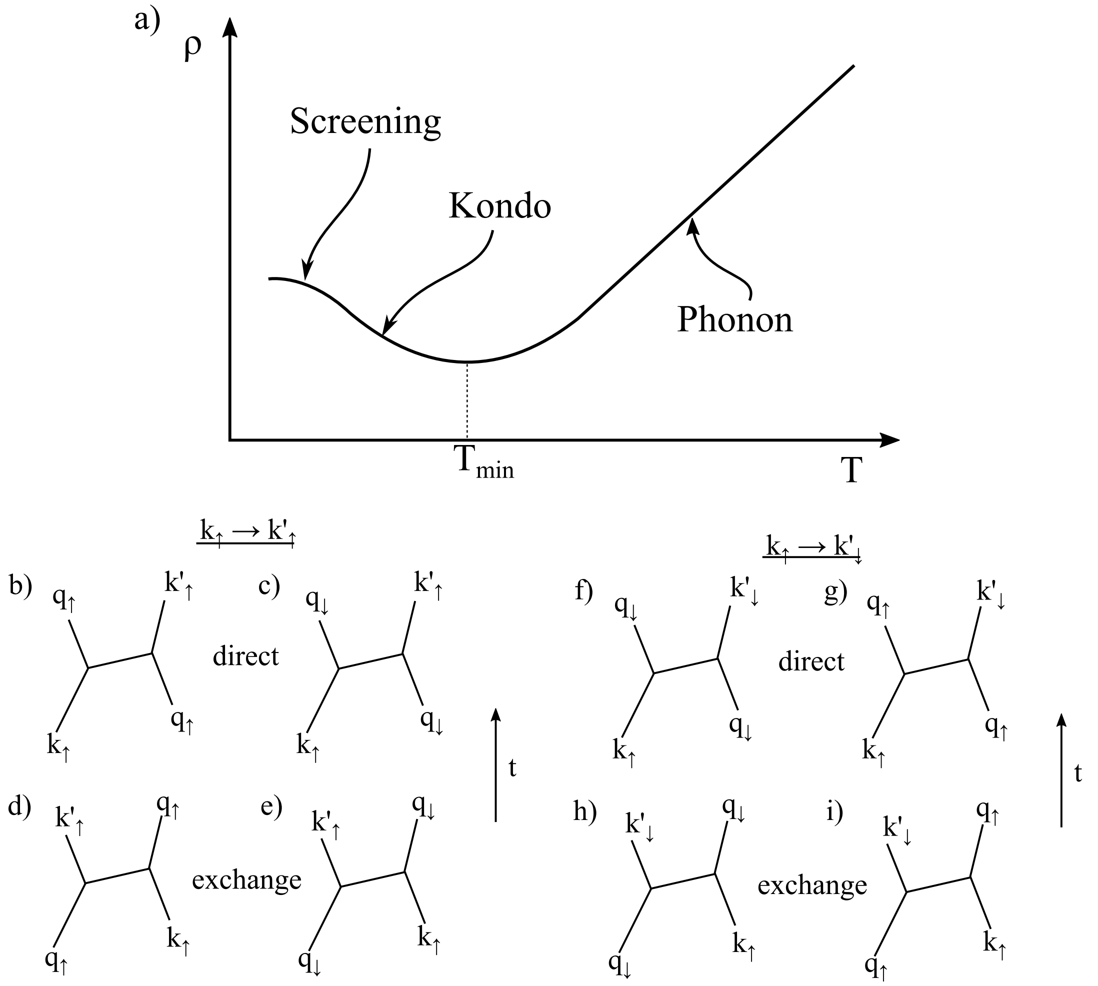

Figure 2.6: a) Typical curve for resistivity as a function of temperature for a dilute ferromagnetic alloy. At high temperatures scattering from phonons dominates the resistivity. Below a critical temperature (T_{min}) scattering form the magnetic impurities causes the resistivity to rise. At very low temperatures the resistivity can reach a maximum as the conduction electrons screen the magnetic impurities[56]. d) – e) Diagrams detailing the different 2^{nd} order scattering events that conserve the initial and final spin state. b) and d) involve no spin-flip scattering at all while c) and e) scatter with an intermediate state of opposite spin. Time flows vertically. f) – i) Four scattering events for a case where the initial and final spin are not conserved.

and conduction electrons which can be either positive (ferromagnetic coupling) or negative (antiferromagnetic coupling). The important result in Kondo's work is that the resistivity has an odd dependence on J, and so antiferromagnetic coupling (negative J) can accurately reproduce the experimentally observed negative temperature coefficient at low temperatures.

Although Kondo scattering can preserve the spin of the conduction electron it can also cause spin-flip events, as shown in Fig. 2.6 (f)–(i). However, the calculation of each scattering amplitude is beyond the scope of this thesis and instead a phenomenological approach is used. In a similar manner to the Elliot-Yafet mechanism, it is assumed that each Kondo scattering event has a certain probability of flipping the spin of the conduction electron ε_{m}, and the spin-flip scattering rate from magnetic impurities is:

$$\frac{1}{\tau_{\mathrm{sf}}^{m}} = \frac{\varepsilon_{\mathrm{m}}}{\tau_{\mathrm{m}}} \tag{2.26}$$

where $1/\tau_{\mathrm{m}} = ne^2\rho_{\mathrm{m}}/m$ and n is the conduction electron density. The formation of a local moment on the impurity can exist up to room temperature[57] and in general ε_{m} is much bigger than the equivalent for phonons or nonmagnetic impurities. Consequently, Kondo scattering can be a very effective mechanism for spin relaxation and is discussed in more detail in Chapter 5.

2.5 Simulations

Simulations using the finite element method (FEM) have been used in two cases in this thesis, to perform micromagnetic simulations and the solving Poisson's equation. FEM is a numerical method for solving partial differential equations (PDEs), where through an iterative approach an equation can be solved by minimising the result against a set of test functions. This is performed within each cells across a mesh representing the sample. Micromagnetic simulations are performed to aid the design of FM electrodes, avoiding lengthy fabrication procedures of devices containing electrode with undesirable switching fields. Along with this, finite element modelling has been used to solve Poisson's equation to obtain the electric potential in 3D structures due to an applied current.

2.5.1 Micromagnetics

In order to simulate the reversal of a magnetic electrode due to an external applied field the commercially available software OOMMF was used[58]. The Landau-Lifschitz equation is a phenomenological description of the dynamics for a magnetic moment within an applied field

$$\frac{d\mathbf{M}}{dt} = -\gamma\mathbf{M}\times\mathbf{H}_{\mathrm{eff}} - \frac{\alpha\gamma}{M_{\mathrm{s}}}\mathbf{M}\times(\mathbf{M}\times\mathbf{H}_{\mathrm{eff}}) \tag{2.27}$$

where γ is the gyromagnetic ratio, $\mathbf{H}_{\mathrm{eff}}$ is an effective field combining the external applied field with the internal demagnetising field and α is a parameter representing the damping in the system. OOMMF solves the Landau-Lifschitz equation for a set of 3D spins across a mesh of 2D cells by minimising the magnetostatic energy. The meshes used are idealised representations of the FM electrodes required with a cell size of 5 nm. The values for the exchange constant A and saturation magnetisation M_{s} used were 13×10^{-12} J/m and 800 kA/m respectively.

2.5.2 Solving Poisson's Equation

Poisson's equation is a PDE and is used in many areas of physics. It relates a scalar potential to a source function. In this case the potential generated due to a charge current density is required. Ohm's law states that $j=\sigma E$, where E is the electric field within the conductor and related to the scalar potential by $E=-\nabla V$. Since, for a constant current density $\nabla j = 0$ we obtain:

$$\nabla^2 V = 0 \tag{2.28}$$

which can be solved to find the electrostatic potential, given the charge current density boundary conditions, in a 3D mesh. This is performed by using Sfepy[59], a freely available python package. The current density is fixed at the source with a second boundary condition of zero potential at the drain. The potential difference with respect to the drain is then calculated throughout the defined mesh. The dimensions and material parameters are all taken from experimental values obtained from the measured devices.

CHAPTER 3

Experimental methods

3.1 Introduction

Nano-fabrication encompasses a wide range of techniques, many seen throughout industry and readily available through commercial set-ups. The fabrication of LSVs however, is often achieved through the unconventional method of shadow lithography and angled deposition, due to the high quality interfaces the technique provides. The work presented in this thesis required the set up of this complex procedure and saw the first devices fabricated in such a way here at Leeds. Central to this was the design and building of a bespoke ultra high vacuum (UHV) deposition system that allows the sample to be rotated through a range of angles relative to the deposition source. Along with this, the development of a double-dose electron-beam lithography (EBL) technique provides high precision control of individual layers of resist. The combination of these two techniques allows the *in situ* deposition of lateral structures involving up to three different materials, providing high quality interfaces between each material. This work has also required the design and construction of new equipment for the characterisation of LSVs. The small signals and delicate nature of the nano-structures called for new sample heads and measurement sticks for the cryostats to be made, in order to reproducibly and reliably measure them. This chapter will detail the equipment built and used, along with the methods developed for the fabrication of lateral structures.

3.2 Device Fabrication

Devices have been fabricated through a mixture of conventional and shadow lithography techniques. Throughout this thesis positive resist processing is used, where the exposed regions of polymer undergo chain scission becoming soluble when placed in developer solution. A schematic of a typical final device structure is shown in Fig. 3.1. The whole process involves three lithographic steps: conventional EBL, optical lithography (OL), and shadow lithography. Samples were fabricated on Si/SiO$_2$(100 nm) substrates. The substrates were cleaned in an oxygen plasma asher for 5 mins at 50 W followed by sonication in acetone and finally isopropyl alcohol (IPA) to remove any residues. The cleaning process is repeated between each lithography stage to ensure the removal of any remaining resist. The inner contacts were defined first, using EBL and deposited via electron-beam evaporation, and are shown in Fig. 3.1 (b). The inner contacts step includes the patterning of alignment markers for the overlay of the final lithography layer. Figure 3.1 (a) shows the design used

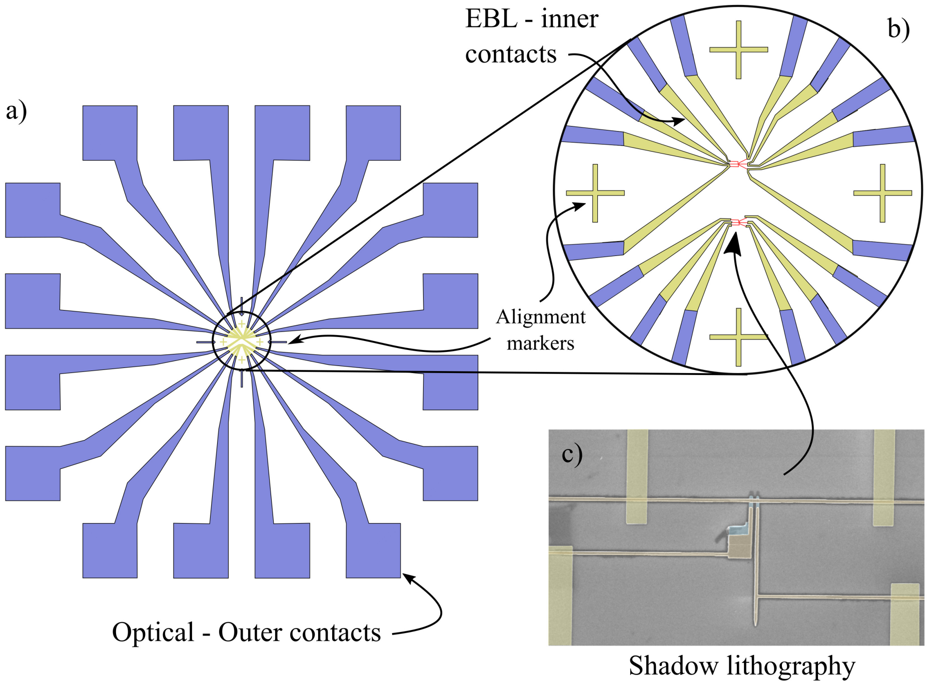

Figure 3.1: Over view of a typical device fabricated in this thesis. a) Design of the outer contacts patterned with OL. The 300 × 300 µm square pads are used to wire bond to. b) Close up of the central region showing the inner contacts defined though EBL. Crosses are chip marks used for EBL alignment. c) False colour SEM image of a LSV. Shows the overlap with the inner contacts. This final stage is fabricated through a shadow lithography technique.

for the outer contacts, patterned through OL and sputter deposited. Together the two stages of contacts bridge between the ~100 nm wide wires of the LSV to the 300 × 300 µm pads used to wire bond electrical connections to the device. In both stages a Cr/Au bilayer was used, where the Cr provides adhesion to the substrate and Au good electrical conductivity. The outer contacts (Cr[5 nm]/Au[50 nm]) are thicker than the inner (Cr[5 nm]/Au[30 nm]) to ensure a good overlap and continuity across the two lithography steps. The final stage was made through shadow deposition and parameters vary depending on the device. Figure 3.1 (c) shows a typical LSV where Py was evaporated at 45° to the substrate, followed by Cu at normal incidence. The optical mask consists of nine copies of the design shown in Fig. 3.1 (a) on a 3 by 3 grid, allowing the simultaneous fabrication of nine chips on a single substrate. In general, each of nine chips has a slight variation in the LSV (typically the separation of FM electrodes L) providing a full sample set in a single deposition. Once all fabrication processes are complete, a protective layer of resist was spin coated onto the devices and allowed to harden without baking. The substrate was then diced on a Microace 66 wafer saw into individual chips to fit into the sample head. The fabrication process was performed in cleanroom conditions with the exception of the angled deposition. The samples were transported to the angled deposition system in an evacuated portable desiccator to minimise any contamination.

3.2.1 Conventional Lithography

Conventional lift-off lithography is a well established technique for nanofabrication. The basic outline of a positive resist process used in this work is shown in Fig. 3.2. The use of a bilayer resist is crucial, as the support resist has a higher sensitivity to the radiation used in the exposure, resulting in a natural undercut once developed, see Fig. 3.2 (d). This prevents the deposited material linking from the substrate onto the side wall of the resist leading to poor lift-off, either through delamination or leaving ridges at the edge of the material

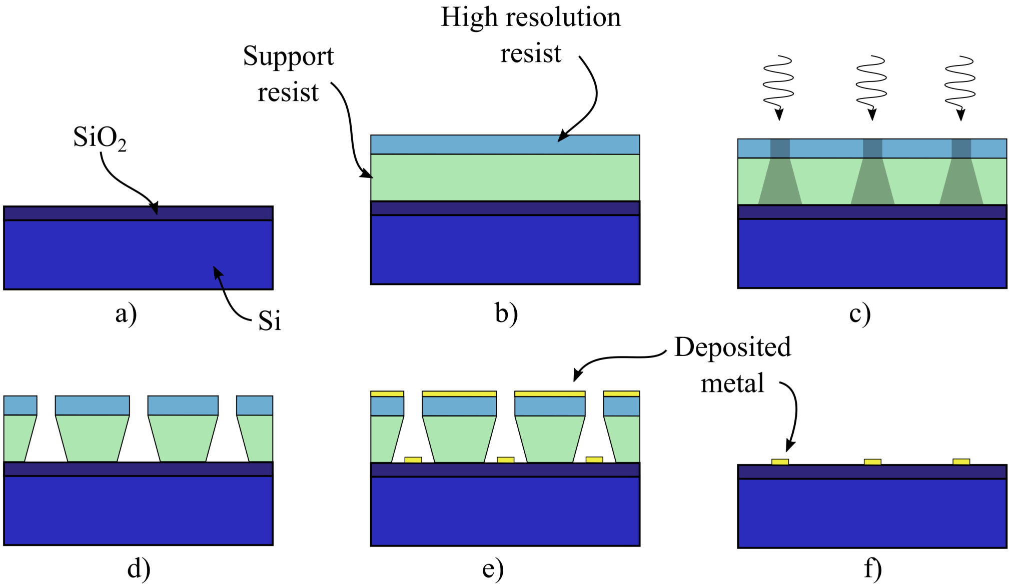

Figure 3.2: Processes involved in conventional lift-off lithography. a) Cleaned Si/SiO_2 substrate. b) Two layers of resist are independently spin coated on the substrate and baked. The Support resist is usually more sensitive to provide an undercut. c) Exposure. d) Development in solution. e) Deposition. c) Lift-off removes the resist and any metal not in contact with the substrate.

(crowning) which form fractures in overlaying lithography steps. The fabrication of both the inner and outer contacts were performed through this method.

Optical Lithography

The outer contacts include feature dimensions of the order 1–100 µm—far too time consuming to expose through electron beam lithography. Optical lithography utilises a predefined mask, usually etched into Cr on quartz, which defines the exposure pattern. The OL was performed on and EVG 610 with a deep ultra-violet (DUV) 350 W lamp in the wavelength range 350–450 nm. The clean substrates were spin coated with Microchem Lift Off Resist (LOR) 3A at 4000 rpm for 40 s and baked on a hot plate at 200°C for 5 min. Then the photoresist S1813 was spin coated at 4000 rpm for 40 s and baked on a hot plate at 110°C for 3 min. The upper layer is photosensitive and will define the feature dimensions once exposed, the LOR does not actually require exposure and will simply dissolve in the resist developer, allowing the control of the undercut by varying the developer time. The sample was exposed for 3.2 s, developed in MF 319 for 2 min and rinsed in de-ionised water (DI H_2O). Once the material has been deposited the sample was placed in a lift off solution of MICROPOSIT Remover 1165 at 75°C and, when the lift-off was completed, thoroughly rinsed in DI H_2O to remove any unctuous residues.

Electron-beam Lithography

Electron-beam lithography's main advantages over optical lithography are the drastic increase in resolution and ability to easily alter the design. However, these advantages come with the caveat of electron beam lithography's reduced sample throughput. For these reasons EBL is used for the inner contacts, where dimensions ~100 nm are required and designs can vary depending on the device requirements. The data preparation, proximity error correction and EBL were all performed by Dr. M. Rosamond through the BEAMER software and on a Jeol JBX 6300FS system. Similar to the OL recipe, a bilayer resist structure was again used to produce a natural undercut and good lift-off. The support layer is methyl methacrylate (MMA) EL11 spin coated at 4000 rpm for 40 s and baked on a hot plate at 180°C for 5 min. This is followed by polymethyl methacrylate (PMMA) 950k A4 again spin coated at 4000 rpm for 40 s and baked at 180°C for 5 min. Figure 3.4 shows the contrast curves for these two resists, clearly showing the difference in sensitivity which provides the undercut, as the MMA will is overexposed for any dose required to fully expose the PMMA. The sample was exposed on the JEOL system, with a beam current of 10 nA and dose of 440 μC/cm^2. The development was performed in a DI H_2O/IPA (3/7 by vol.) mix at 20–21°C for 3 mins followed by a rinse in DI H_2O. Prior to the deposition the samples undergo an oxygen plasma ash for 20 s at 50 W to remove any resist residues. The lift-off was carried in warm (40–50°C)

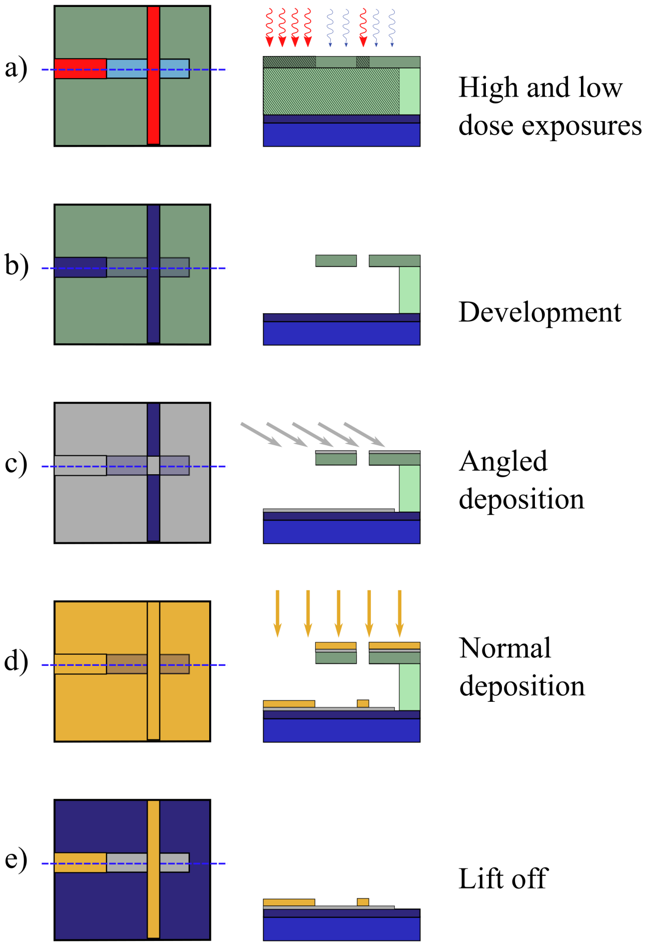

Figure 3.3: Overview of shadow lithography process. a) Two resists are used, the bottom layer having a higher sensitivity. The resists are exposed through a double dose technique discussed in the main text. b) Development causes regions of the low sensitivity upper layer to remain forming resist bridges. c) Material is deposited at an angle to the substrate causing lateral shifts in patterned features. d) Deposition normal the the surface completes the device forming electrical contacts. e) Lift off removes the resist.

acetone followed by a rinse in IPA.

3.2.2 Shadow Lithography

Key to this work was the development of a robust double-dose shadow lithography technique with Dr. M. Rosamond[60], which combined with the new angle deposition chamber allows the fabrication of lateral structures with high quality ohmic contacts. An outline of the process is shown in Fig. 3.3. This step utilises EBL and as such the same resist recipe as above. However, the bake times here were increased to 10 mins for each layer to ensure all the solvent is driven out of the resist and the structure is rigid once developed. This is important for the regions of PMMA with no support resist post development. As seen in Fig. 3.4 the dose required to clear the MMA is ≈120–130 μC/cm^2 which will only slightly thin the upper PMMA layer. This allows the two layers to be exposed independently of each other by varying the dose in different regions of the pattern. Fig 3.3 (a) shows the high (red) and low (blue) exposure regions where the high dose exposes both layers while the low dose will only affect the MMA. The design is exposed on the JEOL system with a 500 pA beam current and a base high dose of 440 μC/cm^2. The low dose is then calculated depending on the proximity of the each region to a high dose section and will vary from 120 μC/cm^2 for section close to a high dose area to 150 μC/cm^2 for areas further away. The details of this proximity correction

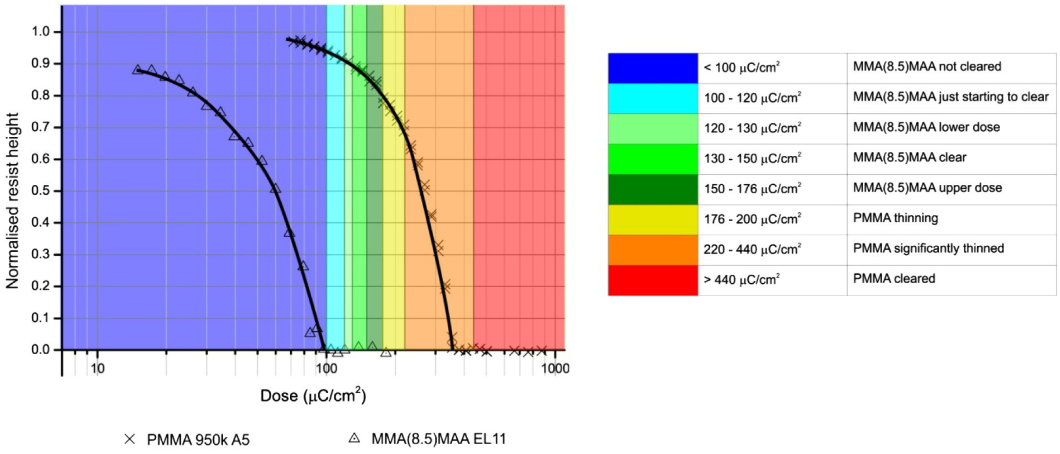

🟦	< 100 μC/cm^2	MMA(8.5)MAA not cleared
🟦	100 - 120 μC/cm^2	MMA(8.5)MAA just starting to clear
🟩	120 - 130 μC/cm^2	MMA(8.5)MAA lower dose
🟩	130 - 150 μC/cm^2	MMA(8.5)MAA clear
🟩	150 - 176 μC/cm^2	MMA(8.5)MAA upper dose
🟨	176 - 200 μC/cm^2	PMMA thinning
🟧	220 - 440 μC/cm^2	PMMA significantly thinned
🟥	> 440 μC/cm^2	PMMA cleared

Figure 3.4: Contrast curves for PMMA and MMA resists. The dose required to clear PMMA is 440 μC/cm^2 while MMA required only 120 μC/cm^2. At 120 μC/cm^2 the PMMA starts to thin but a substantial amount of resist remain. Data obtained by Dr. M. Rosamond[60].

can be found in reference[60].

The samples were then developed in a DI H_2O/IPA (3/7 by vol.) mix at 20–21°C for 3-3.5 mins and rinsed in DI water. Since the development of the MMA bottom layer is a diffusion limited process, in order to obtain reliable results a development test structure was patterned with every device. An example of this is shown in Fig. 3.5 where the suspended resist regions can be seen. This aids the development process where the actual device structures are too small to view in an optical microscope. Post development the samples underwent an RF Ar ion mill for 15 s, with 10 sccm Ar at 50 W to remove any resist residues before the final deposition. The liftoff was performed in warm acetone, where once the majority of material has come away the samples were transferred to fresh acetone and left overnight. This aims to remove the resist of the side wall of the pattern which can become cross linked due to stray ions from the evaporation source. Finally the samples were rinsed in IPA.

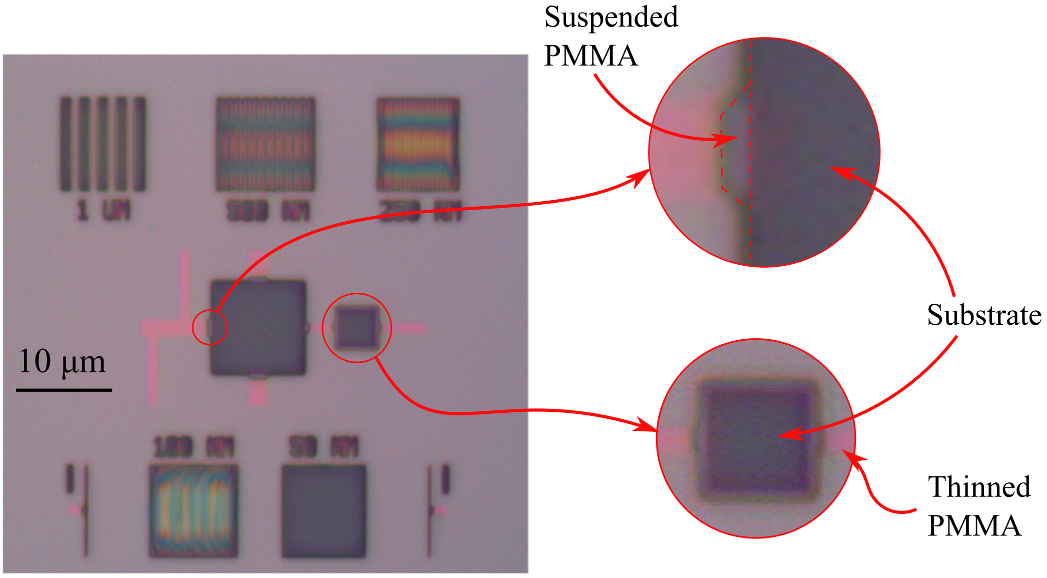

Figure 3.5: Optical image of the structure used to gauge the development times. Highlighted areas show the suspended PMMA and thinned parts where a low dose was used.

3.2.3 Material Deposition

Three different techniques have been used to deposit material while fabricating devices. Sputter deposition was used for the outer contacts, while conventional electron-beam evaporation was used for the inner contacts. Finally the central devices utilise shadow deposition with a combination of electron-beam and thermal evaporation.

Sputter Deposition

Sputter deposition is a widely used technique for both coating substrates and thin film growth. It has many advantages over other techniques, from quick and simple coating of surfaces to aid imaging in electron microscopy to the high energy of the adatoms allowing good mobility on the substrate and producing high quality films.

Sputtering requires the presence of a working gas, usually Ar. The inert gas is bled into the system at a pressure of the order of ~1 mTorr and converted into a plasma through the application of large (~500 V) potential. The heavy Ar ions are then accelerated towards the negatively biased target material and through momentum transfer knock out atoms of the source material. The source material then condenses on the substrate forming a thin film. Due to the working gas involved in sputtering the atoms in the deposition flux have very short mean free paths, order 10^{-2} m. This creates an almost conformal deposition atop any patterned structure on the surface of the substrate which can be beneficial when depositing overlaying lithography. However, to achieve successful lift-off an undercut is generally required to ensure the deposited material is not continuous at the junction between the substrate and the wall of the resist.

Electron-beam Evaporation

A schematic of an electron-beam deposition gun (e-gun) is shown in Fig. 3.6 (a). A large current (~10 A) is driven through a tungsten filament producing thermionic emission of electrons. These electrons are then accelerated through a potential ~7 kV providing a large amount of kinetic energy to the electron flux. Through the use of electromagnets (or a permanent magnet as in Fig. 3.6) the beam of electrons can be deflected to impinge on the source material causing it to heat up. The source material sits within a water cooled Cu hearth, and some times placed in a crucible of a suitable material. The water cooling produces a temperature gradient such that the outer of the source remains solid but a small region in the centre will melt and evaporate. The great advantage to electron-beam evaporation is it does not require any working gas in the system and as such the evaporation can take place under UHV conditions. This means the evaporated flux can have a mean free path greater than the dimensions of the chamber and can be considered to originate from a point source. As a result, when evaporating into lithography very well defined features are achieved. Unfortunately back scattered electrons from the source along with ionised atoms can damage the resist by causing cross linking of the polymer chains preventing successful liftoff. This can be avoided through he careful placement of permanent magnets along the path of the evaporated flux to deflect charged particles.

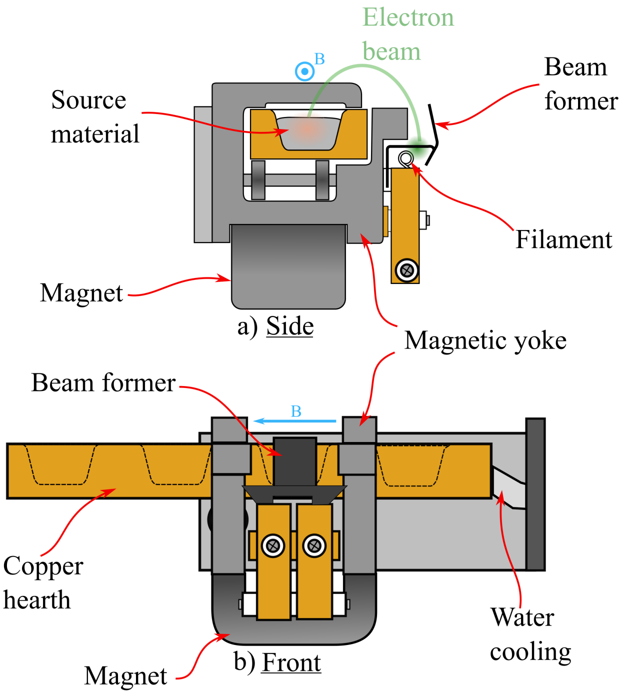

Figure 3.6: Schematic of the e-gun within the shadow deposition system. The magnet and yoke provide magnetic flux to curve the accelerated electrons, which then impinge on the source material. There are four source pockets within the water cooled hearth mounted on bellows and able to slide past the filament assembly.

Angled Deposition

In order to perform electron-beam deposition at various angles relative to the sample plane a bespoke UHV deposition system was set up as part of this work. The original system was designed by Dr. G. Burnell and Dr. M. Ali and has since undergone many additions. A considerable amount of help has been received during the design and implementation of additional features by Dr. J. Witt, Dr. M. Ali, Dr. G. Burnell and Prof. B. Hickey along with the

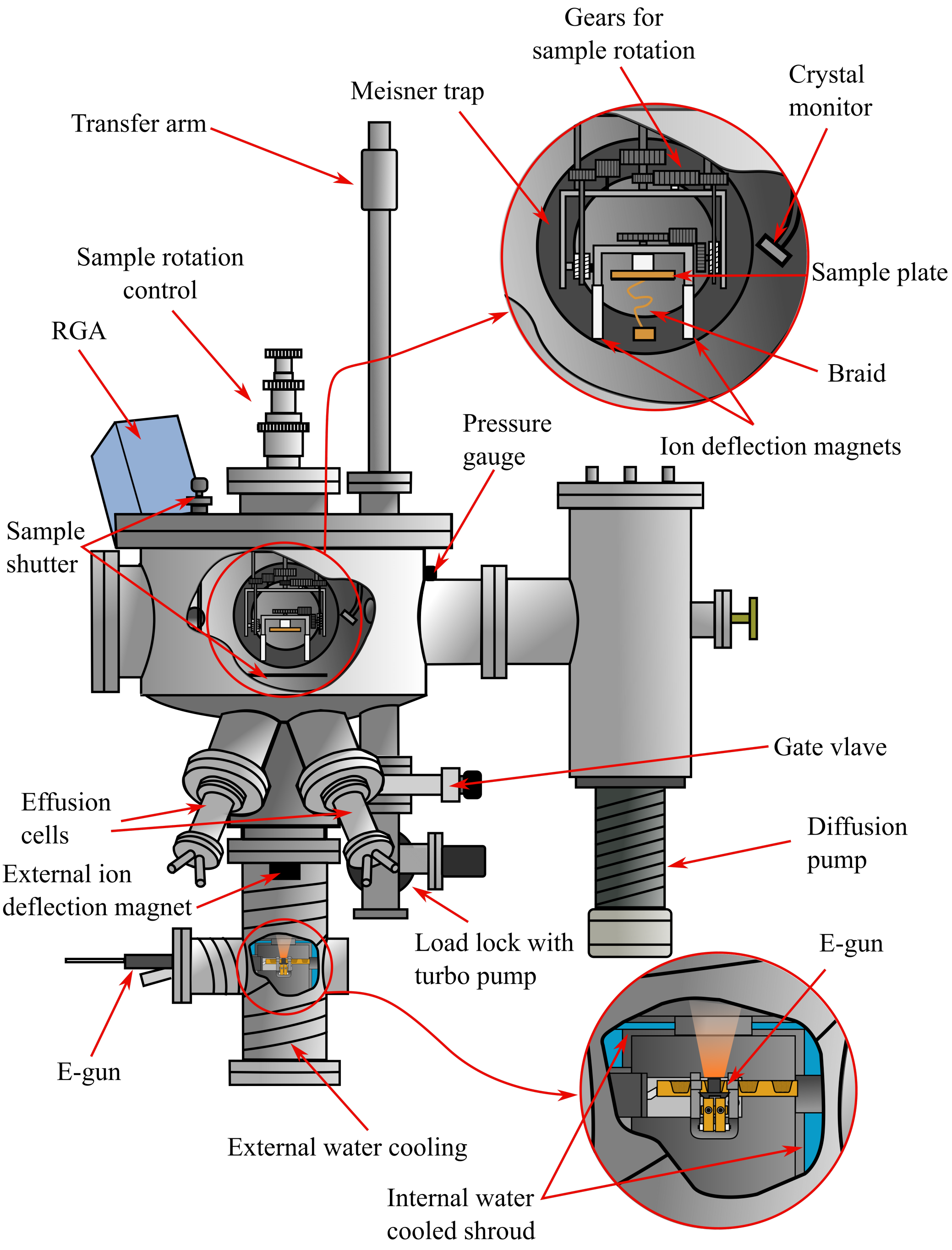

Figure 3.7: Bespoke UHV system for angle deposition. Two effusion cells are used for nonmagnetic materials and a four pocket e-gun (see Fig. 3.6) for magnetic materials. A gear assembly allows three degrees of rotation of the sample. The system has a large diffusion pump and Meissner trap, along with a turbo pumped load-lock.

technical staff in the School of Physics and Astronomy. The result has lead to the chamber shown in Fig. 3.7.

A critical requirement of such a chamber is an extremely good base pressure. This lowers the residual gasses in the system which will in-turn improve the quality of the deposited material, especially in evaporation systems where the distance between the source and substrate can be quite large, generally ranging from ~0.1–1 m. The main chamber is pumped by a large diffusion pump fitted with an oil trap. This is a large internal space that can be filled with liquid N_2 causing any oil which may be drawn into the deposition chamber to condense and remain in the diffusion pump, it is also effective at condensing water removing it from the vacuum. The system is fitted with a load lock, separated from the main chamber by a gate valve, so samples may be loaded without venting the entire system. Samples are placed in a carousel in the load-lock, which can be evacuated to 5×10^{-8} mbar via a turbomolecular pump, then loaded into the main chamber using a linear transfer arm. A sample can then be moved onto the sample plate via a wobble stick. There is a second cold trap within the main chamber along with a titanium sublimation pump (TSP). The combination of the load-lock and various pumps enables an ultimate base pressure of the system of the order of 10^{-10} mbar. The total pressure is monitored through an ion gauge while partial pressure are acquired through a residual gas analyser (RGA).

Since the system is aimed at the fabrication of nanoscale lateral structures, evaporation sources have been chosen for the material deposition. In combination with UHV, evaporation sources act as a point source and so provide clean shadowing of the resist design on a substrate. The system has an e-gun similar to that in Fig. 3.6, with four source material pockets for FM material and two thermal evaporation effusion cells for NM materials. The evaporation rates are monitored by a quartz crystal which is calibrated through growth of thin films and x-ray diffraction to obtain their thickness. In general, the evaporation rates for the magnetic materials are ~0.1–0.2 Å, while nonmagnetic material ~0.3-0.4 Å. A shutter is then used to ensure the correct amount of material is deposited.

The use of evaporation sources in conjunction with lithography brings with it issues that required changes to the initial design of the system. The two detrimental effects were the generation of large amounts of thermal radiation from the sources and high energy charge particles from the e-gun, the consequences of which are shown in Fig. 3.8. The polymers used in the resists will begin to reflow at temperatures > 100°C, causing a loss of definition of the pattern and can lead to poor lift-off. Figure 3.8 (a) is an SEM image of a sample

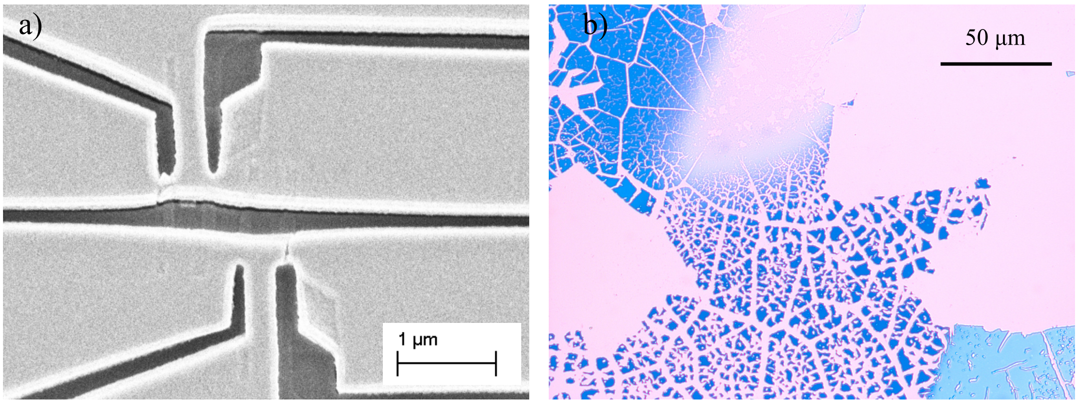

Figure 3.8: a) SEM post deposition and before lift-off of a LSV. Widening of the patterns has occurred due the upper resist layer becoming hot and reflowing. b) Optical image of a sample after attempted lift-off. Charge particles damage the resist, cross-linking polymer chains, preventing it from dissolving in the lift-off solution.

where the thermal radiation from the evaporation sources has caused the upper layer of resit to warp, destroying the lithography. To avoid this two modifications were made to the original chamber. Firstly all the working distances (WD) between the source and sample were extended. For the e-gun the original WD, specified by the manufactures, was 25 cm and was expended through an additional section to 60 cm. Similarly, the effusion cells original WD were 15 cm and were extended to 27.5 cm. The second set of modifications was the introduction of cooling systems, one for the sample plate and another surrounding the e-gun. For this, the sample plate was thermally isolated from the gear system through a set of ceramic washers. It was then anchored to the Meissner trap in the main chamber so that when filled with liquid N_2 would act to cool the sample plate. A large water cooling system was also introduced, surrounding the e-gun which produces a large amount of heat due to the higher melting points of the magnetic materials in comparison the Cu and Ag. Figure 3.8 (b) is an optical image, after attempting lift-off, showing sample damage due to implantation of charged particles. These are a combination of back scattered electrons and ionised evaporated flux from the e-gun, which cause cross-linking of the resist preventing it from dissolving in the lift-off solution. To avoid this magnets have been placed between the evaporation source and the sample which deflect the ions, allowing good lift-off.

The sample manipulator involves a system of gears linked to a rotation control outside the system via magnetic coupling. This allows the tilting and rotation of the sample with respect to the evaporation sources and is the key aspect that distinguished this system. Since the deposition is performed in a UHV environment the evaporated material has an extremely long mean free path (greater than the chamber size) and when combined with the correct lithography can be used to create well defined shadowing as show in Fig. 3.3 (c) and (d). The development of this deposition chamber in conjunction with the double-dose lithography has allowed the fabrication of lateral device with high quality interfaces. These are the first samples fabricated though this method at the University of Leeds.

3.3 Device Characterisation

This thesis focuses on the properties of spin transport in LSVs, hence the main characterisation techniques involve magnetotransport measurements from room temperature to liquid helium. The signals from such devices can be quite small, requiring measurement apparatus with a good noise levels. LSVs are also highly delicate as they are fabricated from conductive metals and so are easily destroyed by static shocks. In order to measure these devices a custom designed measurement stick and sample head were made to go in the available cryostat.

3.3.1 Measurement Stick and Sample Holder

The principles behind the design of the measurement stick were aimed at reducing noise, spurious measurement effects and the possibility of unwanted voltage spikes from switches or cable movement that can destroy samples. This involved separating the noisy thermometry lines from those carrying the signals, reducing the number of solder connections, fixing the breakout box atop the stick, and ensuring the signal lines are twisted pairs and non-inductively wound where required. Much of the design follows from guidance obtained from reference [61].

A schematic of the final stick is shown in Fig. 3.9. The main stick consists of an outer and inner tube shown in the highlighted section. The 20 signal lines are twisted pair Cu loom, which is wrapped non-inductively around the inner tube and heat sunk with GE varnish. The thermometry lines are then isolated, as they run through the centre of the inner tube, and exit the stick separately through a 4-pin LEMO connector away from the main breakout box. The signal lines each go to a BNC connector at the top of the stick where the outer of all BNCs are electrically connected to the box. During the measurement the whole stick

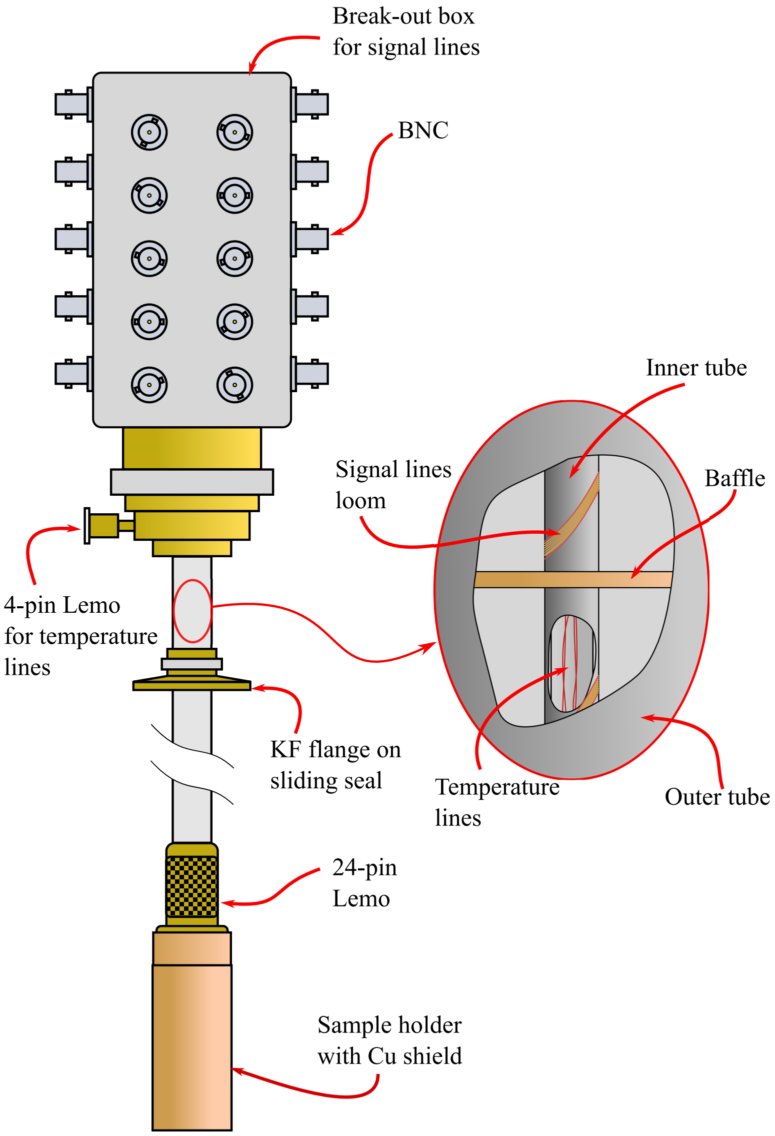

Figure 3.9: Stick used for electrical characterisation of devices in a He flow cryostat.

is isolated from the cryostat through a rubber o-ring at the KF seal and the box connected to the measurement ground. This forms a completely coaxial circuit surrounding the measurement. In order to connect or swap cables a T-piece and BNC terminator is used, shorting the signal line to the outer of the BNC. Thus any spurious voltages from mechanically making and breaking connections with the BNC cables preferentially go to ground, rather than through the signal lines.

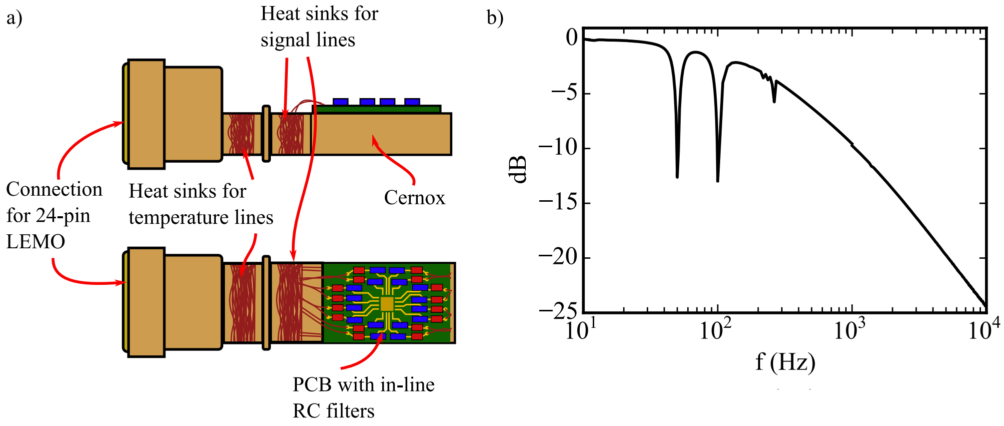

Figure 3.10: a) Schematic of custom made sample head. Each signal line has an RC filter to reduce noise and prevent static shocks reaching the device. Values of the components are R = 1 kΩ and C = 220 nF. b) Filter characteristics at room temperature. The cut off frequency is 220 Hz. The two troughs visible at 50 and 100 Hz are the band pass filters in the lock-in and not a characteristic of the sample head.

The design of the sample head is shown in Fig. 3.10 (a). The main body is made from Cu to be thermally conductive and reduce temperature gradients. The signal lines and thermometry are independently heat sunk to the Cu reducing the heat leak to the sample and a calibrated Cernox is fixed behind the sample position. The most important aspect of the sample head is the inclusion of a printed circuit board (PCB) which introduced resistor-capacitor (RC) filters into each signal line. These act as a low-pass filter and have a measured cut-off frequency of 220 Hz - see Fig. 3.10 (b). These reduce the noise from high frequencies and also act to filter out any static shocks which may destroy the sample. The two troughs visible at 50 and 100 Hz are the band pass filters in the lock-in and not a characteristic of the sample head. The combination of the above stick and sample holder allow measurements with a typical noise level of $\sim$ 10 nV/$\sqrt{\text{Hz}}$.

3.3.2 He Flow Cryostat

All magnetotransport measurements have been performed in an Oxford instruments He flow cryostat shown schematically in Fig. 3.11. The system consists of a variable temperature insert (VTI) placed in a He reservoir. This is then surrounded by a Nitrogen tank with a vacuum space between. In the He reservoir, surrounding the bottom of the VTI, is a superconducting solenoid capable of producing up to 8 T fields. The sample sits on the sample

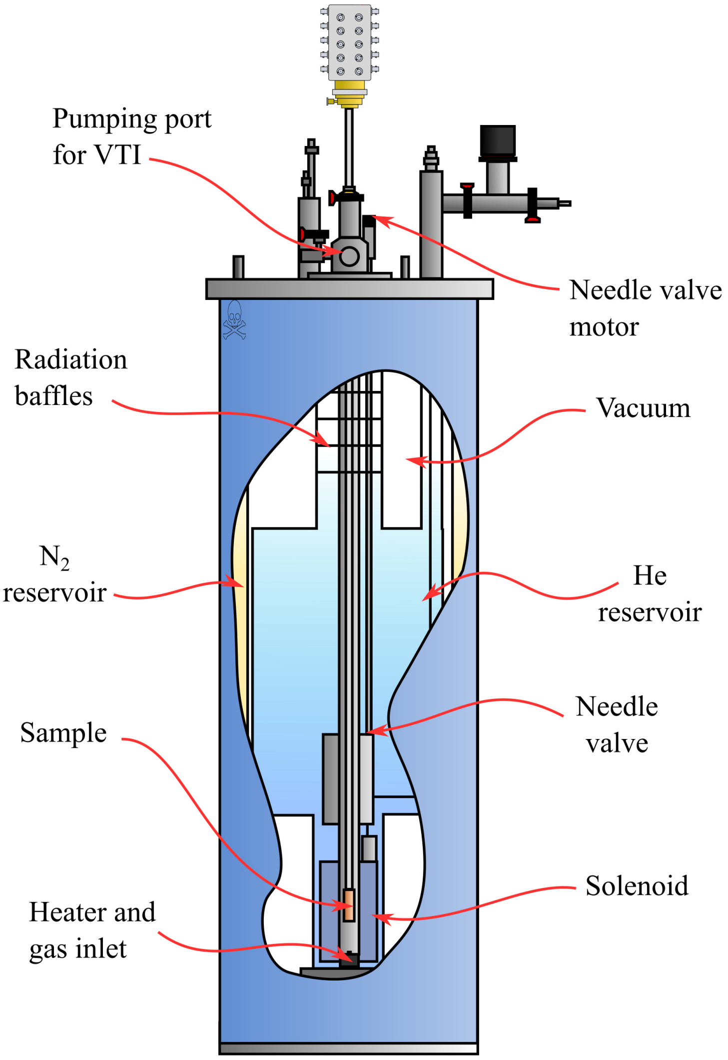

Figure 3.11: Schematic of a He flow cryostat used for magnetotransport measurements.

head at the end of the measurement stick described above, which is then lowered into the VTI such that the sample is in the centre of the coil. The VTI is evacuated with a roughing pump and He gas flows through a heater to control the temperature between 300 and 1.4 K.

The electrical measurements are performed with a Keithley 6221 current source and 2182A nano-voltmeter in a conventional 4-probe technique. These, along with the temperature and magnetic fields, are all controlled using software written in LabVIEW by Dr. G. Burnell. The communication between the equipment and PC is through a GPIB to USB adapter.

3.3.3 MOKE

The magneto optical Kerr effect causes a change in amplitude and rotation of the polarisation of linearly polarised light upon reflection from a magnetic material. The rotation experienced by the light is proportional to the magnetisation of the sample and can be detected by a polariser-analyser pair. It has been used to investigate the switching behaviour of magnetic electrodes designed for LSVs. The transverse orientation was used where the magnetisation lies in the plane of the sample and parallel to the plane of incidence, leading to elliptically reflected light with a Kerr rotation. This effect however is dependent on the angle of incidence and will produce no rotation if the radiation is incident normal to the sample. By measuring the magnitude of the Kerr rotation as a function of applied field information is gained about the reversal field of patterned samples.

3.4 Data Analysis

Throughout this work the data analysis was performed through scripts written in Python, a freely available language. As discussed in the following chapters many individual current-voltage curves are obtained for various different control parameters and the individual fitting of each is a task well suited to a Python script. Many of the functions used are part of the Python module developed by Dr. G Burnell and other members of the Condensed Matter group at Leeds, including the author[62].

CHAPTER 4

Characterising Lateral Spin Valves

4.1 Introduction

The fabrication of high quality LSVs is central to work presented in this thesis, and as such, a significant amount of effort was expended in optimising lithography recipes, along with the commissioning of a new deposition chamber. Through these means LSVs with transparent interfaces are achieved, and this chapter will present the measurements used to obtain the interface resistance, $\mathrm{R_i}$, along with some design considerations for LSVs. A good understanding of the interface resistance is needed as it strongly affects the physics of spin transport[28, 47, 63] and as such the models used to interpret the data. Similarly, well engineered LSVs allow precise control of the FM electrodes state, leading to unambiguous determination of the spin dependent transport properties. Here the design considerations and simulations used to ensure suitable reversal of the FM electrodes will be presented. This chapter will also discuss the different contributions to the nonlocal signal due to spin, charge and thermal transport. Since the overall focus of the thesis is spin transport, it is crucial to be able to distinguish between these different effects. This was achieved through investigating the dependence of the nonlocal voltage on injection current, field and temperature.

4.2 Interface Resistance

In LSVs the properties of the interface dictates the occurrence of spin flip events upon spin injection, which will alter the magnitude of the spin accumulation. R_i is also a crucial parameter in determining the amount of spin absorption at a FM/NM interface[46, 47]. This can alter the profile of the spin current within the NM and is important when fitting data to obtain spin transport parameters[28]. Two different methods have been used to quantify R_i for samples fabricated in this study.

4.2.1 Kelvin Resistors

Kelvin resistors (KRs) are specifically designed to measure the contact resistance of two materials. Figure 4.1 (a) is a schematic of an ideal KR. This structure involves two elbow shaped wires that overlap at their vertices to form a cross with a contact area A. When a current is driven along the vertical electrodes it travels in a straight path, then using the horizontal leads to probe the potential, the measurement should only be sensitive to the voltage drop at the interface between the two materials. The benefit of a KR geometry is that the current

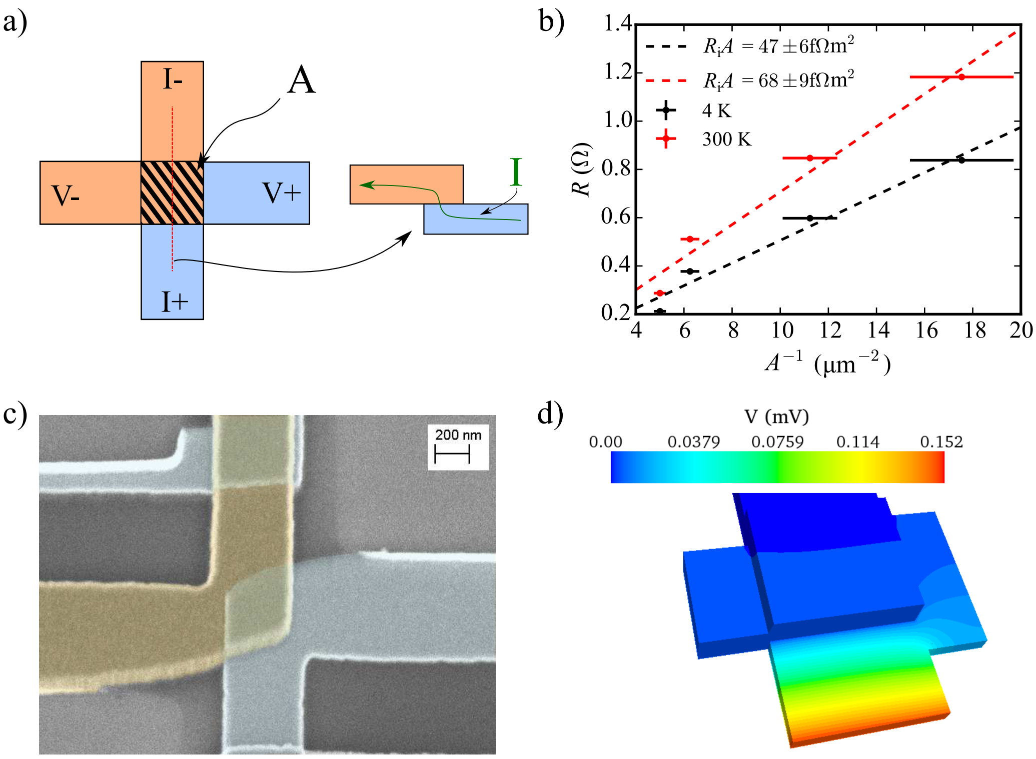

Figure 4.1: a) Schematic illustrating the ideal Kelvin resistor geometry. Red line indicates section showing ideal current path. b) Plot of resistance as a function of inverse interface area A at 4 and 300 K. A was obtained from SEM data. Linear fits show the R_iA product. c) SEM image of a Kelvin resistor. False colour indicates the Py (blue) and Cu (orange). The misalignment of the overlap due to small shifts in the deposition angle can clearly be seen. d) Finite element simulation of the voltage in a KR. Shows the nonuniform equipotentials within the voltage leads due to the non-ideal geometry.

flow is always perpendicular to the voltage leads, which will in principle remove spurious effects due to the current flow around a corner[64]. However, it is important to note that even KRs will experience current bunching if the difference in conductivities of the two materials is large, causing a reduction in the effective junction area.

A series of KRs of different A were fabricated, as R_i should be inversely proportional to A, to obtain the resistance area product R_iA. The data for R_i as a function of A^{-1} is shown in Fig. 4.1 (b) for temperatures of 4 and 300 K. The linear fits to the data give resistance area products at 4 and 300 K of 47 ± 6 fΩm^2 and 68 ± 9 fΩm^2 respectively. These values far exceed those expected for transparent Py/Cu interfaces from theory[65] and experiment[11, 13, 66] by around a factor of 100, but is actually a result of the device geometry and not inherent to the interface. The KRs are fabricated through a double angle deposition technique. The Py is first deposited at 45° to the sample normal, the substrate is then rotated to -45° and the Cu deposited. Due to the rotation between the two depositions, the two layers are susceptible to a misalignment error. In Fig. 4.1 (c) it can be seen that the Cu and Py do not completely overlap in the corner. This misalignment of the two depositions causes a region where current spreading can occur, causing spurious voltages in the sense electrodes. To estimate the magnitude of this contribution finite element analysis has been used. Figure 4.1 (d) shows the result of simulating the potential throughout a KR. The misalignment of the lithography causes current spreading into the voltage leads, generating a potential gradient which is not due to the contact resistance between the two materials. The amount of current spreading, and as such the distribution of voltage within the leads, is strongly contingent on the misalignment. Depending on the exact geometry, and position of the voltage leads, this nonuniform current distribution can account for the entire measured signal explaining the apparent large interface resistance. Hence, another method is required to obtain a more accurate estimate of the interface resistance.

4.2.2 Cross Geometry

As the design of the KRs was shown to be unreliable due to the high sensitivity to any misalignment during the lithography, a more simplistic cross geometry is used to measure R_i. Figure 4.2 (a) is an SEM image of a typical cross used for this. This type of device is essentially one half of a LSV and easily fabricated simultaneously with a set of LSVs. However, in these measurements the current path is not linear as it has to go around a corner from the source to the drain. This again causes a geometrical voltage due to inhomogeneous current distribution and the resulting shape of the equipotentials[64]. Figure 4.2 (b) shows the measured R_i (black) as a function of temperature. This signal is negative and increases in magnitude with temperature. The results of the finite element analysis can be seen in Fig. 4.2 (c) and (d) where the simulated potential is shown. It is clear that due to the low resistivity of the Cu above the Py there is a significant amount of current leakage along the Cu voltage lead. This causes the V- lead to be at a higher potential with respect to V+, forming the appearance of a negative R_i. Figure 4.2 (d) shows a reduced scale highlighting where the V- lead is at a higher potential to the V+ lead. The results of the simulation as a function of temperature are also shown in Fig. 4.2 (b) and the magnitude of the geometric signal is very similar to the measured resistance at all temperatures. As the simulation geometry is an ideal case it may underestimate the geometric signal, but it can account for the negative voltage and indicates that the interface resistance is very low. Taking the positive difference between the measured signal and the simulation an order of magnitude estimate for $R_\mathrm{i}A \approx 0.1$ fΩm^2 is obtained and comparable to values elsewhere for both lateral and conventional spin valves in the transparent limit[11, 13, 19, 64]. This is evidence that the fabrication process used throughout this work is able to produce good quality, low resistance ohmic contacts.

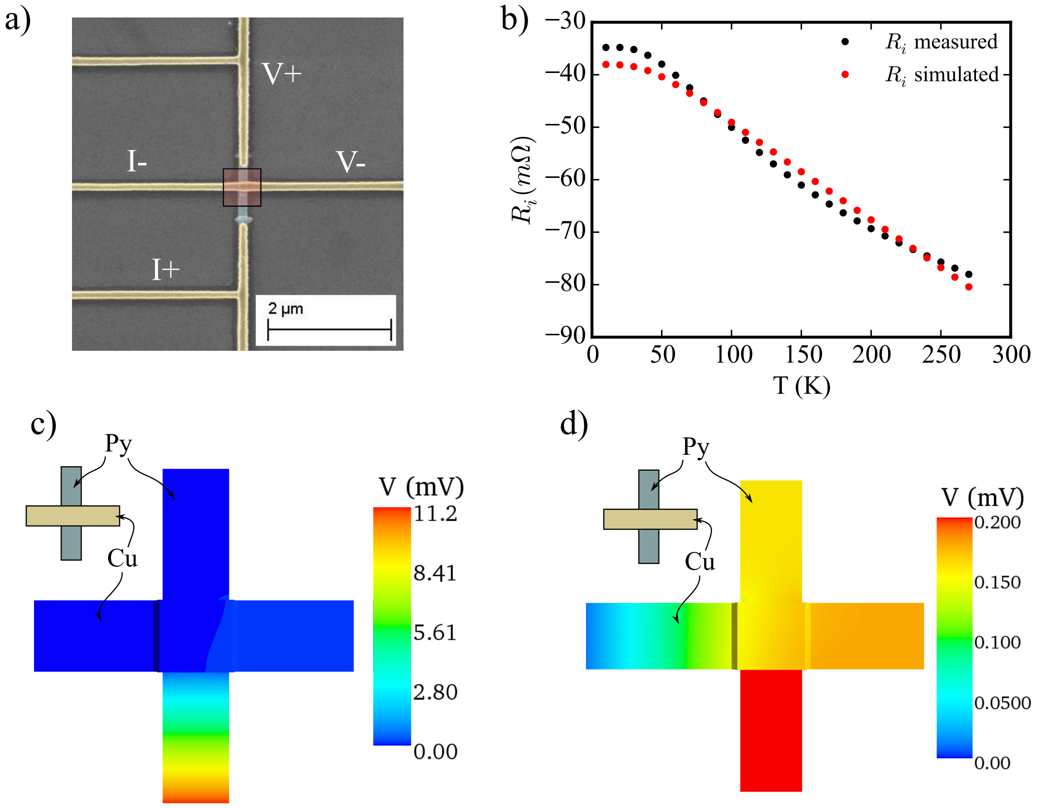

Figure 4.2: a) SEM of device used to measure the interface resistance in the cross geometry. False colour indicating the Cu (orange) and Py (blue). Central highlighted region represents the simulated region shown in c) and d). b) Measured interface resistance as a function of temperature (Black). The resistance is negative due to the geometric current spreading. This is highlighted by the red data from the simulations. c) Finite element simulation of cross device showing the calculated voltage. Full scale of the voltage shows the largest potential drop is within the Py due to its higher resistance d) Reduced voltage scale highlighting the potential difference of the voltage leads. The carrot colour of the V- lead indicates a higher potential than the yellow of the V+ lead.

4.3 Lateral Spin Valve Design

Lateral spin valves rely on FM electrodes to create and detect the pure spin current in the NM spacer. The quantisation axis of the injected spin accumulation is dictated by the direction of the magnetisation of the injection FM[67]. Similarly, the detection of the spin current is proportional to its projection onto the magnetisation of the second FM electrode. To maximise the measured signal, and obtain the most reliable estimate of the magnitude of the spin current, a well defined antiparallel (AP) configuration of the two FMs is required.

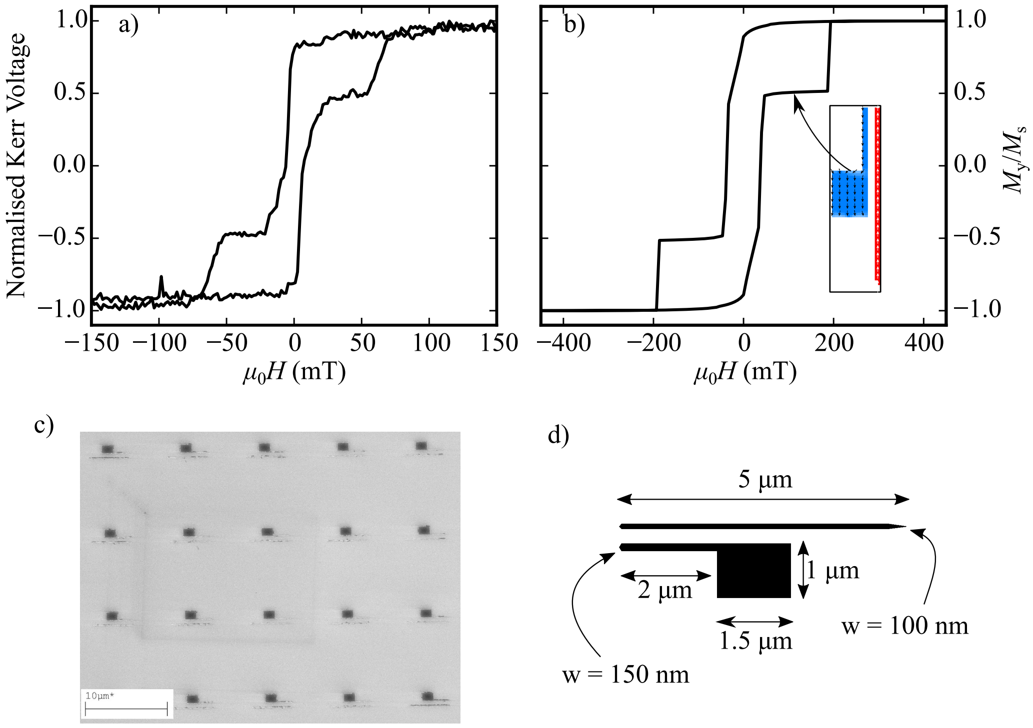

Figure 4.3: a) MOKE data of a 40 000 array of Py electrodes. b) OOMMF simulation of a single pair of Py electrodes. Inset shows the electrodes in the AP state with colour coded magnetisation, Blue is positive y direction and red negative. c) SEM image of array of Py electrodes showing the 10 µm separation. d) Schematic of electrodes used.

The chosen electrode design is shown in Fig. 4.3 (d). They consist of a high coercivity long and narrow wire with pointed ends and a second lower coercivity electrode with a wider wire accompanied by a large nucleation pad. The pointed ends prevent the formation of closure domains which can reduce the required fields to reverse the magnetisation. The closure domains may also cause a region of non-uniform magnetisation in the injection region, reducing the effective spin polarisation and hence spin accumulation. As a result of shape anisotropy, the demagnetising field along the direction of the applied field is larger in the pad causing it to reverse at a lower field value. This nucleates a domain wall at the base of the attached wire which can propagate along its length once over coming the relatively small pinning potential. To check these electrode designs function as required simulations were first performed using the OOMMF micromagnetics software. The results of the simulation are shown in Fig. 4.3 (b), where the normalised magnetisation in the y-direction is plotted as a function of external field along the same axis. As the field is reduced from positive saturation and crosses through zero, there is a gradual reduction in M_y as the nucleation pad begins to rotate its magnetisation, the injection of a wall along the length of the attached wire is then marked by a sudden decrease in M_y. This is followed by a flat region where the two electrodes have AP moments, until around 200 mT, when another reduction in M_y indicates the reversal of the narrow wire. This demonstrates that the reversal fields for these two electrodes should be sufficiently separate and that a clear AP state is obtained.

The reversal of FM wires through domain wall motion can be stochastic and will vary with temperature, as thermal activation energy can help to overcome the pinning barriers. Since OOMMF simulates an idealised system at zero Kelvin an array of 40 000 electrodes was patterned through a standard EBL lift-off technique to measure the switching fields at room temperature. The electrodes were patterned 10 μm apart from each other to prevent interactions and provided a 2 × 2 mm area which can easily be focused on with the MOKE laser spot. The data from the MOKE measurements on 20 nm thick Py is shown in Fig. 4.3 (a). The data shows a qualitative similarity with the OOMMF simulations with two distinct switching events corresponding to each electrode, however the coercive fields are much smaller by a factor of 3. This is a joint consequence of the experiment having been performed at room temperature and that the real sample will contain defects that will act as nucleation points aiding the reversal the magnetisation. Of key importance here is that there is still a clear AP state and thus this design is suitable for use in LSVs.

4.4 Nonlocal Characteristics

Lateral spin valves allow the separation of charge and spin currents, proving to be ideal device structures for the investigation of spin transport phenomena through nonlocal measurements. However, experiments have shown that nonlocal signals can include spurious effects unrelated to spin transport[13, 68, 69]. Thus detailed knowledge of the nonlocal voltages caused by charge and thermal transport within LSVs is required to guarantee the correct interpretation of spin transport signals. In order to separate each contribution, the dependence of the nonlocal signal on injection current, applied field and temperature has been investigated.

4.4.1 Nonlocal IV

The nonlocal current-voltage characteristics (NLIV) are a powerful tool in observing different transport mechanisms within LSVs. In most studies conventional AC lock-in techniques are used[9, 11, 12, 68], however these obscure any dependence the nonlocal signal may have on the direction of the current flow[13]. Throughout this work a DC spin injection method has been used with the current and voltage leads connected as shown in Fig 4.4 (a). The nonlocal voltage is then measured while sweeping the injection current, providing extra information about the current dependence as similarly done by Kasai *et al*[70]. Figure 4.4 (b) shows a typical NLIV in both the P and AP states. The measured nonlocal voltage should represent the spin signal and as such is expected to be linear in current and reverses its sign with the current[7, 28]. This is not the case here, as the voltage remains positive and independent of the current direction, while also being non-linear. Based on a-priori assumptions that the spin-voltage is linear in current whilst thermal and other parasitic effects depend on the

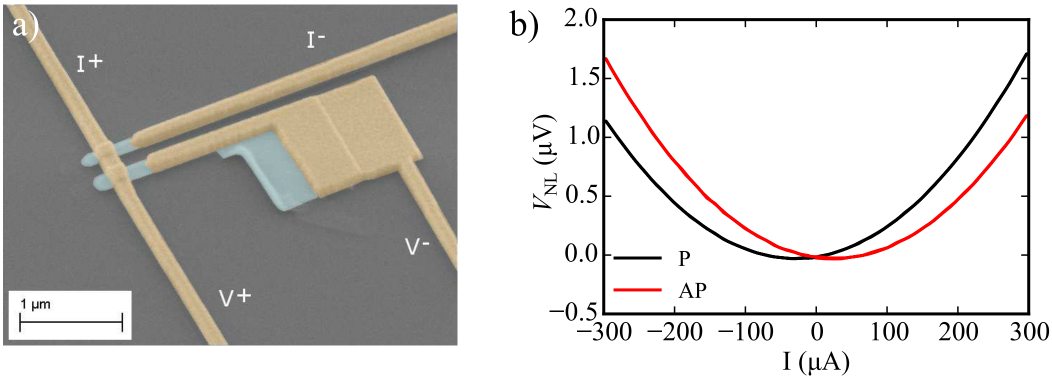

Figure 4.4: a) SEM image of a LSV device. False colour has been added to highlight the Cu (orange) and Py (blue). The FM electrode separation is 200 nm. b) Nonlocal IV at 30 K of a LSV in the parallel (P) and antiparallel (AP) state. The separation of FM electrodes $L = 425$ nm.

power dissipated within the device, a 2$^{\mathrm{nd}}$ order polynomial was chosen to fit to the IV of the form:

$$V_{\mathrm{NL}} = V_\beta + V_\mathrm{s} + const. = \beta I^2 + R_\mathrm{s} I + const. \tag{4.1}$$

The constant term accounts for voltage offsets within the experimental apparatus, most likely a result of thermal emfs and can be subtracted. Here it has been assumed that the gradient in the linear component of the nonlocal voltage is the nonlocal spin resistance R_s. This is a formalism that has been adopted throughout the literature where the nonlocal voltage normalised by the injection current produces an effective resistance. Figures 4.5 (a) & (b) show the results of extracting each component from the raw NLIV data. The V_β term is obtained from the subtraction of the linear coefficient from the NLIV, producing a voltage signal that varies quadratically with the injection current. It is immediately apparent that there is no correlation with the magnetic state of the LSV, as both P and AP configurations produce the same curve. The absence of a dependence on the LSVs magnetic state indicates V_β is not a spin dependent signal. At the current densities used (max ~ 10^{12} A/m^2) and in conjunction with the I^2 behaviour it is assumed that this is a thermal effect caused by Joule heating at the injector. This is further supported by this coefficient demonstrating a dependence on the thermal properties of the substrate[70] and is discussed in more detail in the following section.

The consequence of subtracting the quadratic coefficient from the NLIV data is presen-

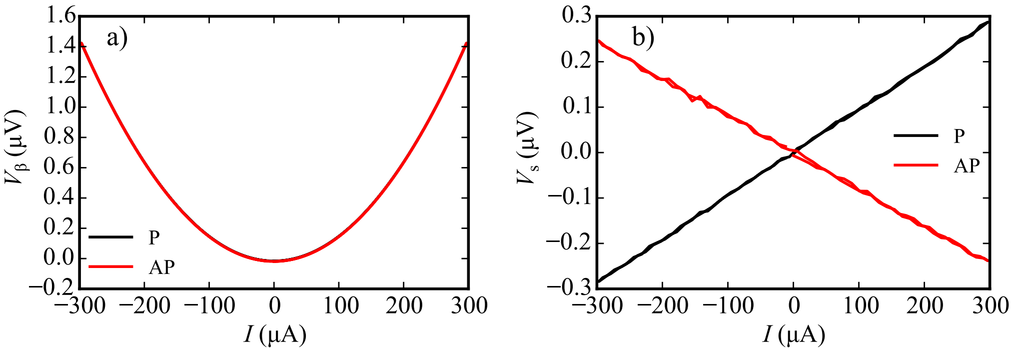

Figure 4.5: Decomposed nonlocal signal from NLIV shown in Fig. 4.4 at 30 K. a) Voltage after subtraction of the linear spin signal leaves the remaining field independent quadratic background. b) Spin voltage from nonlocal IV after subtraction of the quadratic signal.

ted in Fig. 4.5 (b). The end result is a voltage, linear in current, that exhibits a strong dependence on the magnetic configuration. This shows what would be expected of the spin signal from theory[7, 28] and as seen from previous experiments on DC injection[13], where the spin current has a bipolar dependence on the charge current. This linear behaviour also demonstrates that there are no higher order terms present in the NLIV.

4.4.2 Quadratic Coefficient

It was previously considered that V_β is a result of Joule heating at the injector. The detection of this heating in the nonlocal measurements is possible due to the large thermal conductivity (κ) of Cu and difference in Seebeck coefficients of Cu[71] and Py[72]. The charge current causes Joule heating at the injector electrode and a thermal current flows along the Cu wire, due to its large value of κ, raising the temperature of the detector interface (T_d) with respect to the substrate (T_sub). As mentioned, the Seebeck coefficients of Cu and Py can be very different, at room temperature $S_\mathrm{Py} = -20\ \mu\mathrm{V\ K}^{-1}$[72] while Cu is much smaller $S_\mathrm{Cu} \approx 1.8\ \mu\mathrm{V\ K}^{-1}$[71]. As such, the open circuit voltage detection used in nonlocal measurements means the detector circuit acts as a thermocouple and is sensitive to any temperature difference between the T_d and T_sub. This effect is only visible when using DC injection[13] or observing the higher order harmonics in AC lock-in techniques[68] and so is often overlooked. Figure 4.6 (c) shows a schematic diagram of the detection circuit. The voltage due to the Seebeck effect can be written as:

$$V_\beta = \int_{T_\mathrm{i}}^{T_\mathrm{sub}} (S^+ - S^-)\mathrm{d}T, \tag{4.2}$$

where $S^{+(-)}$ is the effective Seebeck coefficient along the path of the positive (negative) voltage leads. In general these are themselves temperature dependent and a non-trivial mixture of contributions from Cu, Py and Au—most notably along the negative lead due to the Py/Cu bilayer. Since the Seebeck coefficient of Py is much larger than Cu and Au Eq. 4.2 can be simplified assuming the majority of the thermopower signal is caused by Py close to the interface leading to:

$$V_\beta = (S_\mathrm{Cu} - S_\mathrm{Py})\Delta T, \tag{4.3}$$

where $\Delta T = T_\mathrm{d} - T_\mathrm{sub}$. Using the room temperature values quoted above for S and assuming a positive ΔT (as would be expected for Joule heating at the injector) it is obvious that V_β is also positive as seen in NLIVs and Fig. 4.5 (a). For a LSV with $L = 1.325\ \mu\mathrm{m}$, $\beta = V_\beta / I^2 = 6.2$ V/A^2 is measured and with Eq. 4.3, ΔT is estimated to be ≈ 26 mK. This estimate is highly dependent on the choice of S, which has been shown to depend on the microstructure and thickness of the materials [73, 74]. Without detailed measurements of the effective Seebeck coefficient of the detector circuit an exact measurement of T_d is not obtainable. Work by the author's colleague G. Stefanou in collaboration with F. Menges and B. Gotsmann at IBM Zürich on similar structures have shown a qualitative agreement with this picture, where scanning thermal microscopy shows the heat dissipation through a LSV raising the temperature of the detector by a similar amount.

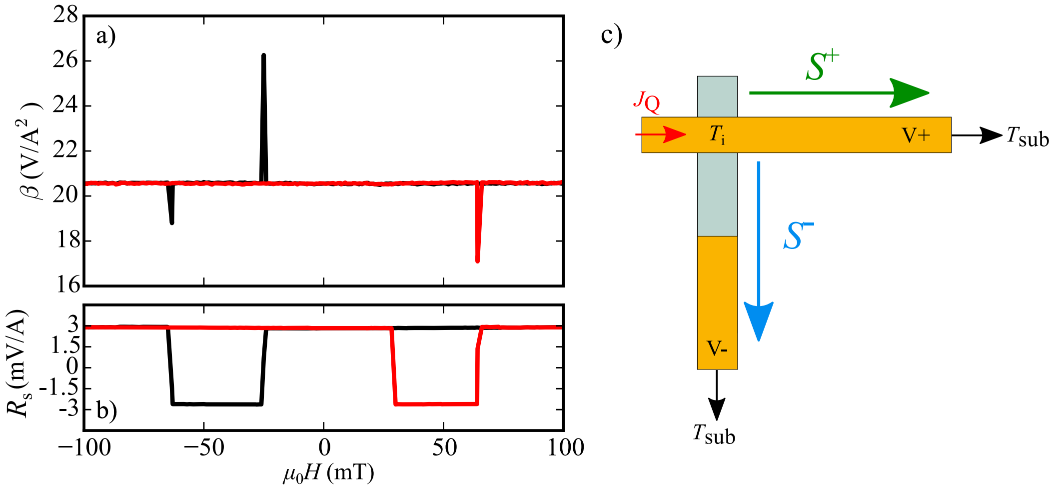

Figure 4.6: a) Magnitude of the quadratic coefficient from nonlocal IVs as a function of applied field for a LSV with magnetic electrode separation $L = 300$ nm at 10 K. Spikes in the data occur when the FM electrodes reverse. This is not always detected if the field step is larger than the width of the reversal. b) The corresponding linear coefficient measured at the same time showing the FM switching fields. c) Schematic of the detection circuit of a LSV. The heat current J_Q from joule heating at the injector raises the temperature of the detector interface T_d with respect to the substrate temperature at the end of the voltage leads.

Although there is no difference in V_β between the P and AP states Fig. 4.6 shows that there are some field dependent features in the Joule heating coefficient β. The spikes in the measured signal exactly coincide with the switching fields of the FM electrodes shown in Fig. 4.6 (b), where the higher switching field at 65 mT is due to the reversal of the injector electrode. When the injector switches β shows a sharp reduction in magnitude and is possibly a consequence of the AMR of the Py also observed by Slachter *et al.*[75]. During the reversal, at some stage its magnetisation becomes perpendicular to the current flow and its resistance drops. Since the Joule heating efficiency is proportional to the resistance, this results in a slight reduction in the heat current along the Cu wire and is detected as a reduction in the Seebeck voltage. Although this predicts the correct sign change the magnitude of the change in β is around 10–15%. This is in general much larger than a typical change in resistance due to AMR and indeed larger than the effect observed in [75]. At present it is unclear how this small resistance change can cause a larger reduction in the measured signal.

A peak in β is also observed when the detector electrode reverses its magnetisation. Since there is no current flow in this part of the circuit this is not related to the AMR of the FM but instead a voltage contribution from the anomalous Nernst effect[75, 76]. The Nernst effect can be considered as a thermoelectric equivalent to the anomalous Hall, where a transverse voltage to both the current flow and magnetisation occurs. Hence the Nernst voltage gradient $\vec{\nabla} V_{\mathrm{N}}$ is proportional to the cross product of the magnetisation and, in this case, temperature gradient as:

$$\vec{\nabla} V_{\mathrm{N}} = S_{\mathrm{N}} \vec{m} \times \vec{\nabla} T \tag{4.4}$$

where $\vec{m}$ is the unit vector along the direction of magnetisation and $S_{\mathrm{N}} = R_{\mathrm{N}} S$ is a transverse Seebeck coefficient, which is some fraction of the conventional Seebeck coefficient determined by the Nernst equivalent of the Hall coefficient R_N. At the detector interface there will be a thermal gradient into the plane of the sample across the Cu/Py interface caused by Joule heating at the injector. As $\vec{m}$ generally lies along the length of the Py electrode this produces a constant voltage across the width of the Py. When $\vec{m}$ rotates to become briefly perpendicular to the length of the electrode a Nernst voltage is generated along its length and this change is detected within the voltage circuit. Since the reversal of the FM electrodes occurs over a very small field range the observation of both these effects is dependent on the distribution of field steps and so are not always present in the measurements due to the stochastic nature of the reversal.

The most significant contribution to the nonlocal thermal signal β is Joule heating at the injector. This has been measured as a function of temperature and separation of the FM electrodes, as shown in Fig. 4.7. Here the same linear dependence on L as observed by Bakker et al.[68] is seen. The temperature dependence of β is a result of changes in the generated heat as the resistance of the device is reduced at low temperatures, reduction in heat transport as thermal conductivities (κ) diminish with temperature and the temperature dependence of the Seebeck coefficients. All of these can exhibit complex behaviour at low temperatures[71, 77, 78] where peaks in κ and even changes of sign in S may be the cause of

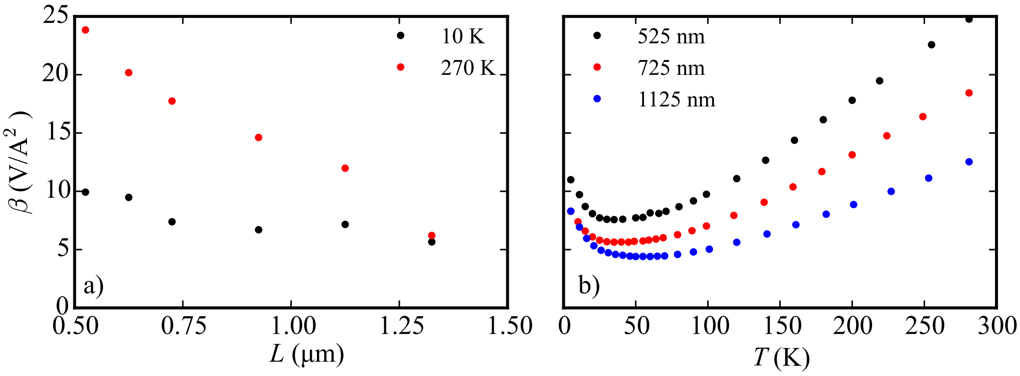

Figure 4.7: a) Decay of quadratic term as a function of electrode separations at 10 and 250 K. b) Quadratic coefficient as a function of temperature for varying electrode separations

the low temperature upturn observed in Fig. 4.7 (b). Unfortunately without detailed knowledge of these parameters no quantitative details of the heat currents within LSVs can be made.

The heating at the injector has been show to affect the magnitude of the spin injection due to the spin-dependent Seebeck effect[21–23]. At large current densities, greater than 5×10^{11} A/m^2, the higher resistivity of the Py electrode causes greater Joule heating than the Cu, forming a temperature gradient at the interface. Due to the spin dependent conductivities of the Py this temperature gradient can cause a net injection of spin. However, the maximum current density used in measuring devices in this thesis is only 5×10^{10} A/m^2 and no nonlinear behaviour is observed in the V_s. Therefore, although the nonlocal signal due to thermal effects (V_β) is greater than the spin signal this is a consequence of the high sensitivity of Cu/Py LSVs to thermal currents and not an excessive amount of Joule heating.

4.4.3 Linear Coefficient

Previously the assumption had been made that the linear component of the NLIV represented the signal due to electrical spin injection. Figure 4.8 (a) & (b) show R_s as a function of an in-plane magnetic field. The data presents what would typically be expected from a DC reversal or AC lock-in technique measurement for a LSV, confirming the interpretation of the NLIV components. At large field both electrodes are saturated and aligned parallel giving a positive R_s. As the field is reduced, upon crossing zero it first reaches the coercive field of

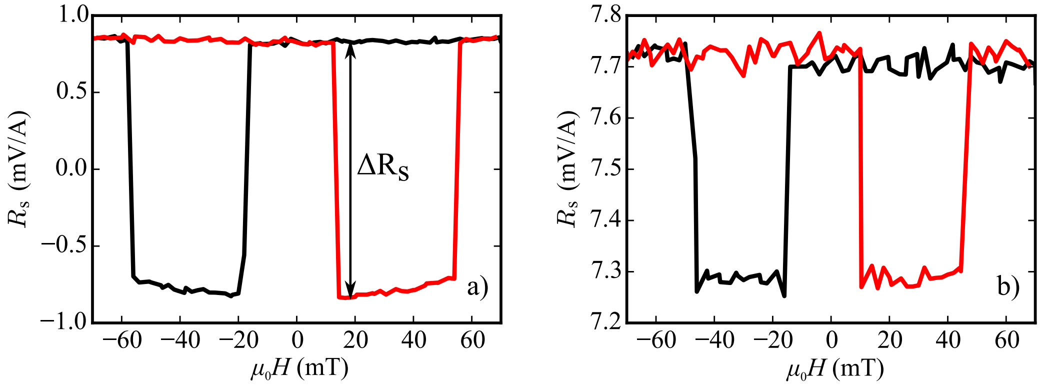

Figure 4.8: Linear component of NLIV as a function of applied magnetic field at a) 5 K and b) 280 K of a LSV with magnetic electrode separation $L = 425$ nm.

the easy electrode (~ 20 mT) causing the reversal of its magnetisation and forming an AP configuration. As the magnitude of the applied field is increased there is a slight slope in R_s with field. This behaviour is not always present and is a consequence of closure domains forming within the FM electrodes causing a reduction in the effective polarisation at the interface. As discussed above, the wires were designed with pointed ends to avoid the formation of such domains, however non-ideal fabrication conditions (slight overdevelopment, incorrect deposition angle) can cause the wire end to become rounded. The formation of a domain below the Cu wire results in a non-collinear orientation of the magnetisation of the two electrodes and a reduction of R_s. In this case to calculate ΔR_s the AP value for the lowest field is used, before the formation of domains. At a higher field the second FM will switch and the P state is recovered. This characteristic signal is the same as seen in conventional AC lock-in and DC reversal techniques when measuring R_s of LSVs further confirming the interpretation of the fits to the NLIV.

At low temperatures the magnitude of R_s is symmetric about zero for the P and AP states. Since there is no spin asymmetry within copper this should guarantee an equal divergence of each spin type from the equilibrium electrochemical potential thus an equal but opposite spin signal when the spin axis is reversed in the detector electrode as shown in Fig. 2.3. However, the data taken at 280 K, shown in Figure 4.8 (b) does not display this bipolar effect as R_s for both P and AP are positive.

The full temperature dependence of R_s for both P and AP states is shown in Figure 4.9 (a). The bipolar switching for P and AP is visible at low temperatures but a clear transition away from this is observed as both values rise with increasing temperature. The difference between the two curves, shown in Figure 4.9 (b), is labeled as ΔR_s and is the common focal point within literature as it represents the magnitude of spin accumulation within the Cu. There is a general trend of increasing magnitude with the reduction in temperature, along with the formation of a peak at low temperatures, the details of which will be discussed in the following chapter. For now, the focus will be on the quantity labeled $\bar{R}_\mathrm{s}$ in Figure 4.9 (c) defined as the mean value of R_s for the P and AP state:

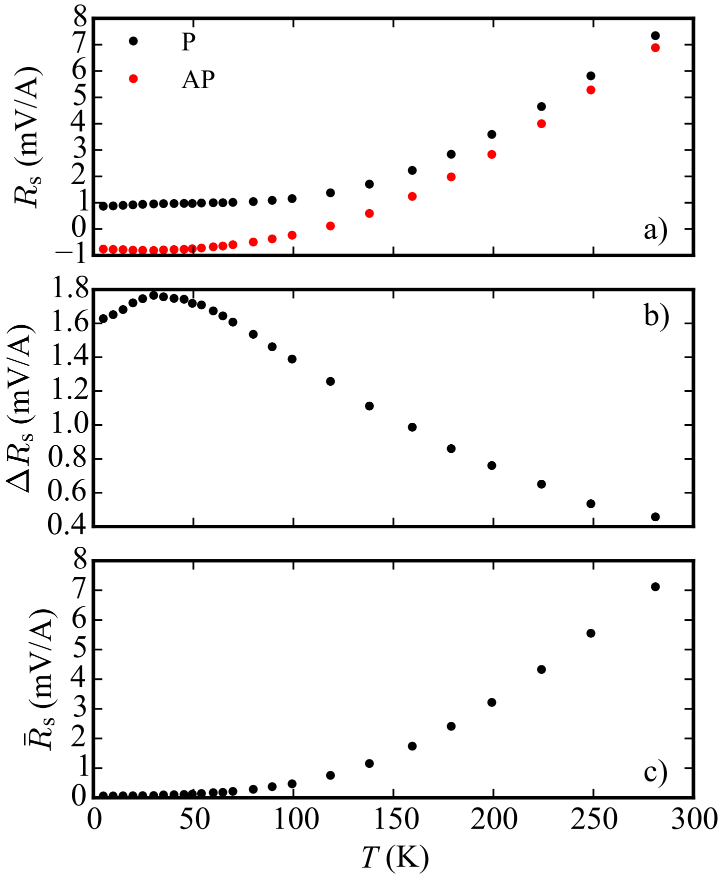

Figure 4.9: a) Magnitude of the spin signal in the parallel (P) and antiparallel (AP) states as a function of temperature for a device with magnetic electrode separation $L = 425$ nm. b) ΔR_s as a function of temperature. The magnitude of the spin current increases with decreasing temperature until a peak at ~35 K. This feature is discussed in more detail in Chapter 5. c) The mean value of R_s in the P and AP states. This vanishes at low temperatures and is a consequence of the Peltier effect.

$$\bar{R}_\mathrm{s} = \frac{R_\mathrm{s}^\mathrm{P} + R_\mathrm{s}^\mathrm{AP}}{2} \tag{4.5}$$

In most studies the characterisation of LSVs focuses on ΔR_s due to its direct link to the spin accumulation. Yet, the effect of this background signal is always present and generally overlooked or ignored. One explanation by Jonson and Silsbee[69] stems from a nonuniform current injection generating a geometry dependent voltage at the detector electrode. However, this is predicted to decay exponentially and to only have a significant contribution when the separation of the FM electrodes is comparable to the width of the Cu wire, w_Cu. Within this work no LSVs were measured where $L < 3w_\mathrm{Cu}$, and so, far from a regime where the voltage from nonuniform current distribution is observable. Also, the dependence of $\bar{R}_\mathrm{s}$ on L show in Fig. 4.10 (a) displays no exponential decay but is instead linear. This linear dependence on L was also observed in β and indicates that this field independent contribution to the linear response of the NLIV is a thermal phenomenon.

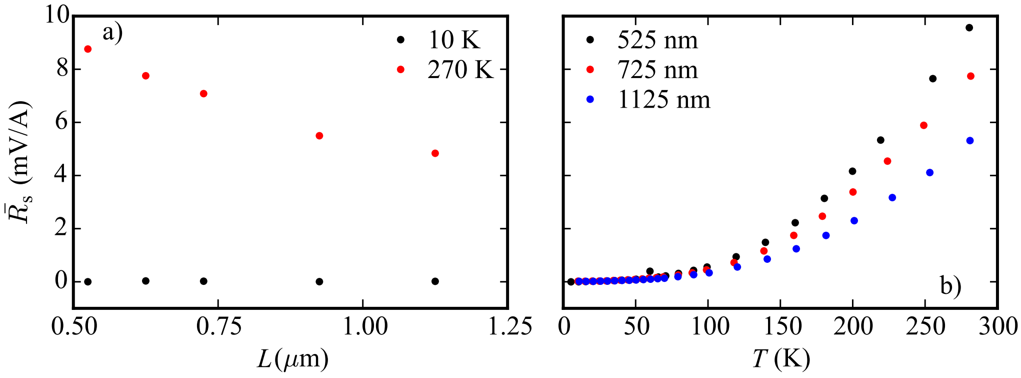

Figure 4.10: a) Decay of the field independent part of the linear term $\bar{R}_\mathrm{s}$ as a function of electrode separations at 10 and 250 K. b) $\bar{R}_\mathrm{s}$ as a function of temperature for varying electrode separations.

Studies of this background have postulated that the Peltier effect is the origin. Bakker et al.[68] demonstrated that the linear dependence on both the injection current and L show this to be a heat flow along the Cu due to Peltier heating/cooling at the injector. The Peltier effect describes the heat current absorbed when a charge current flows across the interface of two materials that have different Peltier coefficients. The absorbed, or generated, heat is described by:

$$J_Q = (\Pi_{Cu} - \Pi_{Py})I, \tag{4.6}$$

where $\Pi_i = S_i T$ is the Peltier coefficient and is related to the Seebeck coefficient of the material. The Peltier effect can heat or cool the interface depending on the sign of the current and produces an extra heat flow along the Cu wire with a linear relation to the injection current. This is detected again through the Seebeck effect and as such shows similar diffusion along the Cu as the Joule heating thermal current and shown in Fig. 4.10 (a). Further, Fig. 4.10 is the temperature dependence of $\bar{R}_s$, which tends towards zero at low temperatures. This is expected for the Peltier effect which vanishes as T goes to zero.

4.5 Conclusion

Within this chapter the basics of LSVs have been discussed. Two methods for measuring R_i were shown, highlighting the difficulty in measuring low contact resistances for materials with very different conductivities. Throughout the literature, values for R_i are obtained from cross devices or LSVs themselves[11, 13, 79]. However, it is only in two studies, O'Brien *et al.*[11] and Villamor *et al.*[79], where the negative resistance commonly seen in earlier research on low-impedance tunnelling junctions[64, 80] is commented on. The direct observation of a negative R_i is only possible with low resistance contacts and without consideration of this effect measured values of R_i may not correctly estimate its true magnitude. The combination of measurements and simulations performed in this thesis show that the fabricated device are within the transparent limit. This is a key result as it demonstrates the quality of devices fabricated through the shadow lithography and angled deposition technique developed during this work.

The design of LSVs has been discussed and the ability to precisely control the magnetic configuration of the FM electrodes proven. This is pivotal in nonlocal measurements as the magnitude of R_s is strongly dependent on the orientation of the injector/detector magnetisation. Many studies are made on LSVs which have partial switching of the FM electrodes[22, 81, 82], displaying steps or triangular switching in R_s as a function of field. This is undesirable, creating ambiguity in defining the magnitude of ΔR_s and hence the spin current. This chapter has shown that a very clear AP state is achieved over a field range much greater than the step resolution of the solenoid and power supply. The well defined P and AP states in the devices used for this study ensures reliable measurements of ΔR_s to be made.

Finally the different nonlocal signals have been discussed. This work departs from the conventional AC lock-in or DC reversal techniques to observe the full nonlocal direct current-voltage characteristics. This method allows the observation of thermal and spin transport without the need for multiple lock-in amplifiers[68]. Through observations of the current and field dependence this allows the separation of thermal transport due to Joule heating and Peltier heating/cooling at the injector, while also measuring spin transport.

CHAPTER 5

Spin Relaxation through Kondo Scattering

5.1 Introduction

The spin diffusion length, λ_{s}, characterises the decay of a pure spin current and can be obtained from measurements of ΔR_{s} from LSVs as a function of spin injector to detector distance, L. The dependence of this length scale on the various scattering mechanisms is a highly contentious point. Both intrinsic and extrinsic spin scattering in an NM can be of similar magnitudes and vary according to the material quality within a specific sample. The understanding of the mechanisms that can destroy spin accumulation is crucial to the study of spin transport and its resulting exploitation[4–6]. This chapter focuses on the spin relaxation effects in LSVs and the work presented here forms a manuscript published in Physical Review B[83].

It is widely observed that the temperature dependence of ΔR_{s} within Cu/Py LSVs is non-monotonic exhibiting a peak around 30 K[11, 19, 25, 84, 85], with similar behaviour also observed in LSVs containing other NM materials[32, 86]. Figure 4.9 (b) shows the ΔR_{s} as a function of temperature for a single LSV highlighting this non-monotonic temperature dependence. As discussed in Chapter 2, spin relaxation in NM materials is governed by the Elliot-YaffYafetet mechanism[29, 30] and so expected to be inversely proportional to the resistivity. Since the magnitude of ΔR_{s} is dependent on the spin diffusion length (λ_{NM}) and hence spin-scattering in the NM we would assume $\Delta R_{\mathrm{s}} \propto T^{-1}$ at high temperatures, and eventually reaching a plateau at low temperature. However, this behaviour is rarely seen and for more than a decade this critical issue of the non-monotonic nature of the spin signal has prompted many models focusing on either scattering effects altering λ_{NM}[31, 32, 79, 86] or changes in the spin polarisation of the FM/NM interface α[11], yet no consistent solution has been presented.

Most of the present literature concentrates on scattering events within the NM channel. The initial observation of this by Kimura et al.[25] shows a similar behaviour to that seen in Fig. 4.9 (b). The peak is attributed to a corresponding peak in the spin diffusion length of copper (λ_{Cu}) obtained from fits to a 1-D model. They hypothesise a reduction in λ_{Cu} at low temperatures is due to additional scattering from the surfaces of the Cu. As the LSV is cooled the electron mean free path (λ_{e}) increases, which, when comparable to the dimensions of the wire, introduces an increased scattering rate from the surfaces. They highlight the effect by measuring the peak position as a function of the thickness of the Cu channel, where the maximum in ΔR_{s} shifts to lower temperatures for thicker Cu, supporting the scenario of surface scattering. This is similarly observed by Erekhinsky et al.[84] where an increase in

λ_{Cu} can be correlated to the increase in thickness and as such, indicates some feature of the surface of the Cu is a strong spin-flip scatterer. Interestingly they show that λ_{Cu} can increase in samples that have been exposed to atmosphere and formed a Cu oxide layer on the surface. Further research by Mihajlovic et al.[32] draws the same conclusion through measurements of the spin relaxation time (τ_{sf}) via the Hanle effect, which shows the familiar peak as a function of temperature. Although no thickness dependence is investigated, here a more quantified approach allows the extraction of phonon ($\varepsilon_{\mathrm{ph}}$), impurity ($\varepsilon_{\mathrm{imp}}$) and surface ($\varepsilon_{\mathrm{s}}$) spin flip probabilities, where $\varepsilon_{\mathrm{i}} = \tau_{\mathrm{e}}^{\mathrm{i}}/\tau_{\mathrm{s}}^{\mathrm{i}}$ as defined in Eq. 2.19. They obtain $\varepsilon_{\mathrm{imp}} = -5 \times 10^{-3}$ and $\varepsilon_{\mathrm{ph}} = 8 \times 10^{-3}$ where $\varepsilon_{\mathrm{ph}}$ agrees with experiments on bulk Ag[87]. Interestingly the value obtained from the fits for surface scattering $\varepsilon_{\mathrm{s}} = 1.7 \times 10^{-2}$ is much larger than other mechanisms. However, they report a negative value for $\varepsilon_{\mathrm{imp}}$ which brings into doubt the validity of their analysis. These studies all suggest that there is some property of the NM spacer's surface which acts to strongly scatter spins.

Complementary to the above results is work by Zou and Ji[31] where the temperature dependence of ΔR_{s} was observed over an extended time period. As with the work above the samples were fabricated through angled deposition but here show a return to a monotonic temperature dependence after the device has been exposed to atmosphere for 143 days. Zou and Ji state that due to the angled deposition the side wall of the resist becomes coated in FM material. Then, during the growth of the NM the energy of the adatoms is sufficient to dislodge FM materal from the resist causing impurities in the outer layers of the NM. While exposed to air the Cu will oxidise, removing the regions contaminated with magnetic impurities from the conduction channel, preventing them from scattering spins. However, they show no measurements of λ_{Cu} in the oxidised samples and no quantitative analysis.

Idzuchi et al.[86] support the concept of a reduction in λ_{NM} due to surface interactions. Experiments were performed with Py/Ag LSVs with and without an MgO capping layer, where the addition of MgO recovers the expected monotonic temperature dependence of λ_{Ag}. Their argument states that the capping with MgO alters the effective Z at the surface and reduces the spin flip probability. Idzuchi et al. do not perform a similar analysis to Mihajlovic as it is not valid for their experiment. However, recently they have been able to quantify the relative changes in surface scattering for various metal oxides and show an increase in spin flip scattering for heavy elements[88].

All the studies mentioned so far have fabricated LSVs through a shadow deposition technique and draw conclusions that some property of the surface of the NM channel causes a large amount of spin-flip scattering. Of these, experiments that introduce a surface oxide appear to reduce this strong spin-flip scattering. Since the Elliot-Yafet spin-flip mechanism is a spin orbit effect, the oxide at the surface of the NM may alter this by changing the effective Z seen by the conduction electrons. However, the inclusion of magnetic impurities through the fabrication process, which are then removed from the conduction channel through oxidation, is also able to explain the observed results and it is difficult to distinguish between the two suggestions with the available data.

Villamor et al.[19] have undergone the same work though a two step lithographic process. Expanding on the work of Kimura et al. they measured λ_{Cu} in the Cu channel for a range of thicknesses but do not see the same shift in the peak position. The absence of any changes with the thickness of the NM indicates that, within the two step lithography LSVs, the origin of the increased spin relaxation at low temperatures is a bulk effect. This increases the likelihood that the cause of the non-monotonic temperature dependence is magnetic impurities (MIs). Villamor et al. states that there may be MIs present within their source material and the contamination of the NM in shadow deposition, either during growth or liftoff, is highly likely thus providing a reasonable explanation for the low temperature spin dephasing. However, no proof of the presence of MIs within the NM nor any quantitative explanation of their effect has been presented within the literature, which this work aims to resolve.

5.2 Experimental Details

LSVs were fabricated through a double dose electron-beam lithography and shadow deposition technique as outlined in Chapter 3. In order to investigate the effect of the spacer channel material quality, specifically the MI concentration, on the nonlocal signal, two sets of LSVs have been fabricated. The two sample sets contain Cu evaporated from different quality source material of 99.99% (four-9s) and 99.9999% (six-9s).

The four-9s sample set was fabricated initially, with a base pressure of the order 10^{-10} mbar. The FM is deposited first, with 25 nm of Py evaporated at 45°, followed by the NM, 100 nm of Cu normal to the substrate. Figure 5.1 (a) is a scanning electron micrograph of a typical device. The FM electrodes have widths of 140 nm and 100 nm, with a large nucleation pad on the wider wire to facilitate independent magnetisation reversal. The connecting copper wire has a width of 130 nm and devices were prepared with a range of separations between the magnetic electrodes from 450 nm to 1370 nm.

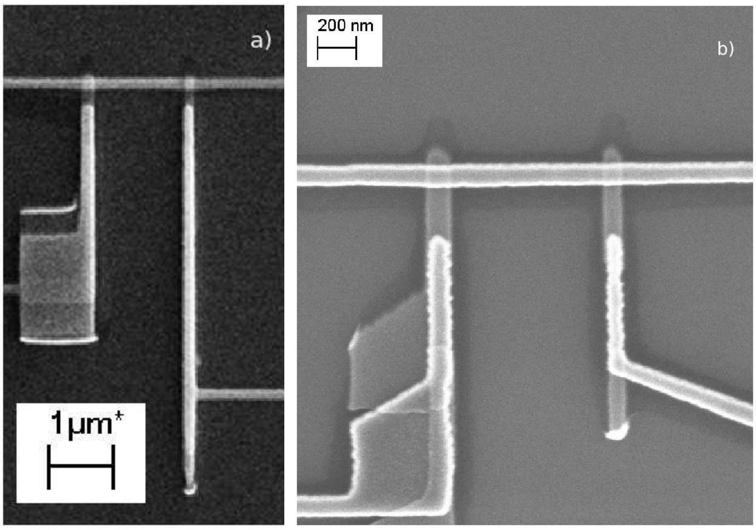

Figure 5.1: Scanning electron micrograph showing typical LSVs from the two sample sets. a) four-9s and b) six-9s.

In order to prepare the six-9s samples the deposition system was vented and the Cu source replaced with the higher purity material. The system was then pumped and baked until an equivalent base pressure to the four-9s samples was achieved. Figure 5.1 (b) shows a typical LSV from the six-9s sample set. Here 20 nm of Py is evaporated at 45° and the widths of the FM electrodes are 115 nm and 90 nm, where the wider wire has the nucleation pad. The Cu spacer has a width and thickness of 100 nm and 85 nm respectively. Although the dimensions of the Cu track are different between the two sample sets this does not contribute significantly here to the differences in λ_{Cu} as will be discussed further on.

Figure 5.2 shows the resistivity of the Py used during the calculation for λ_{Cu} and interface spin polarisation α for both sample sets. The resistivities are obtained from samples deposited within similar conditions to the LSVs. There is a slight increase in resistivity for the Py used within the six-9s LSVs due to a reduction in the thickness used and slightly reduced deposition rate. However this will not affect the properties of the Cu, on which this study focuses.

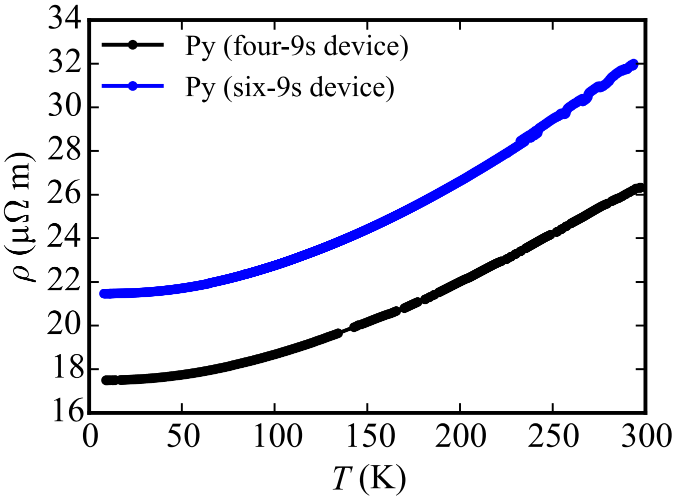

Figure 5.2: Resistivities of Py electrodes as a function of temperature used in calculation of λ_{Cu} and α for both sample sets.

5.3 Charge Transport

The resistivity for both types of Cu obtained directly from the LSVs is shown in Fig. 5.3 (a). It is immediately clear that the lower purity four-9s Cu has a higher resistivity at all temperatures. This is a consequence of an increase in disorder within the material due to the presence of more impurities. Figure 5.3 (b) shows the low temperature data for the change in resistivity from the minimum value for both sample sets where again they display different behaviours. The four-9s sample set has a very clear upturn with a resistance minimum temperature $T_{\mathrm{min}} = 11$ K which is not present in the six-9s sample. Although there is a small change in the resistivity of the six-9s Cu at around 4 K this is of similar magnitude to the noise level and not of reliable significance.

5.3.1 Origin of the Resistance Minimum

In many systems the observation of a resistivity minimum indicates the presence of localisation. Localisation effects, including Anderson localisation, are present in samples with a significant amount of disorder that is usually identified by the resistivity and its temperature dependence. However, the resistivity of the most resistive four-9s Cu is 2 μΩ cm (i.e. $\ll$ 100 μΩ cm—the Mooij critical value[89]), and the temperature dependence of ρ is that of bulk

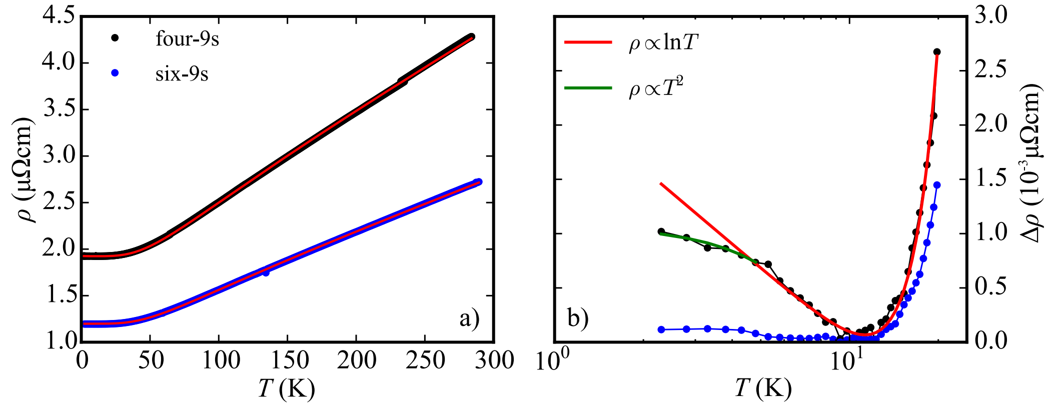

Figure 5.3: a) Resistivity as a function of temperature for Cu in both the four-9s (black) and six-9s (blue). Due to the lower purity, the four-9s has a higher amount of disorder and a higher resistivity. The red curves are fits to Equation 5.1b. b) Low temperature $\Delta\rho = \rho(T) - \rho(T_{\text{min}})$ data showing the resistivity minimum caused by MIs. Red curve is a fit to Equation 5.1b showing the lnT temperature dependence expected of the Kondo effect. The green curve highlights the T^2 regime where the MIs begin to be screened and electron-electron interactions occur.

Cu and therefore does not display features associated with weak localisation. The observation of Anderson localisation can occur in systems with reduced dimensionality provided the resistivity is sufficiently high[90, 91]. A wire with resistivity 100 μΩ cm and radius of 25 nm will approach the one-dimensional regime and display localisation effects below 1 K. Since the Cu wires used in this study have a much larger cross sectional area of 1.4×10^{-14} m^2 and resistivity 50 times smaller, the critical temperature for localisation effects is far below our experimental range.

Weak anti-localization effects due to spin orbit coupling, meanwhile, can be observed in clean materials[92]. However, weak anti-localization shows the opposite sign of $d\rho/dT$ to weak localization [93] and to that seen in this experiment, so can be discounted.

This analysis leaves the Kondo effect[33] as the only viable candidate to describe the change in the resistivity. Cu-Fe is a very well characterised Kondo system that typically displays a resistance minimum in this temperature region[94]. Through sensitive resistivity measurements, and the presence of the Kondo effect, it is possible to detect the existence of MIs within a non-magnetic host. Analysis from the manufacturer shows the most significant impurities in the four-9s Cu are Ni and Fe with concentrations of 15 and 12 ppm respectively. Since the Kondo temperature for Ni impurities in Cu is greater than 1000 K[95], no resistance minimum is observed from Ni[55] and it is assumed that only Fe impurities contribute to this. Through the empirical expression for Fe impurities in a Cu host $T_{\text{min}} = 115c^{1/5.3}$[33] the concentration of MIs was found to be c = 4 ppm. This is lower than the source material, probably due to a differential evaporation rate of the constituent elements.

A smoking gun for the Kondo effect is the observation of electron-electron interactions. The temperature dependence of the Kondo effect has been shown to exhibit a logarithmic term due to magnetic impurity scattering that becomes a T^2 dependence well below the Kondo temperature, where screening of the impurities and electron-electron interactions become dominant[56]. This is exactly seen with a crossover between the two regimes around 4 K, as shown in Fig. 5.3 (b). It is at this temperature that the original description by Kondo[33] using second order perturbation theory breaks down. However, the lnT temperature dependence is used in the analysis of the spin-flip scattering as the spin transport measurements are performed at temperatures far from when screening effects occur and the result from perturbation theory is valid.

5.3.2 Momentum Relaxation Rates

With observations of charge transport through the NM spacer, details of the different momentum relaxation rates were obtained. Since the Elliot-Yafet theory links the momentum and spin relaxation through spin-orbit coupling, this allows the determination of the dominant spin-flip mechanism. A phenomenological model is built upon a combination of Bloch-Grüneisen and Kondo terms to account for phonon and magnetic impurity scattering:

$$\rho = \rho_{\text{i}} + \rho_{\text{p}} + \rho_{\text{m}} \tag{5.1a}$$

$$\rho = \rho_0 + K\left(\frac{T}{\Theta_{\text{D}}}\right)^5 \int_0^{\frac{\Theta_{\text{D}}}{T}} \frac{x^5\,dx}{(e^x-1)(1-e^{-x})} + \rho_{\text{K}}\text{lnT} \tag{5.1b}$$

where ρ_0 is the residual resistivity due to non-magnetic impurities and defects, K is a material specific constant, Θ_{D} is the Debye temperature and ρ_{K} is the Kondo resistivity. The fit of Eq. (5.1) to the data is shown in Fig. 5.3 (a) & (b) where it accurately reproduces all the features, including the Kondo minimum in the four-9s sample set. Values for Θ_{D} for high and low purity Cu are extremely close, 283.7 ± 0.7 K and 281.1 ± 0.6 K respectively. The constant K for the two sample sets are $(6.13 \pm 0.02) \times 10^{-7}$ Ωm and $(9.79 \pm 0.03) \times 10^{-7}$ Ωm for six-9s and four-9s respectively. These values are dependent on the microstructure but are all in good agreement with those reported for Cu elsewhere[96, 97]. The momentum relaxation rates were then evaluated through the free electron Drude approximation $1/\tau_e = ne^2\rho_e/m_e$ where n is the conduction electron density and ρ_e is the resistivity for the individual scattering contributions shown in Eq. (5.1a).

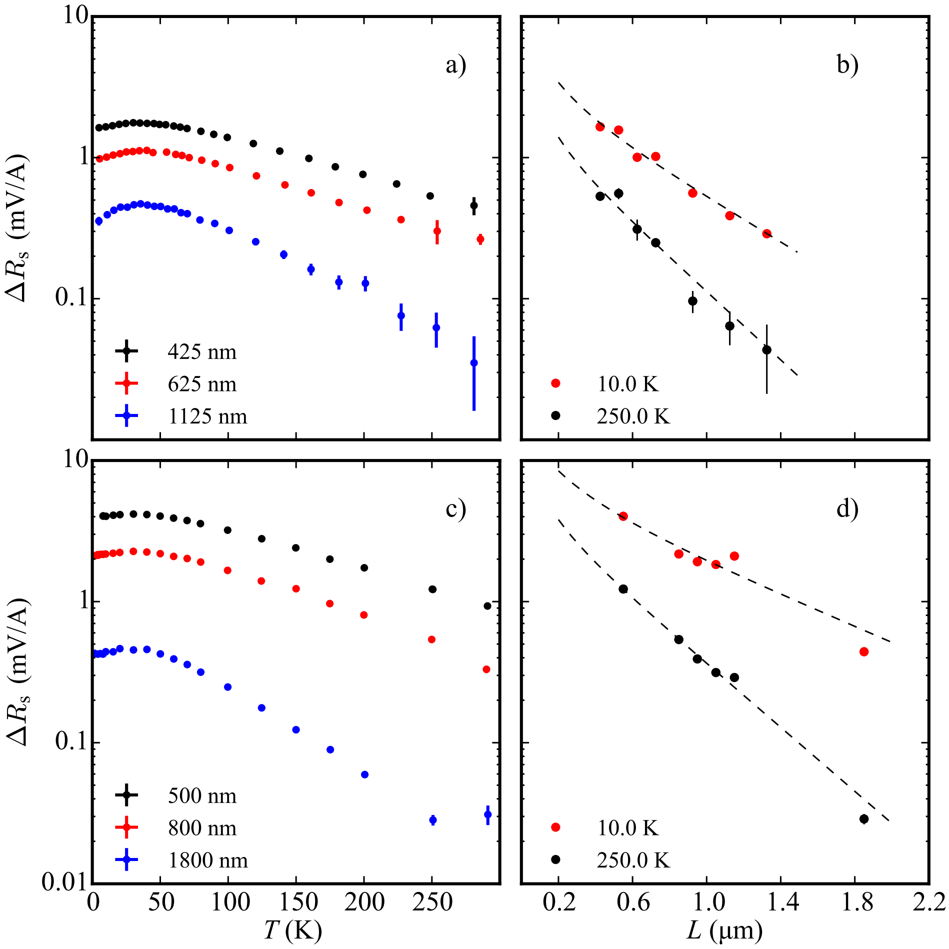

Figure 5.4: a) four-9s & c) six-9s ΔR_s as a function of temperature for a LSVs with varying magnetic electrode separation L. b) & d) show the decay of ΔR_s with lateral separation L at 10 and 250 K. The dotted lines are fits to Eq. 2.13.

5.4 Spin Transport

Lateral spin valve measurements were performed in the geometry discussed in Chapter 2 section 2.3.1 and ΔR_s obtained though the method outlined in Chapter 4. For each purity of Cu, ΔR_s was measured as a function of temperature in a helium flow cryostat for a series of LSVs of different electrode separations L. Figure 5.4 (a) & (c) show ΔR_s as a function of temperature for some values of L for the four-9s and six-9s sample sets respectively. The general trend for all devices is the same, with an increase in ΔR_s for smaller values of L. It can also be seen that ΔR_s is larger in six-9s samples, which moreover, show a smaller downturn at low temperatures. In order to fit ΔR_s as a function of L to Eq. 2.3, it is assumed that $\lambda_F \propto \sigma_F$ and fixed to a value of 5.5 nm at 4.2 K[98] as similar to elsewhere[19]. This leaves λ_N and α as free fitting parameters. The fits were performed at different temperature (see Fig. 5.4 (b) & (d)) to obtain temperature dependent data on the spin relaxation within Cu.

Figure 5.5 shows the values for the spin diffusion length obtained from fits to Eq. 2.3 at various temperatures for both four-9s and six-9s LSVs. Whilst the values for λ_{Cu} lie well within the range of published values[10, 13, 19, 25, 31], the two Cu purities show a significantly different temperature dependence. The four-9s purity Cu, in which there is a clear resistance minimum, displays the commonly observed non-monotonic temperature de-

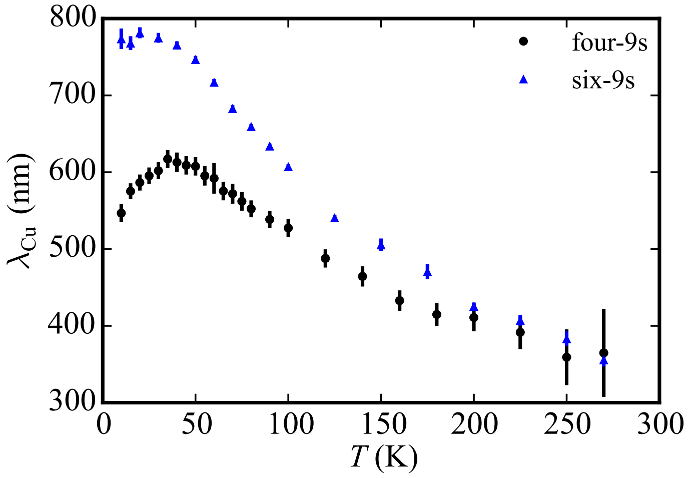

Figure 5.5: Spin diffusion length obtained from fitting data from four-9s (black circles) and six-9s (blue triangles) LSVs. The four-9s samples have a clear peak at 35 K where as the six-9s, within the uncertainty, have a monotonic temperature dependence and a large value at low temperatures.

pendence with a peak around 35 K. In contrast, the six-9s sample set produces, within experimental uncertainty, a monotonic variation with temperature. Here we see a direct link between the presence of MIs and the reduction in λ_{Cu} that is seen throughout literature[19, 25, 31, 32, 86]. If surface spin flip scattering[25, 32] were to be a major contribution it would be more dominant within the six-9s sample set, as they have both a longer electronic mean free path (lower resistivity) and smaller cross sectional area compared to the four-9s samples. However, a much larger λ_{Cu} is observed within the six-9s samples indicating that the purity of the Cu, specifically the concentration of MIs, is a more important factor in the suppression of λ_{Cu}.

The combination of measurements on charge and spin transport can be used to provide a qualitative analysis of the contribution to spin relaxation from MIs. The spin diffusion length can be defined as $\lambda_{\mathrm{s}} = \sqrt{D\tau_{\mathrm{sf}}}$, where D is the diffusion coefficient and τ_{sf} the spin-flip scattering rate. Using the Einstein relation $e^2 N(\epsilon_{\mathrm{F}}) D = \sigma$, where $N(\epsilon_{\mathrm{F}})$ is the density of states at the Fermi energy and σ is the electrical conductivity, D is obtained. Assuming a free electron model and taking $N(\epsilon_{\mathrm{F}}) = 1.8 \times 10^{28}$ states/eVm^3[99], with the measured resistivity the spin-flip scattering time is calculated as shown in Figure 5.6 (a) & (b). Within nonmagnetic metals the spin relaxation can be described through the Elliot-Yafet[29, 30] mechanism which, due to spin-orbit coupling, links the momentum and spin relaxation times $1/\tau_{\mathrm{sf}} = \varepsilon/\tau_{\mathrm{e}}$, where ε is the probability of a spin flip occurring at a momentum scattering event. It has been shown that MIs can be treated in a similar manner[100] and through applying Matthiessen's rule an expression for the spin-flip scattering rate in terms of the individual momentum scattering rates and spin-flip probabilities is obtained as:

$$\frac{1}{\tau_{\mathrm{sf}}} = \frac{\varepsilon_{\mathrm{i}}}{\tau_{\mathrm{e}}^{\mathrm{i}}} + \frac{\varepsilon_p}{\tau_{\mathrm{e}}^{\mathrm{p}}} + \frac{\varepsilon_m}{\tau_{\mathrm{e}}^{\mathrm{m}}}, \tag{5.2}$$

where the labels i, p and m represent non-magnetic impurities/defects, phonons and MIs.

The individual momentum relaxation times have been extracted from the charge transport data as discussed previously in Section 5.3.2. Since samples fabricated with six-9s Cu do not show, within the experimental accuracy, a resistivity minimum, $(\tau_{\mathrm{e}}^{\mathrm{m}})^{-1}$ is assumed to be zero. A standard Elliot-Yafet mechanism of spin relaxation through phonon and impurity scattering is used to fit τ_{sf} and reproduces the data well, shown in Fig. 5.6(b). Values for the spin flip probability for phonon and nonmagnetic impurities of $\varepsilon_{\mathrm{p}} = (16.9 \pm 0.5) \times 10^{-4}$ and $\varepsilon_{\mathrm{i}} = (17.2 \pm 0.1) \times 10^{-4}$ respectively are in good agreement with those found in other LSV experiments [19, 101].

The lower purity four-9s τ_{sf} is not reproduced via only phonon and impurity scattering

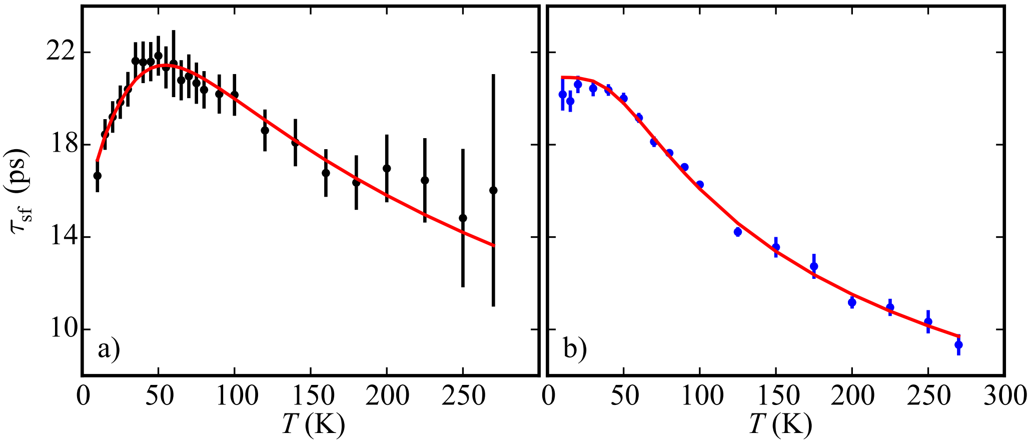

Figure 5.6: Spin flip scattering times for a) four-9s and b) six-9s LSVs. The solid red curves are fits to Equation 5.2. In b) it is assumed that $(\tau_e^m)^{-1} = 0$

but requires the addition of Kondo spin relaxation, which provides excellent agreement with the data as shown in Fig. 5.6 (a). Values for the spin flip probability for phonon and nonmagnetic impurities of $\varepsilon_p = (8.1{\pm}0.5)\times10^{-4}$ and $\varepsilon_i = (13.5{\pm}0.2)\times10^{-4}$ respectively are obtained. The spin flip probability for MIs within Cu is obtained from the fit as $\varepsilon_m = 0.34 \pm 0.03$, a value considerably larger than other contributions from phonons and non-magnetic impurities. This is also an order of magnitude large than estimate for surface spin flip scattering in Ag/Py LSVs[32]. An analytical expression for ε_m can be obtained as [100]:

$$\varepsilon_m = \frac{2}{3}\frac{S(S+1)\left(\frac{J}{V}\right)^2}{1+S(S+1)\left(\frac{J}{V}\right)^2}, \tag{5.3}$$

where S is the spin of the MI, V is the spin-independent scattering potential and J the exchange coupling constant between the impurity and conduction electrons. The exchange coupling constant for Fe impurities in Cu has previously been calculated as $J_{\mathrm{CuFe}} = 0.9{\pm}0.2$ eV [102]. From studies on CuMn dilute alloys a value of $J/V = 0.133$[103] is used with $\mathrm{J}_{\mathrm{CuMn}} = 0.4{\pm}0.1$ eV[102], and maintaining an equal impurity perturbation potential V, provides a ratio $J/V = 0.3 \pm 0.1$ for Fe impurities in Cu. Finally assuming for Fe^{3+} impurities S=5/2, we obtain a value for ε_m of 0.29±0.1 in excellent agreement with the best fit value. It is this large spin-flip probability for MIs which makes them a dominant contribution to λ_{Cu} even at temperatures above which their role is observed in the resistivity. LSVs fabricated with high purity Cu, with no observed Kondo effect, show no downturn within λ_{Cu} at low temperatures, further supporting the role of Kondo scattering in spin relaxation within LSVs.

The small impurity concentration of 4 ppm within the four-9s LSVs demonstrates a significant increase in spin relaxation at low temperatures. However this suppression of λ_{Cu} is also measured in other studies where the Kondo minimum within the resistivity is not reported. To test the generality of this approach the analysis by Villamor *et al.*[19] is repeated with the addition of a magnetic spin relaxation term and using the value $\varepsilon_{\mathrm{m}} = 0.34$. This provides a value for the Kondo resistivity ρ_{K} leading to a MIs concentration of approximately 0.9 ppm through the relationship:

$$\rho_{\mathrm{K}} = c\left(1 + \frac{3zJ}{\epsilon_{\mathrm{F}}}\right)\frac{3\pi mJ^2 S(S+1)}{2ne^2\hbar\epsilon_{\mathrm{F}}}, \tag{5.4}$$

where z is the number of conduction electrons per atom and ϵ_{F} is the Fermi energy taken to be 1 and 7 eV respectively for Cu. This very small amount can clearly be seen as a significant contribution to the spin relaxation but is on the limit of where a Kondo minimum in the resistivity would be observed, with a predicted $T_{\mathrm{min}} \approx 8$ K and below the lowest temperature reported in reference [19].

5.5 Spin Accumulation

When fitting the nonlocal spin signal to obtain λ_{Cu} the effective interface spin polarisation α is a second independent fitting parameter as LSVs were measured with L $\gg \lambda_{\mathrm{Cu}}$. Figure 5.7 (c) shows the obtained values for α as a function of temperature for both four-9s and six-9s samples. The two sample sets show very similar magnitudes and temperature dependence and the values are similar to those calculated for LSVs elsewhere[11, 79]. As the temperature is reduced from 300 K, α increases due to a reduction of magnon population, which cause spin mixing within the Py. However, both show a peak around 70 K and a reduction of the interface polarisation at low temperatures. This has been observed elsewhere and correlated to diffusion of the FM into the NM at the interface with the formation of randomly orientated local moments[11]. Figure 5.7 (a) shows a schematic diagram of this. Due to the shadow deposition technique both the FM and the NM are evaporated within the same vacuum session, then either through diffusion during the deposition or a residual partial pressure of FM material during the initial NM growth, there is a high concentration of FM impurities present at the FM/NM interface. Figure 5.7 (b) shows the spin dependent electro-chemical potential ($\mu_{\sigma}^{\mathrm{s}}$, where $\sigma =\uparrow (\downarrow)$) illustrating the effect of the FM diffusion. Through the Kondo scattering discussed above, λ_s is reduced at the interface compared to the bulk of the NM (i.e. $\lambda_i \ll \lambda_{NM}$) and causes a reduction in the spin accumulation. Since the equation used to fit the data is based on a 1-D model and this reduction in spin accumulation at the interface does not depend on L, and so artificially lowers α.

O'Brien et al.[11] investigated this though LSVs of varying FM/NM combinations using both the spin valve and Hanle effect measurements. Their results reveal that impurity/host combinations that allow the formation of Kondo resonances produce a reduction in α. Crucially this diffusion is a consequence of the fabrication method. Villamor et al.[79] show that a two step fabrication process presents a monotonic temperature dependence in α and such intermixing is only present in LSVs fabricated through shadow deposition.

This provides two regimes that can reduce the spin accumulation within LSVs as indicated in Fig. 5.7 (c). At high temperatures the intrinsic polarisation on the Py is reduced

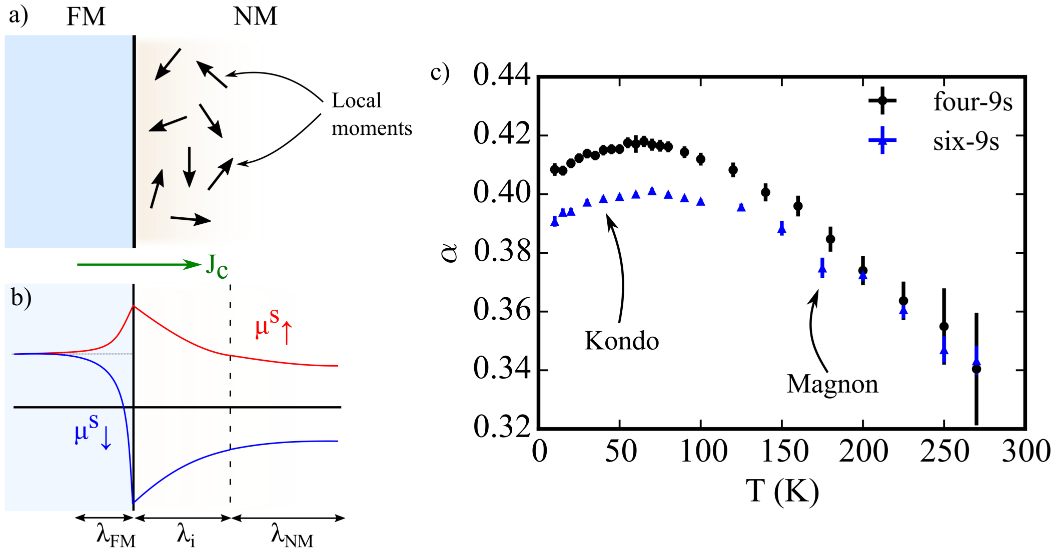

Figure 5.7: a) Schematic of the FM/NM interface at the injector electrode. Small amounts of the FM material diffuses into the NM and can cause the formation of impurities with local moments. This gives rise to Kondo scattering. b) Schematic showing the spin dependent electrochemical potentials at the injector. The gradient due to the charge current has been subtracted for clarity. At the interface where there is a high concentration of MIs the spin diffusion length λ_i will be shorter than in the bulk λ_{NM}. Due to the 1-D model used this alters α. c) α obtained from fits to Eq. 2.3. At high temperatures the reduction is caused my magnon scattering within the FM. However, at low temperatures the Kondo effect in the NM at the interface causes a reduction by dephasing the spin accumulation.

due to spin mixing caused by magnon scattering. At these temperatures (>100 K) α is well reproduced by a Bloch like law:

$$\alpha_{\text{Bloch}} = \alpha_0(1 - (T/T_c)^{3/2}), \tag{5.5}$$

where α_0 is the intrinsic spin polarisation at 0 K and T_c is the Curie temperature of the Py. The fits shown in Fig. 5.8 (a) & (c) give α_0 for the four-9s and six-9s LSVs as 0.431 ± 0.001 and 0.414 ± 0.002 and agree well with values obtained through PCAR[104]. The T_c obtained for four-9s and six-9s were 780 ± 10 and 890 ± 20 K which are reasonably close to measured values[105, 106] but overestimated as the Bloch law breaks down at temperatures close to T_c. At temperatures below this there is a Kondo scattering regime. The transition temperature

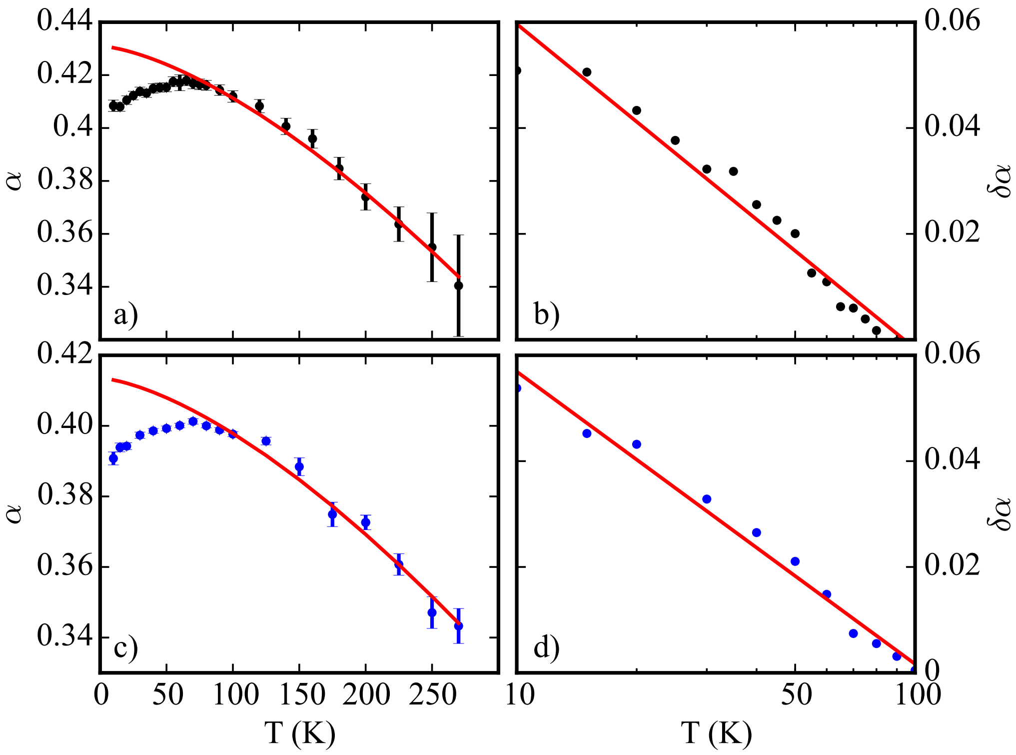

Figure 5.8: a) & c) show the temperature dependence of α for four-9s and six-9s LSVs. The solid red curves are fits to Eq. 5.5 which accurately reproduces the high temperature region. b) & d) are the difference between the best fit values of α and Bloch curves normalised by α_0 ($\delta\alpha = (\alpha - \alpha_{\text{Bloch}})/\alpha_0$) for four-9s and six-9s. These are plotted on a lnT scale and fit very well to a phenomenological Kondo expression.

here is much larger than observed in λ_s due to a higher concentration of MIs[11]. Figure 5.8 (b) & (d) show $\delta\alpha = (\alpha - \alpha_{\text{Bloch}})/\alpha_0$ fitted with a phenomenological Kondo like temperature dependence:

$$\delta\alpha = \delta\alpha_0(1 - \delta\alpha_{\text{K}}\ln\text{T}), \tag{5.6}$$

where $\delta\alpha_{\text{K}}$ is related to the concentration of MIs at the interface. The values for $\delta\alpha_{\text{K}}$ for four-9s and six-9s LSVs are 0.224±0.002 and 0.221±0.002 respectively. These are very similar, indicating that the concentration of MIs diffused into the NM at the interface are not related to the purity of the Cu, as in the previous section, but a consequence of the fabrication. This also confirms that the low temperature decrease in α is again a form of Kondo spin-flip scattering within LSVs.

5.6 Conclusion

The non-monotonic behaviour of the nonlocal spin signal in LSVs has been widely researched and hotly debated for the last decade. The origin of the downturn seen in ΔR_s can vary for different devices and is either due spin-flip scattering in the spacer material or an interface effect. This chapter has shown that both of these effects are a result of Kondo scattering.

From temperature dependent measurements of the resistivity of different purity Cu, the contributions to momentum relaxation from impurities, phonons and the Kondo effect are isolated. This is achieved through fits to a model based upon Matthiessen's rule with Bloch-Grüneisen and Kondo terms to account for phonon and magnetic impurity scattering along with a residual resistivity term. These have been related to the spin relaxation rates through an Elliot-Yafet like model, assuming spin relaxation to be directly proportional to the momentum relaxation. The observed values for spin flip probabilities for phonon and non-magnetic impurities agree with those published for LSVs elsewhere. It has been shown that even extremely small magnetic impurity concentrations can cause a significant reduction in the spin diffusion length at low temperatures due to the large probability of a spin-flip event with Kondo scattering. This type of scattering is orders of magnitude more likely to flip the spin of a conduction electron than any other mechanism. The extension to include MIs accurately reproduces the spin relaxation in this low temperature regime providing a semi-quantitive method for analysis of the effect of MIs on pure spin currents and well describes a common feature seen throughout the literature.

The concept of Kondo spin relaxation is shown to encompass the low temperature region of the spin accumulation in LSVs also. α obtained from fits displays a non-monotonic temperature dependence due to magnon scattering within the FM and Kondo scattering in the NM at the NM/FM interface.

The work in this chapter demonstrates the significant role Kondo spin relaxation plays in LSVs and provides a solution to a long-standing problem within the field.

CHAPTER 6

Kirchhoff’s First Law and Pure Spin Currents

6.1 Introduction

The application of pure spin currents relies heavily on maintaining both spin coherence and a large spin accumulation, as described in the previous chapter. However, an equally important aspect is detailed knowledge of how spin currents behave in multi-terminal circuits. In conventional electronics a fundamental component of circuit design is the principle of fan-out. For example, this allows multiple operations to be performed on information in order to build up complex logical procedures. A fan-out device relies on the condition that electrical currents obey Kirchhoff's laws and in order for spin-logic to be viable, the same must be shown for pure spin currents. Kirchhoff's current law—the sum of currents into a junction being equal to the sum out—occurs due to the conservation of charge, which does not exist in the same way for spins. As a consequence, spin currents decay over the spin diffusion length and in this chapter the application of Kirchhoff's laws to this kind of spin current is tested.

Previous studies have focused on ways to manipulate the spin accumulation at the FM/NM interface. Using double injectors placed at an angle on a single Cu wire, and changing the relative orientation of the magnetisation **M** and the current through each injector, the net quantisation axis of the spin accumulation can accurately be controlled[67]. A similar multi-terminal device fabricated by Nonoguchi *et al.*[107] with fixed **M** direction demonstrates how the effective spin polarisation of the spin accumulation can be modified with combined injector current. However, neither experiment has demonstrated the interaction between two independently produced spin currents, nor how a single spin current divides through a multi-terminal system. Through fabrication of multi-terminal LSVs (MTLSVs) the combination of two spin currents, along with how a single spin current divides through a circuit, is investigated to test the application of Kirchhoff's first law to pure spin currents.

6.2 Experimental Details

6.2.1 Device Geometry

To investigate the behaviour of pure spin currents within a circuit a MTLSV has been fabricated. The device, shown in Fig. 6.1 (a), consists of three Py electrodes all connected by a Y shaped Cu wire. To facilitate clear detection of the spin current within the two arms of the Cu spacer each FM electrode requires a different switching field. As shown in Chapter 4, the reversal of the magnetisation of Py can be controlled though the shape anisotropy of the electrode. Before fabrication the designs for the electrodes were simulated through the micromagnetics software OOMMF. The chosen shapes are shown in Fig. 6.1 (f) where FM1 and FM3 resemble those used for the conventional LSVs. As in previous chapters the highest coercivity electrode is a narrow wire with pointed ends. Figure 6.1 (d) shows the very square hysteresis loop obtained from the simulations with a coercive field much higher than the other electrodes. The very small demagnetising field of this design, due to its large aspect ratio, leads to this high coercivity. However, in real systems, roughness and imperfections can provide nucleation points which reduce the switching field. The large nucleation pad on FM1 has a greater demagnetising field than the thin wires, causing it to reverse its magnetisation more readily. The resulting domain wall at the base of the attached wire then

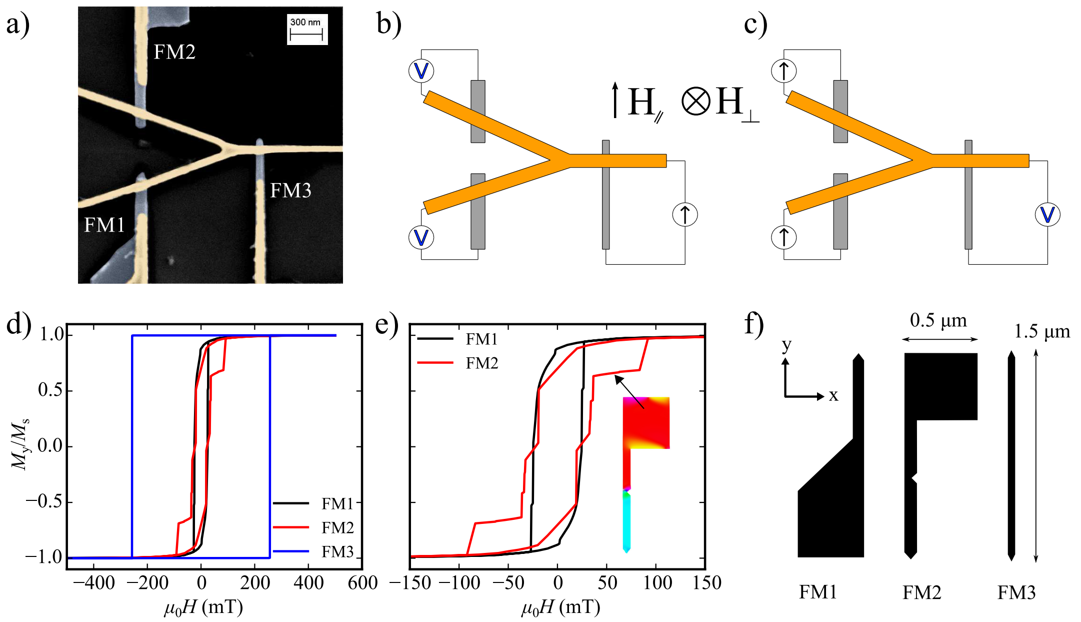

Figure 6.1: a) Scanning electron micrograph of a MTLSV. False colour indicates Cu (orange) and Py (blue). b) and c) show schematics of the fan-out and fan-in experiments. The two field directions are used for spin valve ($H_{\parallel}$) and Hanle ($H_{\perp}$) measurements. d) & e) Results of OOMMF simulations for FM electrodes used for a MTLSV. The field was applied along the y-direction and hysteresis plots display the normalised change in magnetisation along this axis. d) Hysteresis simulations for all three FM electrodes. e) Hysteresis of FM1 and FM2 highlighting difference caused by the addition of a notch. Inset shows the pinned domain wall between the regions of positive (red) and negative (blue) magnetisation along the y-axis. f) Schematic representations of the designs used for the FM electrodes.

propagates along its length. This is observed in the hysteresis simulation as a small kink in the curve at $\mu_0 H = 26$ mT where the wall is pinned at the base of the wire for a short period. The final electrode is similar in design to FM1 but contains a notch along the wire to act as a pinning site of the domain wall, thus increasing the field value where the injection region reverses its magnetisation. The effect of this pinning site is shown in Fig. 6.1 (e) where the magnetisation remains constant over the field range 36–84 mT until the pinning potential is overcome. The use of a notch was preferable over changing the width of the wire in an attempt to maintain equal current densities at FM1 and FM2 interfaces. This provides three Py electrodes with independent switching fields.

6.2.2 Fabrication

The device shown in Fig. 6.1(a) was fabricated using the method outlined in Chapter 3. The complex design of the MTLSV requires extra considerations when planning the shadow lithography and deposition. The Py electrodes were required to be deposited from two angles of ± 40° from the sample normal to obtain the correct overlap with the Cu. FM1 and FM3 were deposited first, followed by FM2, with a thicknesses for all Py electrodes of 20 nm. The wire width for FM1 and FM2 were both 110 nm while FM3 was 65 nm. The width of the Cu wires was reduced to ensure correct shadowing of the substrate where the branches meet and along their length, as they are no longer perpendicular to the Py electrodes. The width of the Cu wire above FM2 (55 ± 5 nm) differed slightly from FM1 (75 ± 5 nm) and FM3 (75 ± 5 nm) due to uneven development. The Cu was deposited last, normal to the sample, with a thickness of 85 nm. The separation between FM1-FM3 and FM2-FM3 was kept the same at 1.18 µm. All measurements of the device geometry have been extracted from SEM images, while thicknesses were taken from the deposition calibrations.

6.2.3 Measurement Geometry

Two different measurement geometries were used to investigate the the application of Kirchhoff's current law to spin currents and are shown in Fig. 6.1 (b) & (c). The fan-out geometry, shown in Fig. 6.1 (b), uses FM3 as the injector electrode with FM1 and FM2 both as simultaneous detectors. This conventional fan-out measurement probes how a pure spin current divides through multiple leads in a circuit. The second configuration, shown in Fig. 6.1 (c), is the reverse, where FM1 and FM2 are injectors and will be called fan-in. The two injectors generate independent spin currents which can be detected at FM3. Both measurements were performed with an in-plane and out-of-plane field to observe the spin valve and spin precession (Hanle) signals. All measurements shown in this chapter were performed at 10 K with the DC injection method described previously.

6.3 Fan-out

6.3.1 Nonlocal Spin Valve Measurements

The in-plane nonlocal spin valve measurements for the fan-out geometry are shown in Fig. 6.2 (a). The detected spin signal at both FM1 and FM2 is shown where the difference in switching fields for these two electrodes is clearly visible. As was noted in Chapter 4, again the magnitudes do not agree with the OOMMF simulations but the correct switching order is obtained.

The magnitudes for the nonlocal spin signal ΔR_s detected at FM1 and FM2 are 641 ± 2 and 414 ± 2 μV/A respectively. The difference in the signals suggests that the spin current generated at FM3 may not separate evenly at the fork and is a consequence of the two channels having different spin resistances. Although the whole Y shaped spacer is made from the same material, the spin resistance depends on the cross sectional area perpendicular to the

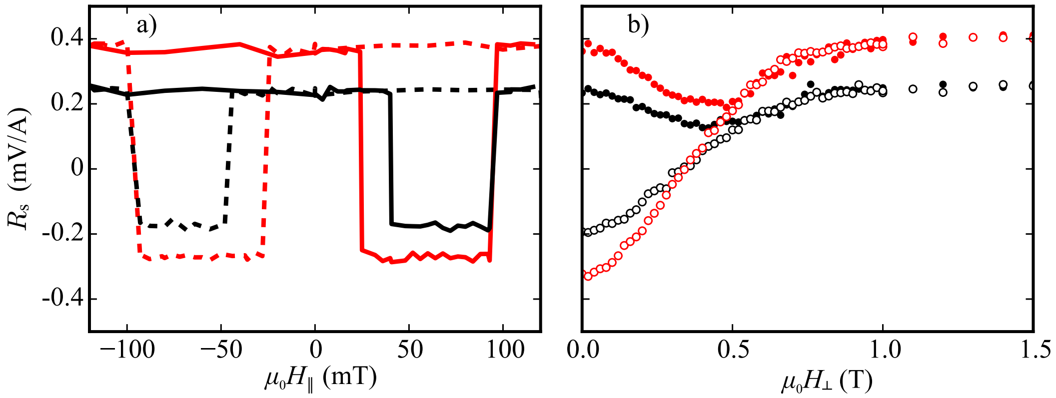

Figure 6.2: Nonlocal spin resistance as a function of applied field for the spin fan-out configuration. Signal detected at FM1 and FM2 and shown in red and black respectively. a) In-plane magnetic field spin valve measurements. Solid and dashed lines are for increasing and decreasing field sweeps. b) out-of-plane Hanle measurements. Solid circles represent all electrodes initially in the P configuration. Open circles for AP initial configuration.

spin flow:

$$R^s_{\mathrm{Cu}} = \frac{\lambda_{\mathrm{Cu}}\rho_{\mathrm{Cu}}}{A_{\mathrm{Cu}}}, \tag{6.1}$$

where λ_{Cu} and ρ_{Cu} are the spin diffusion length and resistivity of the Cu and $\mathrm{A}_{\mathrm{Cu}} = wt$ is the width w multiplied by the thickness t of the Cu wire. Due to small variations in the dimensions, the two branches have different cross sections. The spin resistance is a measure of how quickly a material will equilibrate the spin current and so depends on the spin diffusion length. Since both detectors are the same material the spin injection/detection efficiency $\gamma = (\frac{2\alpha\lambda_{\mathrm{FM}}\rho_{\mathrm{FM}}}{1-\alpha^2})^2$ should be the same for FM1 and FM2 such that it is the spin resistance of the Cu that dictates the separation of the spin current.

6.3.2 Nonlocal Hanle measurements

In order to obtain information about the spin relaxation in the two branches Hanle measurements were carried out in the spin fan-out geometry. The nonlocal spin resistance R_{s} as a function of out-of-plane field for detection at FM1 and FM2 is shown in Fig. 6.2 (b). The Hanle measurements were performed for initial configurations of both P and AP between the detector-injector pairs.

In the Hanle effect the precession of spins due to the out-of-plane applied field ($H_\perp$), coupled with spin relaxation in the Cu is manifest as a damped oscillatory nonlocal signal as shown in Fig 2.4 (d). However, this behaviour is not strongly evident in the data shown in

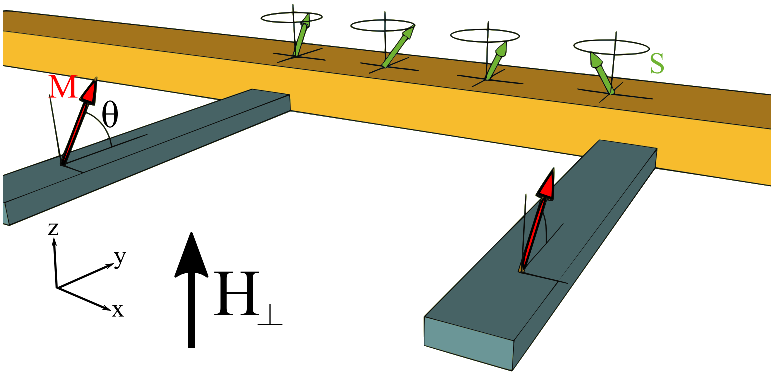

Figure 6.3: Schematic demonstrating the effect of $H_\perp$ on the magnetisation of the FM electrodes and the resulting spin density in the Cu. The applied field causes a rotation of **M** out of the plane by an angle θ altering the quantisation of the injected spin current in the Cu. The spin precess in the x-y plane with an amplitude that reduces to zero as θ tends to 90°.

Fig. 6.2 (b). In fact there is no observation of the π precession angle and both curves quickly tend towards the signal expected of the P configuration. This is caused by an underlying contribution to the arriving spin density from the rotation of the electrodes' magnetisation **M** out-of-plane as shown in Fig. 6.3. As $H_\perp$ increases, **M** begins to rotate out of the plane causing the injected spins to do the same. Although the spins still precess in the x-y plane, their amplitude is reduced and eventually becoming zero once aligned along the z axis when **M** is completely aligned with $H_\perp$.

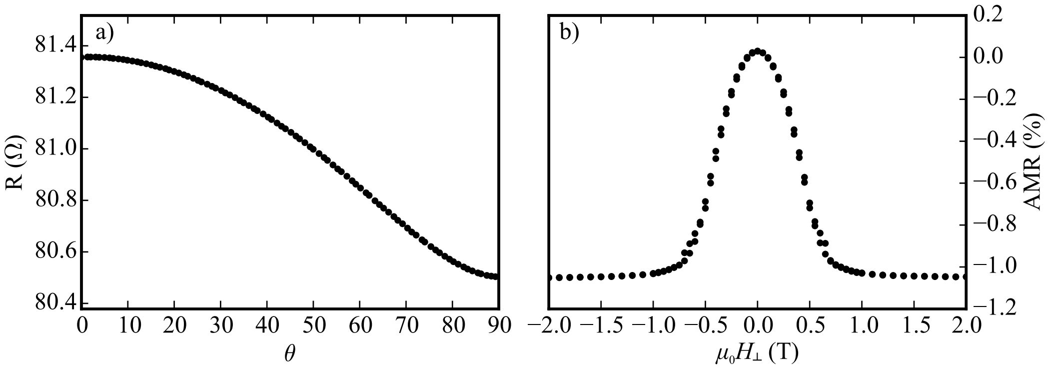

Figure 6.4: Anisotropic magnetoresistance (AMR) for FM1. a) AMR with a 2 T field. The sample is rotated from $\theta = 0°$ (In plane field along the length of the wires) to $\theta = 90°$ (field out-of-plane). b) out-of-plane field sweep. Due to the shape anisotropy, at zero field **M lies along the length of the wire parallel to the current flow. The increasing filed saturated M out of plane and perpendicular to the current flow.**

Figure 6.4 shows the anisotropic magnetoresistance of FM1 highlighting the out-of-plane rotation resulting in limited spin precision. From the Hanle data, R_s for P and AP initial states (R_s^P and R_s^{AP}) begin to collapse onto each other at $\mu_0 H_\perp = 0.5$ T. This corresponds to an out-of-plane rotation of the Py's moment by 70°. The measured signal can be expressed as a convolution of spin precession with the rotation of **M** as[9, 32, 108]:

$$R_H^{P(AP)}(H_\perp,\theta) = \pm R_H^P(H_\perp)\cos^2(\theta) + |R_H(0)|\sin^2(\theta), \tag{6.2}$$

where θ is the angle between substrate plane and the magnetisation vector of the Py and the + and - relate to the P and AP configurations. R_H is the nonlocal Hanle resistance due solely to the spin precession. Using Eq. 6.2 the spin precessional signal can be obtained from the measured data as[32]:

$$R_{\mathrm{H}}^{\mathrm{P}}(H) = |R_{\mathrm{H}}(0)| \frac{R^{\mathrm{P}}(H,\theta) - R^{\mathrm{AP}}(H,\theta)}{2|R_{\mathrm{H}}(0)| - R^{\mathrm{P}}(H,\theta) - R^{\mathrm{AP}}(H,\theta)} \tag{6.3}$$

However, this is only valid below 0.5 T, while the effect due to the rotation of **M** is small, as above this the denominator in Eq. 6.3 tends to zero. The Hanle signal obtained through Eq. 6.3 at FM1 and FM2 is shown in Fig. 6.5. As discussed in Chapter 2 the Hanle data is fitted with the spin-absorption model presented in reference [47]. For consistency it is again assumed that λ_{Py} is 5.5 nm at 10 K[98]. The resistivity of the copper was obtained from resistance measurements on the sample itself, the geometric factors given in Section 6.2.2 and the simple approximation of $\rho = R t_{\mathrm{Cu}} w_{\mathrm{Cu}} / l$. Each path, FM1→FM3 and FM2→FM3, shows a different resistance of 5.451 ± 0.004 and 8.103 ± 0.006 Ω due to the variation in cross-sectional area. With this, the resistivity for each path is calculated as ρ(FM1→FM3) = 2.9 ± 0.2 and ρ(FM2→FM3) = 3.2 ± 0.2 μΩ cm. The difference here is small and within the extremes of the error bounds. Since the Py/Cu interfaces have already been characterised within this work we are able to fix the interface polarisation to a value of $\alpha = 0.39$. This leaves the spin relaxation time τ_{sf} and interface spin mixing conductance $\mathrm{G}^{\uparrow\downarrow}$ left as free fitting parameters.

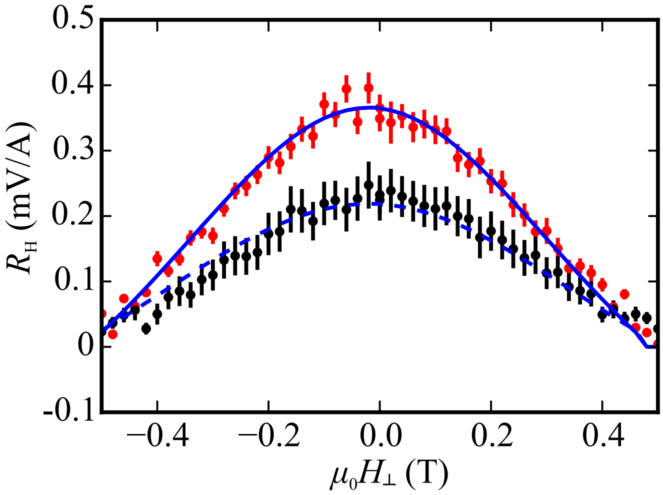

Figure 6.5: Spin precessional Hanle signal obtained from Equation 6.3 for a spin fan-out measurement detected at FM1 (red) and FM2 (black). Blue lines are fits to spin-absorption model in reference [47]

The best fit parameters for τ_{sf} for detecting at FM1 and FM2 are 17.4 ± 0.2 and 11.6 ± 0.3 ps respectively. These values are of similar magnitudes to those observed in conventional LSVs as shown in Chapter 5. The relative difference between the two values is a consequence of the geometry of the forked wire. Assuming a simple Drude approximation, the electronic mean free path λ_e can be estimated through $\lambda_{\mathrm{e}} = \frac{3\pi^2\hbar}{k_{\mathrm{F}}^2 e^2 \rho_{\mathrm{e}}}$ where $k_{\mathrm{F}} = (3\pi^2 n)^{1/3}$ is the Fermi wave vector. Since the dimensions of the wires are similar in magnitude to λ_{e}, approximately 20 nm at this temperature, the discrepancy in τ_{sf} may be caused by scattering off surfaces.The narrower branch of the copper connected to FM2 leads to an increase in surface scattering due to the Fuchs-Sondheimer effect which can increase the spin relaxation rate in the absence of any other dominating factors[86]. Since the Cu used in this experiment was of the 99.9999% (six-9s) purity as was show in Chapter 5 MIs are of sufficiently low density to provide little measurable contribution to spin relaxation. However, the dimensions of the Cu wire here are much smaller and so surface scattering and defects can increase spin relaxation[19]. This in turn can account for the different nonlocal signals from the fan-out measurements, as one channel provides more spin relaxation than the other.

The fits to the data, shown in Fig. 6.5, result in values of the spin mixing conductance for the two electrodes of a very similar magnitude: $\mathrm{G}_{\uparrow\downarrow}(FM1) = (1.65 \pm 0.03) \times 10^{14}\Omega^{-1}\mathrm{m}^{-2}$ and $\mathrm{G}_{\uparrow\downarrow}(FM2) = (1.22 \pm 0.09) \times 10^{14}\Omega^{-1}\mathrm{m}^{-2}$. This is an interesting quantity as it is only observable in these systems when a transverse spin current is present[47] and not measurable in conventional spin valve techniques. These values are in reasonable agreement to the theoretical prediction of the Sharvin conductance of Cu of $\mathrm{G}^{sh} = 4.8 \times 10^{14}\Omega^{-1}\mathrm{m}^{-2}$[47], which has been shown to closely coincide with the value of the spin mixing conductance in intermetallic interfaces[109].

6.4 Fan-in

The other measurement configuration available with this MTLSV is a fan-in, shown in Fig. 6.1 (c). Here two independent current sources perform spin injection at FM1 and FM2 and the resulting nonlocal spin signal is measured at FM3. This enables the investigation of how two independently produced pure spin currents interact with each other for the first time.

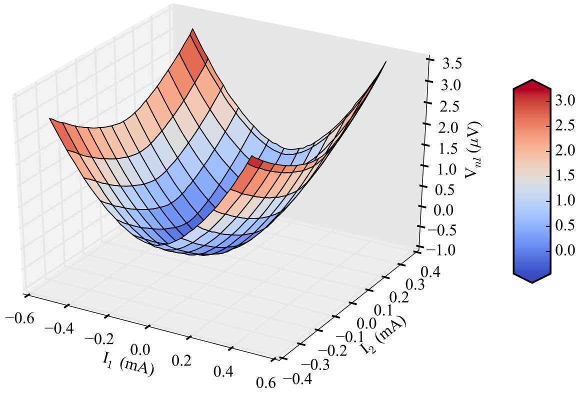

(a)

FM1	FM2	FM3	label
↑	↑	↑	uuu
↑	↑	↓	uud
↑	↓	↓	udd
↓	↓	↓	ddd
↓	↓	↑	ddu
↓	↑	↑	duu
↑	↓	↑	udu

(b)

Figure 6.6: a) Nonlocal voltage at FM3 as a result of spin injection at both FM1 and FM2. Plot forms a paraboloid due to the thermal and spin currents within the MTLSV. b) Table showing the labels assigned to each magnetic configuration of the three electrodes. A final dud state is not shown here as there is no available data for this configuration. However, due to the symmetry this would represent the same measurement values as the udu configuration.

6.4.1 3-dimensional Nonlocal IV

The measurement builds upon the DC spin injection technique used throughout this work. The current injected through FM2 (I_2) is stepped from 0 → 0.4 mA → -0.4 mA → 0, where at each step the current in FM1 (I_1) is swept across a similar range (± 0.5 mA). This produces a 3-dimensional nonlocal current-voltage surface (3DNLIV) as a function of the two injection currents and is repeated across the same field range as the fan-out experiment. Figure 6.6 (a) shows a 3DNLIV plot for the magnetic configuration of all the electrodes parallel to each other. As these injection current maps have been performed over a number of field points, in order to improve the signal to noise ratio, all the field steps that relate to the same configuration (see Fig. 6.6 (b)) are averaged.

The pronounced parabolic shape of the nonlocal voltage in Fig. 6.6 (a) shows that the nonlocal signal is again dominated by Joule heating, as was observed in the NLIVs of conventional LSVs. However, due to the use of two injection electrodes the nonlocal voltage is now a more complex paraboloid function of I_1 and I_2. In order to characterise how the signals from each injector interact with each other the 2^{nd} order polynomial fitting used previously has been extended into a matrix equation. To compare the relative contributions each term makes to the nonlocal signal, the fits were performed with normalised current units such that the matrix elements have units of volts i.e. $i_k = I_k/I_k^{\max}$ for $k = 1, 2$. The fits are then performed with:

$$\begin{pmatrix} 1 \\ i_1 \\ i_1^2 \end{pmatrix} \begin{pmatrix} a_{00} & a_{01} & a_{02} \\ a_{10} & a_{11} & a_{12} \\ a_{20} & a_{21} & a_{22} \end{pmatrix} \begin{pmatrix} 1 & i_2 & i_2^2 \end{pmatrix} = V_{nl} \tag{6.4}$$

Figure 6.7 shows the field dependence of each of the matrix elements. The most significant contribution arises due to the a_{02} and a_{20} terms. These are equivalent to the β terms discussed in conventional LSVs, a consequence of heat flow through the device and detected due to the Seebeck coefficient of Cu and Py. These terms show no dependence on the applied field or magnetic configuration. The udu magnetic state shows a reduction of the value of a_{20} but is a consequence of the device having been taken out of the cryostat and remounted. This may have altered how well the device was thermally anchored to the sample holder or affected the protective resist layer on top of the device. Despite this, it is important to note that the spin signal is not affected. Also, the magnitude of a_{02} and a_{20} are not equal, indicating a larger amount of Joule heating at FM2. This is likely due to the different designs of the two injector electrodes, as FM2 has a longer narrow section compared to FM1, along with a notch in the wire. This results in a higher resistance along the

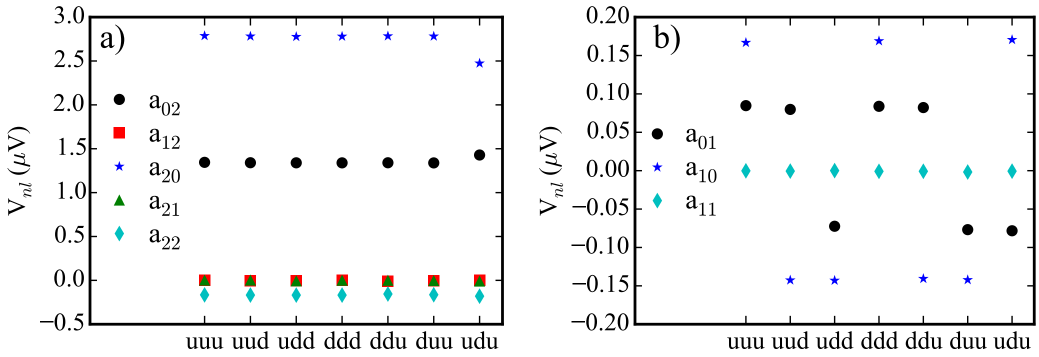

Figure 6.7: Results from fitting Eq. 6.4 to 3DNLIV of different magnetic configurations. a) Show the matrix elements for all terms involving either I_1^2 or I_2^2. b) Terms that only have linear contributions. Only a_{10} and a_{01} show any dependence on the magnetic configuration as they depend on whether the detector/injector pair are P or AP.

current path of FM2, close to to the Cu spacer, increasing the thermal current as a result of Joule heating. It is interesting to note that the a_{22} term shows a small, yet still significant, contribution to the nonlocal voltage that is not present in conventional lateral spin valves. This is a second order effect due to the combination of the two heat currents generated by each injector. The observed voltage is negative, indicating a reduction in the efficiency of detecting the quadratic terms as they increase in magnitude. From Fig. 4.7 it can be seen that below 50 K a_{02} and a_{20} will have a negative temperature coefficient which accounts for the sign of a_{22}. The a_{00} term is also fairly large (≈ 1 µV and not shown) but again has no dependence on the magnetic configuration of the electrodes. This term is a voltage offset within the experimental apparatus similar to the constant term for conventional LSVs and can be ignored.

The a_{12} and a_{21} terms are zero for all magnetic configurations within the uncertainty of the fit. These demonstrate that there is no interaction between the spin current and heat current at the level of current densities used in this study. Fits were performed up to order 3 in the current but all extra terms were found to be zero within the uncertainty of the fit. This shows that the current densities used here are not high enough to generate spin currents through thermal effects[22, 23].

The a_{01} and a_{10} terms represent the spin current from each electrode and are shown in Fig. 6.7 (b). As seen in conventional LSV measurements only the linear in current terms show a field dependence which can be attributed to the charge injected spin current. The absolute magnitude of the coefficients is the same for all configurations but the sign changes depending on the relative orientation of the injector electrodes magnetisation with respect to the detector. The average absolute value for a_{01} and a_{10} divided by the maximum current are $R_{01} = 203 \pm 4$ and $R_{10} = 320 \pm 10$ µV/A. Since at this temperature $\Delta R_s \approx 2R_s$ (see Fig. 4.9 (a)) these values coincide with the magnitude of ΔR_s found in the fan-out geometry. This demonstrates the ability to isolate each individual spin current from its dependence on the injected charge current at its source. It is also found that the a_{11} term is zero for all magnetic states, shown in Fig. 6.7 (b). This is to be expected if spin currents obey Kirchhoff's law, as there is no non-linear interaction between the two spin currents.

To gain further insight into how the total spin signal behaves in a MTLSV we focus on only the linear component of the 3DNLIV maps shown in Fig. 6.8. The field independent background is obtained by taking the average of the uuu and udd configurations. Since making the transition from uuu to udd both injectors reverse their magnetisation with respect

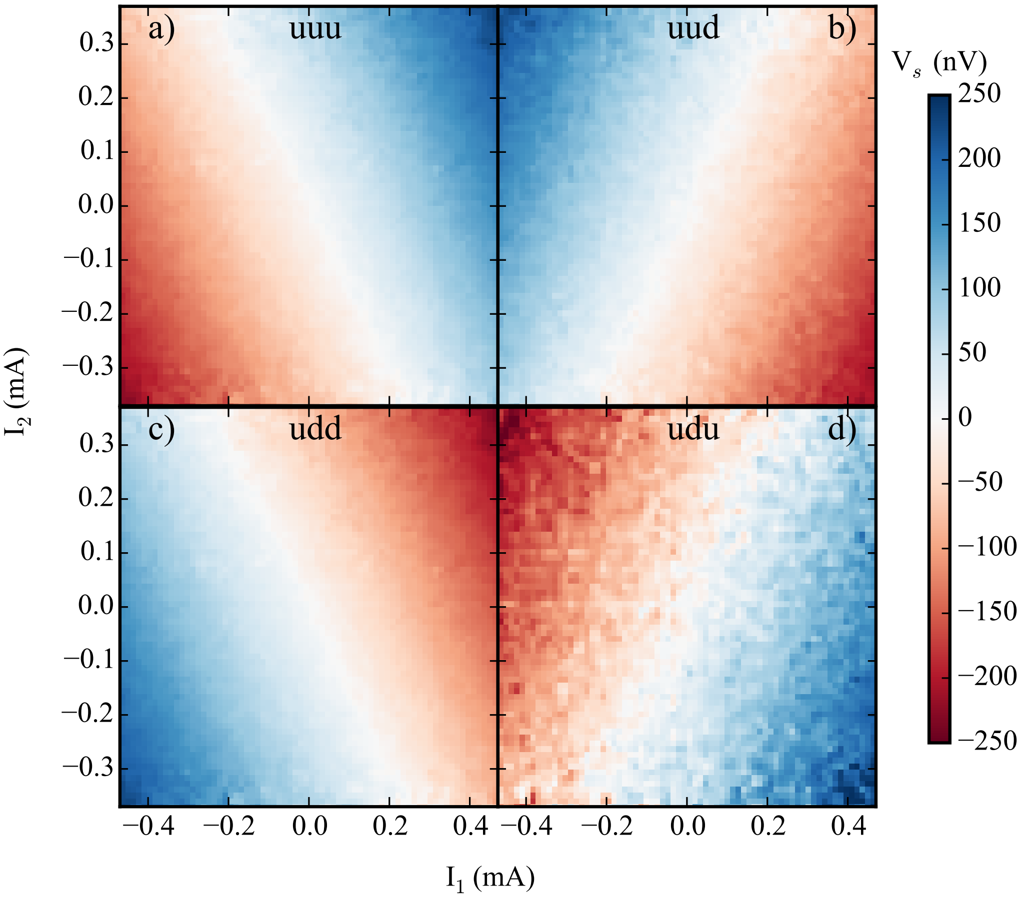

Figure 6.8: Magnitude of the nonlocal spin voltage detected at FM3 as a function of the injection currents through FM1 (I_1) and FM2 (I_2) for various magnetic configurations.

to the detector the spin signal is averaged out. This is then subtracted from each 3DNLIV to obtain the field dependent voltage. The resulting nonlocal spin voltage (V_s) varies linearly with current as similarly seen in Chapter 4. The striking result for the fan-in geometry is the clear region where the spin voltage at the detector is zero for finite injection currents. Figure 6.8 (a) shows the case for all electrodes parallel to each other. Here we can see that zero spin voltage is detected for a negative ratio of injection currents, demonstrating that one injector can be used to cancel the spin current produced at the other. By thresholding V_s around the zero region and fitting a straight line, a ratio of injection current of -1.52 ± 0.04 is obtained. The minus sign here originates from the parallel orientation of injection electrodes, whereby opposite sign injection currents are required to cancel out the spin accumulation

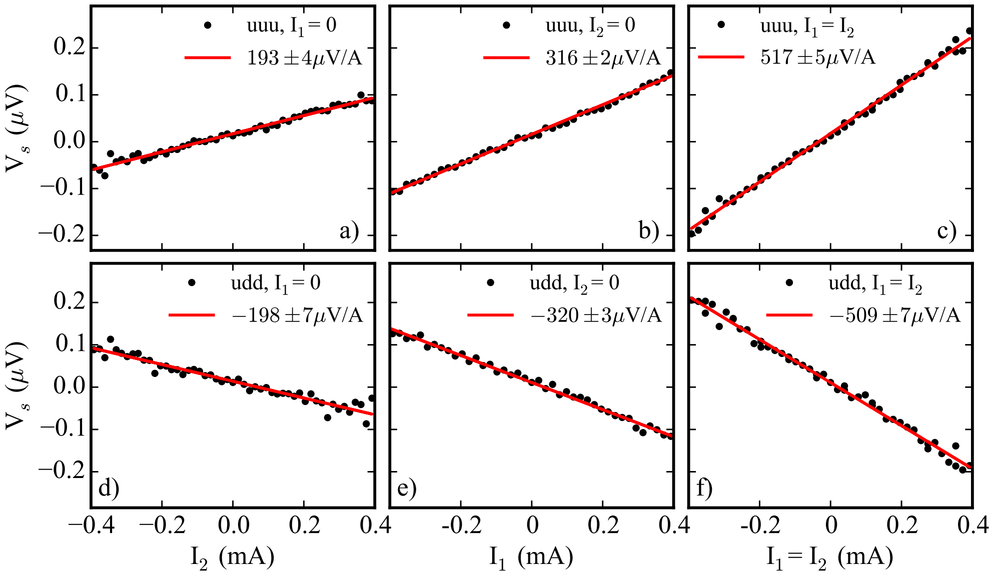

Figure 6.9: Sections cut through the 3DNLIV for the magnetic configurations uuu (a-c) and udd (d-f). a) & d) are sections along the line $I_1 = 0$. c) & e) are sections along the line $I_2 = 0$. c) and f) are sections along the line $I_1 = I_2$

at FM3. The absolute magnitude of this matches very well to the ratio of nonlocal spin signals $R_{01}/R_{10} = 1.58 \pm 0.03$ acquired from fitting the individual current characteristics and demonstrates the linear combination of the spin signals from the two injectors. By changing the relative orientation of an injector electrode we can observe the symmetry of the spin injection. Figure 6.8 (d) has switched the direction of FM2 with respect to the other two electrodes, uuu → udu. This has the effect of causing the opposite spin type to be injected for the same direction of current. This shows that the sign of the spin current can be controlled either through the orientation of the FM electrode or the direction of the current. Although it has been shown that reversing the sign of the injection current changes the orientation of the injected spins[13] this is the first example of two spin currents completely cancelling each other out.

Figure 6.9 is a series of sections cut through the V_s maps of Fig. 6.8. Figure 6.9 (a) & (d) are cut along the line $I_1 = 0$ for the uuu and udd configurations with a linear fit to the data. This provides another method of obtaining R_{01} and results in the same value as fitting the 3DNLIV. This is also achieved for sections along the $I_2 = 0$ and gives the same result for

R_{10} as above. Importantly, if we section the spin voltage along the line of equal injection currents, as shown in Fig. 6.9 (c) & (f), it can be seen that the spin voltages add linearly i.e. for uuu $R_s(I_1 = 0) + R_s(I_2 = 0) = 193 \pm 4$ μV/A $+316 \pm 2$ μV/A $= 509 \pm 5$ μV/A and is within the extremes of the error bounds of $R_s(I_1 = I_2) = 517 \pm 5$ μV/A. This is as would be expected through Kirchhoff's law. An effective ΔR_s for the fan-in geometry can be defined by R_s(uuu) - R_s(udd) $= 1.026 \pm 9$ mV/A and is equivalent to the sum of the ΔR_s observed individually from FM1 and FM2 in the fan-out geometry.

Kirchhoff's current rule states that the sum of currents into a junction must equal the sum of currents out of a junction, and so currents will add and subtract linearly. The results above appear to confirm this for pure spin currents as it has been shown that the nonlocal spin signal from two independent injectors will add and subtract linearly. However, nonlocal measurements are only sensitive to changes in the electrochemical potential and do not directly measure the spin current. In order to obtain information about this a finite element method was used to solve Eq. 2.10 for an ideal MTLSV and the results are shown in Fig. 6.10. Figure 6.10 (a) shows the electrochemical potential within a MTLSV for the fan-in geometry when $I_1 = 0$ and $I_2 = 500$ μA. When comparing this to the the P configuration shown in Fig. 6.10 (b) ($I_1 = I_2 = 500$ μA) we observe, as expected from the experimental results, twice the value of the spin accumulation at the detector. Similarly, in the AP configuration FM1 and FM2 inject opposite spin types and form negative and positive spin accumulations in each Cu branch respectively. The spin accumulation then cancels out when the branches meet as observed in the experimental data.

However, the calculated spin currents for the two cases begin to show a deviation from Kirchhoff's laws. For the single injection fan-in case shown in Fig. (g) the spin current is shown to diffuse in all directions. If the magnitude of the normalised spin currents on either side of the junction (the highlighted green region) are summed then they are not found to be equal. On the left hand side values of J_s/J_c are 5.8×10^{-3} and -1.1×10^{-3} in the upper and lower wires respectively. However, at the right hand side of the junction $J_s/J_c = 3.2 \times 10^{-3}$ and so Kirchhoff's current law is not obeyed. This is result of the finite volume of the junction where the central region becomes much wider than the individual wires. This provides a larger volume where spin relaxation events can occur, causing a decay in the magnitude of the pure spin current within the junction region. The same is observed in Fig. 6.10 (e) for the P configuration and Fig. 6.10 (f). Yet, in Fig. 6.10 (e) the AP dual injection configuration is a special case, as the spin accumulation cancels on the right hand side of the junction and the spin currents on the left are of equal and opposite magnitude they do obey Kirchhoff's law. Finally, although the pure spin currents do not obey Kirchhoff's current law exactly, it is worth pointing out that the resulting spin current at the detector for the dual injection is twice that of a single injection. This shows that the pure spin currents generated independently by each injector do add up linearly in the same manner as the spin accumulations.

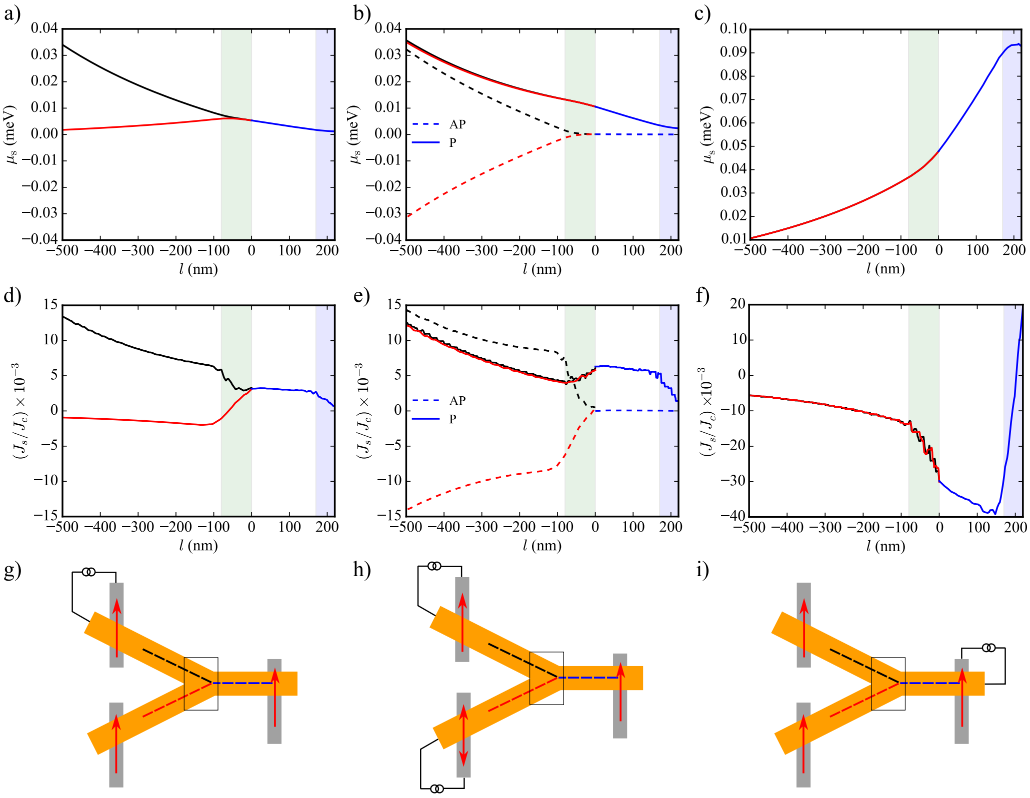

Figure 6.10: Results for finite element simulations solving Eq. 2.10 for the MTLSV geometry. An ideal case was chosen where the spin diffusion and geometric parameters for each Cu branch are the same to simplify the problem. a), b) and c) show the spin accumulation ($\mu_s = \mu_\uparrow - \mu\downarrow$) while d), e) and f) show the spin current normalised to the charge injection current. Below in g), h) and i) are schematics of the MTLSV for three different injection regimes. The black, red and blue lines indicate the paths along which the above results have been taken. The black box corresponds to the green shaded region in the above. a), d) and g) show results for a single spin injection, while b), e) and h) are for dual spin injection in the fan-in configuration. The solid and dotted lines in b) and e) correspond to the P and AP alignment of FM1 and FM2. c), f) and i) show the fan-out geometry.

6.4.2 Spin Coherence

Hanle measurements were also performed in the fan-in geometry. Here a single current source was used for injection at both FM1 and FM2 fixing the injection current to always be equal for both. This will make the two injectors sit at slightly different potentials and causes a small leakage current through the device. This is observed as an extra linear component in the NLIV but does not affect the magnitude of the spin current and has been subtracted. The measurements were performed by setting the magnetic configuration in plane then performing NLIV sweeps at each out-of-plane field steps. The spin signal is then obtained by fitting a quadratic and extracting the linear component as shown previously.

Figure 6.11 (a) shows the measured signal for the initial magnetic configurations of all parallel and both injectors antiparallel to the detector. These curves show qualitatively the same behaviour as each individual detector in the fan-out Hanle measurements but with increased magnitudes. Figure 6.11 (b) shows the difference between these two curves. For comparison, the difference between the P and AP initial configurations of the fan-out measurement with FM1 and FM2 as detectors have been added together and plotted on top. We see that the two curves lie closely on top of each other and demonstrates the equivalence of the spin valve and Hanle measurements, further confirming that the two spin currents add following Kirchhoff's law.

Figure 6.11 also shows data where the polarity of the current injected into FM2 has been reversed with respect to FM1. This reversal of the injection current's polarity in FM2 with respect to FM1 causes an accumulation of the opposite sign spins, having an effective phase shift of π upon injection into the Cu. Interestingly this curve shows no field dependence. This is because the FM2 electrode is effectively tending towards the AP state with respect to the detector as **M** of the electrodes is pulled out of the plane, while FM1 tends towards P. The lack of any field dependence highlights that the spin currents in each branch of the Cu under go Lamour precession at the same frequency and maintain their π phase difference.

6.5 Conclusion

In this chapter the application of Kirchhoff's first law to pure spin currents has been tested through measurements on a MTLSV. Both fan-out and fan-in experiments have been performed to observe how spin currents behave in a multi-terminal circuit. The fan-out geometry demonstrates that the spin current will divide between the different branches in a

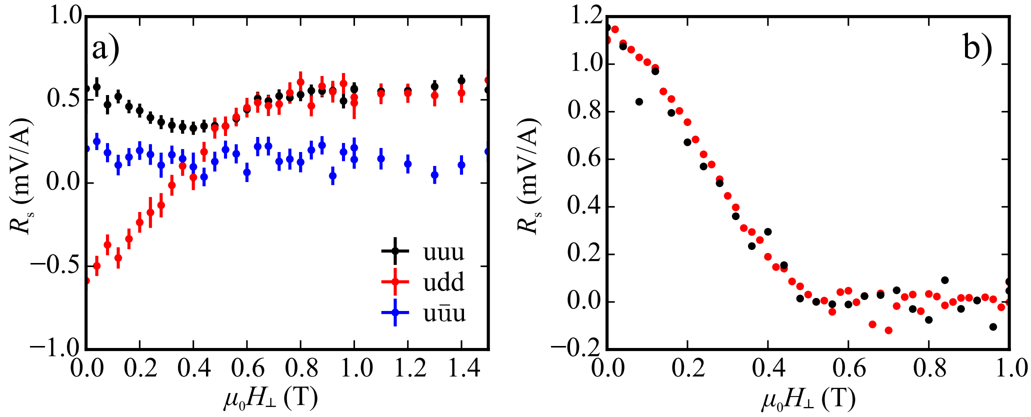

Figure 6.11: a) Nonlocal Hanle data for spin injection at both FM1 and FM2 simultaneously. uuu and udd are for initial states of the injectors parallel of antiparallel to the detector. uūu is for the initial configuration of all electrodes parallel but with the polarity of the injection current reversed for FM2 with respect to FM1. b) Black data are $\Delta R_S = R_S(\text{uuu}) - R_S(\text{udd})$ for the fan-in Hanle measurements. Red data are the sum of $\Delta R_s = R_s^P - R_s^{AP}$ detected at FM1 and FM2 for the fan-out geometry. The precise overlay of these two curves is further evidence for spin currents obeying Kirchoff's law.

circuit, with a magnitude determined through the spin resistances of each arm. Through Hanle measurements the spin relaxation time τ_{sf} for detecting at FM1 and FM2 is measured to be 17.4 ± 0.2 and 11.6 ± 0.3 ps respectively. Since this device was fabricated from high purity Cu the differences in spin relaxation is a consequence of the reduced cross-sectional area of one branch causing an increase in surface scattering due to the Fuchs-Sondhiemer effect. As the spin resistance of a material depends on how effectively it will relax an accumulation of spins, this causes the unequal separation of the spin current.

The fan-in measurements demonstrate that two pure spin currents will add and subtract with each other. The development of a 3DNLIV and matrix fitting method provides information about each spin current, along with the thermal current generated at the injection point, and how they interact with each other. We see here that the spin currents show no non-linear effect and no interaction with the heat flow at the current densities used in this study. The spin accumulations add together and the same magnitude is observed for both fan-in and fan-out experiments. We also see that by changing the sign of one spin current, either through reversing the polarity of the injection current or direction of the magnetisation of the FM, the two pure spin currents can cancel each other out. Through finite element simulations a pure spin current is shown to not exactly fulfil Kirchhoff's current law due to spin relaxation within the finite size of the junction. However, the resulting spin current at the detector is shown to be a sum of the individual spin currents generated at each injector.

These experiments have demonstrated the symmetry of pure spin currents with respect to the injection current and shown spin currents add and subtract within a multi-terminal device.

CHAPTER 7

Conclusions

Lateral spin valves are an effective tool in the study of spin transport and due to this have seen a large amount of interest in the past 15 years, with the publication of almost 300 studies covering multiple material systems. This thesis aimed to answer two fundamental questions regarding the properties of pure spin currents in these structures: what causes the loss of spin coherence at low temperatures? and how do pure spin currents interact? Here the important steps leading to, and the results obtained in answering, these questions are summarised.

7.1 Conclusion

In order to answer the important questions proposed it was first crucial to develop a method of fabricating high quality LSVs. To this end, a large amount of effort was expended within this work on the building of a bespoke UHV deposition system and development of a double-dose lithography recipe, the details of which are presented in Chapter 3. The combination of these provided the means to fabricate multi-material lateral structures without breaking vacuum. Through measurements of the interface resistance and nonlocal spin signals presented in this work, this method of fabrication has been shown to yield high quality LSVs. The direct observation of a negative interface resistance, shown in Chapter 4, is only possible with low resistance contacts and the combination of measurements and simulations performed here show that the fabricated device are within the transparent limit. Along side this Chapters 5 and 6 show nonlocal measurements where the observed spin signals are comparable to those throughout the literature for Cu/Py LSVs of similar dimensions. Consequently, these key results show the fabrication methods developed for this thesis enable high quality lateral structures to be produced and provide the first LSVs made through these means at Leeds and in the UK. Secondly it is of critical importance to the study of spin transport to enable the clear isolation of signal that result from this and not other effects. In this work a DC injection method was used, where the full current-voltage characteristics were examined at each field step. This method allows the observation of thermal and spin transport without the need for multiple lock-in amplifiers and measurements of the current and field dependence enables the isolation of the spin transport signal.

Of principal importance to the conclusions made in this thesis were the results concerning the loss of spin accumulation at low temperatures. This has been a long-standing problem within the field, where different models have been suggested with little success in describing the contradictory results published. Chapter 5 presented charge and spin transport data on LSVs fabricated from two different purities of Cu, 99.99% (four-9s) and 99.9999% (six-9s). The resistance as a function of temperature of the two materials exhibits a Kondo effect only in the four-9s Cu and can be directly correlated to an decrease in λ_{Cu} at low temperatures, which is not present in the higher purity six-9s Cu. This provides direct evidence that magnetic impurities, either in the bulk of the NM spacer or on the surface, can cause the loss of spin accumulation at low temperatures seen in many experiments. A quantitative approach is achieved thorough applying Matthiessen's rule along with an Elliot-Yafet model of spin relaxation and the individual contributions from phonon, non-magnetic impurities and defects, and Kondo scattering were obtained. The value for the probability of a magnetic impurity causing a conduction electron to flip its spin was found to be $34 \pm 3\%$ and is shown to be orders of magnitude larger than any other mechanism. The effect of Kondo spin relaxation is demonstrated to encompass the low temperature region of the spin accumulation at FM/NM interfaces, as α obtained from fits also displays a non-monotonic temperature dependence. This establishes the dominant role Kondo scattering can play in spin relaxation in LSVs, yielding a solution to this long-standing problem and is a key conclusion of this thesis.

Finally, Chapter 6 establishes that pure spin currents do not fully obey Kirchhoff's first law. Both fan-out and fan-in experiments were performed investigating how spin currents behave in a multi-terminal circuit. The fan-out geometry demonstrates that the spin current will divide between different branches in a circuit, with a magnitude determined through the spin resistances of each arm. The fan-in measurements, through development of a 3DNLIV and matrix fitting method, demonstrate that two pure spin currents add and subtract with each other in a linear manner. The subtraction of two spin current is shown through the injection of the opposite spin type at one electrode, either through reversing the polarity of the charge current or direction of the magnetisation of the FM, and shows that two spin currents can cancel each other out. However, simulations demonstrate that the sum of the spin currents into a junction is not equal to the sum out, as pure spin currents are not conserved due to spin relaxation within the finite volume of the junction, and so do not fulfil Kirchhoff's first law.

This thesis has demonstrated a robust and reliable method for the fabrication of high quality LSVs through a double-dose lithography and angle deposition technique. A DC NLIV measurement method has been presented, where by the individual contributions to the nonlocal signal from thermal and spin dependent effect have been successfully isolated.

With this, the different spin relaxation mechanisms within the LSV are quantified, showing the dominant role Kondo scattering plays and solving the issue of high spin relaxation at low temperatures. Finally, measurements demonstrate how pure spin currents behave in multi-terminal devices and provide the basis of spin current circuits for computation.

7.2 Outlook

Crucially, this thesis has seen the development of a method for fabricating lateral structures with good quality interfaces. This opens up a wide range of research possibilities both in spintronics and other fields, such as superconductivity. Immediately, within the field of spintronics, the development of the MTLSV provides the greatest research impact as it is a building block for spin current based logic. However, in order to achieve this two fundamental obstacles must be overcome; spin amplification and logical operations with spin currents. The first has been a hard sought goal of spintronics for decades and is perhaps better suited to semiconducting materials. The latter however, could be attained by building on the work in this thesis.

By building LSVs which contain loop structures in the NM spacer it would be interesting to see how a pure spin current interacts with itself. The possibility for logic operations may then be realised through applications of the Hanle effect. By applying a perpendicular field of sufficient strength a spin current can be forced to reverse its quantisation axis, providing a similar operation to the conventional logic 1 → 0. Using Oersted lines close to each side of the loop perpendicular fields can be applied to each half independently, altering the spin current in each one and changing the resulting combination. Ultimately, spin logic becomes more complicated than conventional charge systems and would be more suitable to ternary logic with values of ↑, ↓ and 0 representing the two different spin current orientations and no spin current. The above device could be considered the equivalent of an inverter, providing one of the two alternative outputs depending on whether one or both Oersted lines are used. Further development along this line of research would be very interesting and provide possible applications for spin based logic systems.

REFERENCES

[1] W. Thomson, On the Electro-Dynamic Qualities of Metals:–Effects of Magnetization on the Electric Conductivity of Nickel and of Iron, *Proc. R. Soc. London* **8**, 546 (1856) 2, 9

[2] G. Binasch, P. Grünberg, F. Saurenbach and W. Zinn, Enhanced magnetoresistance in layered magnetic structures with antiferromagnetic interlayer exchange, *Phys. Rev. B* **39**, 4828 (1989) 2

[3] M. N. Baibich, J. M. Broto, A. Fert, F. N. Vandau, F. Petroff et al., Giant Magnetoresistance of Fe-Cr Magnetic Superlattices, *Phys. Rev. Lett.* **61**, 2472 (1988) 2

[4] D. E. Nikonov, G. I. Bourianoff and P. a. Gargini, Power dissipation in spintronic devices out of thermodynamic equilibrium, *J. Supercond. Nov. Magn.* **19**, 497 (2006) 2, 61

[5] B. Behin-Aein, D. Datta, S. Salahuddin and S. Datta, Proposal for an all-spin logic device with built-in memory., *Nat. Nanotechnol.* **5**, 266 (2010)

[6] S. Bader and S. Parkin, Spintronics, *Annu. Rev. Condens. Matter Phys.* **1**, 71 (2010) 2, 61

[7] T. Valet and A. Fert, Theory of the Perpendicular Magnetoresistance in Magnetic Multilayers, *Phys. Rev. B* **48**, 7099 (1993) 2, 3, 8, 10, 49, 51

[8] M. Johnson and R. H. Silsbee, Interfacial charge-spin coupling: Injection and detection of spin magnetization in metals, *Phys. Rev. Lett.* **55**, 1790 (1985) 2

[9] F. J. Jedema, H. B. Heersche, A. T. Filip, J. J. A. Baselmans and B. J. van Wees, Elec-

trical detection of spin precession in a metallic mesoscopic spin valve, *Nature* **416**, 713 (2002) 2, 49, 83

[10] F. J. Jedema, A. T. Filip and B. J. van Wees, Electrical spin injection and accumulation at room temperature in an all-metal mesoscopic spin valve, *Nature* **410**, 345 (2001) 2, 69

[11] L. O'Brien, M. J. Erickson, D. Spivak, H. Ambaye, R. J. Goyette et al., Kondo physics in non-local metallic spin transport devices, *Nat. Commun.* **5**, 3927 (2014) 2, 3, 44, 46, 49, 58, 61, 72, 73, 75

[12] T. Kimura and Y. Otani, Large spin accumulation in a permalloy-silver lateral spin valve, *Phys. Rev. Lett.* **99**, 196604 (2007) 2, 49

[13] F. Casanova, A. Sharoni, M. Erekhinsky and I. K. Schuller, Control of spin injection by direct current in lateral spin valves, *Phys. Rev. B* **79**, 184415 (2009) 2, 3, 44, 46, 49, 51, 58, 69, 90

[14] G. Salis, A. Fuhrer, R. R. Schlittler, L. Gross and S. F. Alvarado, Temperature dependence of the nonlocal voltage in an Fe/GaAs electrical spin-injection device, *Phys. Rev. B* **81**, 23 (2010) 2

[15] T. Suzuki, T. Sasaki, T. Oikawa, M. Shiraishi, Y. Suzuki et al., Room-temperature electron spin transport in a highly doped Si channel, *Appl. Phys. Express* **4**, 2 (2011) 2

[16] T. Wakamura, N. Hasegawa, K. Ohnishi, Y. Niimi and Y. Otani, Spin injection into a superconductor with strong spin-orbit coupling, *Phys. Rev. Lett.* **112**, 36602 (2014) 2

[17] T. Wakamura, H. Akaike, Y. Omori, Y. Niimi, S. Takahashi et al., Quasiparticle-mediated spin Hall effect in a superconductor, *Nat. Mater.* **14**, 675 (2015) 2

[18] G. Mihajlović, D. K. Schreiber, Y. Liu, J. E. Pearson, S. D. Bader et al., Enhanced spin signals due to native oxide formation in Ni80 Fe20 /Ag lateral spin valves, *Appl. Phys. Lett.* **97**, 2010 (2010) 2

[19] E. Villamor, M. Isasa, L. E. Hueso and F. Casanova, Contribution of defects to the spin relaxation in copper nanowires, *Phys. Rev. B* **87**, 94417 (2013) 3, 46, 61, 63, 69, 70, 72, 85

[20] X. J. Wang, H. Zou and Y. Ji, Increase of nonlocal spin signal at high dc bias due to a redistribution of the injection current, *Phys. Rev. B* **81**, 104409 (2010) 2

[21] S. R. Bakaul, S. Hu and T. Kimura, Thermal gradient driven enhancement of pure spin current at room temperature in nonlocal spin transport devices, *Phys. Rev. B* **88**, 2 (2013) 2, 54

[22] M. Erekhinsky, F. Casanova, I. K. Schuller and A. Sharoni, Spin-dependent Seebeck effect in non-local spin valve devices, *Appl. Phys. Lett.* **100** (2012) 58, 88

[23] A. Slachter, F. L. Bakker, J.-P. Adam and B. J. van Wees, Thermally driven spin injection from a ferromagnet into a non-magnetic metal, *Nat. Phys.* **6**, 879 (2010) 2, 54, 88

[24] N. Kuhlmann, C. Swoboda, A. Vogel, T. Matsuyama and G. Meier, All-metal lateral spin valve operated by spin pumping, *Phys. Rev. B* **87**, 104409 (2013) 2

[25] T. Kimura, T. Sato and Y. Otani, Temperature evolution of spin relaxation in a NiFe/Cu lateral spin valve, *Phys. Rev. Lett.* **100**, 66602 (2008) 3, 61, 69, 70

[26] L. Wang, Y. Fukuma, H. Idzuchi, G. Yu, Y. Jiang et al., Effect of annealing on interfacial spin polarization and resistance in permalloy/MgO/Ag lateral spin valves, *Appl. Phys. Express* **4**, 093004 (2011) 3

[27] Y. Fukuma, L. Wang, H. Idzuchi and Y. Otani, Enhanced spin accumulation obtained by inserting low-resistance MgO interface in metallic lateral spin valves, *Appl. Phys. Lett.* **97**, 2013 (2010) 3

[28] S. Takahashi and S. Maekawa, Spin current, spin accumulation and spin Hall effect, *Sci. Technol. Adv. Mater.* **9**, 014105 (2008) 3, 10, 11, 14, 43, 49, 51

[29] R. J. Elliott, Theory of the effect of spin-Orbit coupling on magnetic resonance in some semiconductors, *Phys. Rev.* **96**, 266 (1954) 3, 17, 61, 70

[30] Y. Yafet, Conduction-electron spin relaxation by transition-element impurities in copper, *J. Appl. Phys.* **39**, 853 (1968) 3, 17, 18, 61, 70

[31] H. Zou and Y. Ji, The origin of high surface spin-flip rate in metallic nonlocal spin valves, *Appl. Phys. Lett.* **101**, 82401 (2012) 3, 61, 62, 69, 70

[32] G. Mihajlović, J. E. Pearson, S. D. Bader and A. Hoffmann, Surface spin flip probability of mesoscopic Ag wires, *Phys. Rev. Lett.* **104**, 1 (2010) 3, 61, 62, 70, 71, 83, 84

[33] J. Kondo, Resistance Minimum in Dilute Magnetic Alloys, *Prog. Theor. Phys.* **32**, 37 (1964) 3, 18, 20, 66, 67

[34] J. S. Dugdale, *The Electrical Porperties of Metals and Alloys*, Edward Arnold Ltd (1977) 6

[35] N. F. Mott, The electrical conductivity of transition metals, *Proc. R. Soc. London. Ser. A* **153**, 699 (1936) 6

[36] S. Maekawa, S. O. Valenzuela, E. Saitoh and T. Kimura, *Spin Current*, Oxford University Press (2012) 6, 10

[37] I. Žutić, J. Fabian and S. D. Sarma, Spintronics: Fundamentals and applications, *Rev. Mod. Phys.* **76**, 323 (2004) 6

[38] E. C. Stoner, Collective electron ferromagnetism, *Proc. R. Soc. London A* **165**, 372 (1937) 7

[39] J. M. D. Coey, *Magnetism and Magnetic Materials*, Cambridge University Press (2010) 8

[40] S. Oki, S. Yamada, N. Hashimoto, M. Miyao, T. Kimura et al., Effect of addition of al to single-crystalline CoFe electrodes on nonlocal spin signals in lateral spin-valve devices, *Appl. Phys. Express* **5**, 063004 (2012) 7

[41] N. F. Mott, Electrons in transition metals, *Adv. Phys.* **13**, 325 (1964) 8

[42] I. A. Campbell, A. Fert and A. R. Pomeroy, Evidence for Two Current Conduction in Iron, *Philos. Mag.* **15**, 977 (2007) 8

[43] I. I. Mazin, How to calculate the degree of spin polarization in ferromagnets?, *Phys. Rev. Lett.* **83**, 4 (1998) 8

[44] J. Smit, Magnetoresistance of ferromagnetic metals and alloys at low temperatures, *Physica* **17**, 612 (1951) 9

[45] P. C. Van Son, H. Van Kempen and P. Wyder, Boundary resistance of the ferromagnetic-nonferromagnetic metal interface, *Phys. Rev. Lett.* **58**, 2271 (1987) 10, 11

[46] T. Kimura, J. Hamrle, Y. Otani, K. Tsukagoshi and Y. Aoyagi, Suppression of spin accumulation in nonmagnet due to ferromagnetic ohmic contact, *Appl. Phys. Lett.* **85**, 3795 (2004) 14, 43

[47] H. Idzuchi, Y. Fukuma, S. Takahashi, S. Maekawa and Y. Otani, Effect of anisotropic spin absorption on the Hanle effect in lateral spin valves, *Phys. Rev. B* **89** (2014) 16, 43, 84, 85

[48] T. Maassen, I. J. Vera-Marun, M. H. D. Guimarães and B. J. Van Wees, Contact-induced spin relaxation in Hanle spin precession measurements, *Phys. Rev. B* **86**, 235408 (2012) 16

[49] M. Johnson and R. H. Silsbee, Coupling of Electronic Charge and Spin at a Ferromagnetic-Paramagnetic Metal Interface, *Phys. Rev. B* **37**, 5312 (1988) 16

[50] Y. Fukuma, L. Wang, H. Idzuchi, S. Takahashi, S. Maekawa et al., Giant enhancement of spin accumulation and long-distance spin precession in metallic lateral spin valves., *Nat. Mater.* **10**, 527 (2011)

[51] H. Idzuchi, Y. Fukuma and Y. Otani, Spin transport in non-magnetic nano-structures induced by non-local spin injection, *Phys. E Low-dimensional Syst. Nanostructures* **68**, 239 (2015) 16

[52] F. Bloch, Nuclear induction, *Phys. Rev.* **70**, 460 (1946) 16

[53] H. C. Torrey, Bloch Equations, *Phys. Rev.* **104**, 563 (1956) 16

[54] P. W. Anderson, Localized Magnetic States in Metals, *Phys. Rev.* **124**, 41 (1961) 18

[55] K. Inoue and Y. Nakamura, Kondo-Type Resistivity Anomaly in Noble Metal Alloys with 3d Metals, *Phys. Status Solidi* **58**, 355 (1973) 19, 67

[56] T. A. Costi, A. C. Hewson and V. Zlatic, Transport coefficients of the Anderson model via the numerical renormalization group, *J. Phys. Condens. Matter* **6**, 2519 (1994) 20, 21, 67

[57] J. Boyce and C. Slichter, Conduction-electron spin density around Fe impurities in Cu above and below the Kondo temperature, *Phys. Rev. B* **13**, 379 (1976) 22

[58] OOMMF User's Guide, Version 1.0, M. J. Donahue and D. G. Porter, Interagency Report NISTIR 6376, National Institute of Standards and Technology, Gaithersburg, MD (Sept 1999) 22

[59] R. Cimrman. SfePy - write your own FE application. In P. de Buyl and N. Varoquaux, editors, Proceedings of the 6th European Conference on Python in Science (EuroSciPy 2013), pages 65 - 70, 2014. http://arxiv.org/abs/1404.6391 23

[60] M. C. Rosamond, J. T. Batley, G. Burnell, B. J. Hickey and E. H. Linfield, High contrast 3D proximity correction for electron-beam lithography: An enabling technique for the fabrication of suspended masks for complete device fabrication within an UHV environment, *Microelectron. Eng.* **143**, 5 (2015) 30, 31

[61] J. Ekin, *Experimental Techniques for Low-Temperature Measurements*, Oxford University Press (2006) 37

[62] The Stoner package is a freely available python package, written and developed by members of the Condensed matter group at the University of leeds. The latest version can be obtained at http://www.github.com/gb119/Stoner-PythonCode/. 41

[63] H. Idzuchi, S. Karube, Y. Fukuma, T. Aoki and Y. Otani, Impact of interface properties on spin accumulation in dual-injection lateral spin valves, *Appl. Phys. Lett.* **103**, 162403 (2013) 43

[64] J. M. Pomeroy and H. Grube, "Negative Resistance" Errors in Four-Point Measurements of Tunnel Junctions and Other Crossed-Wire Devices, *J. Appl. Phys.* **105**, 2 (2009) 44, 45, 46, 58

[65] M. Stiles and D. Penn, Calculation of spin-dependent interface resistance, *Phys. Rev. B* **61**, 3200 (2000) 44

[66] Q. Yang, P. Holody, R. Loloee, L. L. Henry, J. P. W. Pratt et al., Prediction and measurement of perpendicular giant magnetoresistances of Co/Cu/Ni(84)Fe(16)/Cu multilayers, *Phys. Rev. B* **51**, 3226 (1995) 44

[67] T. Kimura, Y. Otani and P. M. Levy, Electrical control of the direction of spin accumulation, *Phys. Rev. Lett.* **99**, 1 (2007) 47, 78

[68] F. L. Bakker, A. Slachter, J. P. Adam and B. J. Van Wees, Interplay of peltier and seebeck effects in nanoscale nonlocal spin valves, *Phys. Rev. Lett.* **105**, 136601 (2010) 49, 51, 53, 57, 59

[69] M. Johnson and R. H. Silsbee, Calculation of nonlocal baseline resistance in a quasi-one-dimensional wire, *Phys. Rev. B* **76**, 153107 (2007) 49, 57

[70] S. Kasai, S. Hirayama, Y. K. Takahashi, S. Mitani, K. Hono et al., Thermal engineering of non-local resistance in lateral spin valves, *Appl. Phys. Lett.* **104**, 1 (2014) 49, 50

[71] P. A. Schroeder, R. Wolf and J. A. Woollam, Thermopowers and resistivities of silver-palladium and copper-nickel alloys, *Phys. Rev.* **138**, A105 (1965) 51, 53

[72] A. D. Avery and B. L. Zink, Peltier Cooling and Onsager Reciprocity in Ferromagnetic Thin Films, *Phys. Rev. Lett.* **111**, 126602 (2013) 51

[73] B. L. Zink, A. D. Avery, R. Sultan, D. Bassett and M. R. Pufall, Exploring thermoelectric effects and Wiedemann-Franz violation in magnetic nanostructures via micromachined thermal platforms, *Solid State Commun.* **150**, 514 (2010) 52

[74] G. S. Okram and N. Kaurav, Size-dependent resistivity and thermopower of nanocrystalline copper, *J. Appl. Phys.* **110**, 023713 (2011) 52

[75] A. Slachter, F. L. Bakker and B. J. Van Wees, Anomalous Nernst and anisotropic magnetoresistive heating in a lateral spin valve, *Phys. Rev. B* **84**, 20412 (2011) 52, 53

[76] S. Hu and T. Kimura, Anomalous Nernst-Ettingshausen effect in nonlocal spin valve measurement under high-bias current injection, *Phys. Rev. B* **87**, 14424 (2013) 53

[77] E. R. Rumbo, Thermopower measurements on copper and silver at low temperatures with particular attention to scattering by residual magnetic impurities, *Philos. Mag.* **22**, 0953 (1970) 53

[78] G. K. White, The Thermal and Electrical Conductivity of Copper at Low Temperatures, *Aust. J. Phys.* **6**, 397 (1953) 53

[79] E. Villamor, M. Isasa, L. E. Hueso and F. Casanova, Temperature dependence of spin polarization in ferromagnetic metals using lateral spin valves, *Phys. Rev. B* **88**, 184411 (2013) 58, 61, 72, 73

[80] R. J. Pedersen and F. L. Vernon, Effect of film resistance on low-impedance tunneling measurements, *Appl. Phys. Lett.* **10**, 29 (1967) 58

[81] Y. Ji, A. Hoffmann, J. E. Pearson and S. D. Bader, Enhanced spin injection polarization in Co / Cu / Co nonlocal lateral spin valves, *Appl. Phys. Lett.* **052509**, 52509 (2006) 58

[82] H. Zou, X. J. Wang and Y. Ji, Nonlocal spin valves with thin Co electrodes for spin-transfer, *J. Appl. Phys.* **108**, 1 (2010) 58

[83] J. T. Batley, M. C. Rosamond, E. H. Linfield, G. Burnell and B. J. Hickey, Spin relaxation through Kondo scattering in Cu/Py lateral spin valves. **220420**, 1 (2015) 61

[84] M. Erekhinsky, A. Sharoni, F. Casanova and I. K. Schuller, Surface enhanced spin-flip scattering in lateral spin valves, *Appl. Phys. Lett.* **96**, 10 (2010) 61

[85] M. Zhu, C. L. Dennis and R. D. McMichael, Temperature dependence of magnetization drift velocity and current polarization in Ni80 Fe20 by spin-wave Doppler measurements, *Phys. Rev. B* **81**, 140407 (2010) 61

[86] H. Idzuchi, Y. Fukuma, L. Wang and Y. Otani, Spin relaxation mechanism in silver nanowires covered with MgO protection layer, *Appl. Phys. Lett.* **101** (2012) 61, 62, 70, 85

[87] F. Beuneu and P. Monod, Conduction-electron spin resonance in cold-worked Al, Cu, and Ag: The spin-flip cross section of dislocations, *Phys. Rev. B* **13**, 3424 (1976) 62

[88] S. Karube, H. Idzuchi, K. Kondou, Y. Fukuma and Y. Otani, Spin relaxation characteristics in Ag nanowire covered with various oxides, *Appl. Phys. Lett.* **107**, 3 (2015) 62

[89] J. H. Mooij, Electrical conduction in concentrated disordered transition metal alloys, *Phys. status solidi* **17**, 521 (1973) 65

[90] N. Giordano, W. Gilson and D. E. Prober, Experimental study of Anderson localization in thin wires, *Phys. Rev. Lett.* **43**, 725 (1979) 66

[91] P. A. Lee and T. V. Ramakrishnan, Disordered electronic systems, *Rev. Mod. Phys.* **57**, 287 (1985) 66

[92] Y. Niimi, D. Wei, H. Idzuchi, T. Wakamura, T. Kato et al., Experimental verification of comparability between spin-orbit and spin-diffusion lengths, *Phys. Rev. Lett.* **110**, 16805 (2013) 66

[93] G. Bergmann, Weak Localization in Thin Films a time-offlight experiment with conduction electrons (1983) 66

[94] B. Knook, *De anomale electrische weerstand van een aantal Cu-, Ag- en Au-legeringen*, Ph.D. thesis, University of Leiden (1962) 66

[95] J. Mydosh, *Spin glasses : an experimental introduction*, Taylor & Francis (1993) 66

[96] D. B. Poker and C. E. Klabunde, Temperature dependence of electrical resistivity of vanadium, platinum, and copper, *Phys. Rev. B* **26**, 7012 (1982) 67

[97] R. A. Matula, Electrical resistivity of copper, gold, palladium and silver, *J. Phys. Chem.* **8**, 1147 (1979) 67

[98] S. Steenwyk, S. Hsu, R. Loloee, J. Bass and W. Pratt, Perpendicular-current exchange-biased spin-valve evidence for a short spin-diffusion lenght in permalloy, *J. Magn. Magn. Mater.* **170**, L1 (1997) 69, 84

[99] N. W. Ashcroft and N. D. Mermin, *Solid State Physics*, Saunders (1976) 70

[100] A. Fert, J. J.-L. Duvail and T. Valet, Spin relaxation effects in the perpendicular magnetoresistance of magnetic multilayers, *Phys. Rev. B* **52**, 6513 (1995) 70, 71

[101] F. J. Jedema, M. S. Nijboer, A. T. Filip and B. J. van Wees, Spin injection and spin accumulation in all-metal mesoscopic spin valves, *Phys. Rev. B* **67**, 16 (2002) 70

[102] P. Monod, Magnetic field dependence of the kondo resistivity minimum in CuFe and CuMn alloys, *Phys. Rev. Lett.* **19**, 1113 (1967) 71

[103] A. Fert, A. Friederich and A. Hamzic, Hall effect in dilute magnetic alloys, *J. Magn. Magn. Mater.* **24**, 231 (1981) 71

[104] B. Nadgorny, R. J. Soulen, Jr., M. S. Osofsky, I. I. Mazin et al., Transport spin polarization of Ni(x)Fe(1-x): electronic kinematics and band structure **61**, 3788 (1999) 74

[105] P. Yu, X. F. Jin, J. Kudrnovský, D. S. Wang and P. Bruno, Curie temperatures of fcc and bcc nickel and permalloy: Supercell and Green's function methods, *Phys. Rev. B* **77**, 1 (2008) 74

[106] H. A. Mook, J. W. Lynn and R. M. Nicklow, Temperature Dependence of the Magnetic Excitations in Nickel, *Phys. Rev. Lett.* **30**, 10 (1973) 74

[107] S. Nonoguchi, T. Nomura, Y. Ando and T. Kimura, Electrical manipulation of spin polarization and generation of giant spin current using multi terminal spin injectors, *J. Appl. Phys.* **111**, 11 (2012) 78

[108] S. O. Valenzuela and M. Tinkham, Direct electronic measurement of the spin Hall effect., *Nature* **442**, 176 (2006) 83

[109] M. Zwierzycki, Y. Tserkovnyak, P. J. Kelly, A. Brataas and G. E. W. Bauer, First-principles study of magnetization relaxation enhancement and spin transfer in thin magnetic films, *Phys. Rev. B* **71**, 1 (2005) 85